Dissertation
submitted to the
Combined Faculties for the Natural Sciences and for Mathematics
of the Ruperto-Carola University of Heidelberg, Germany
for the degree of
Doctor of Natural Sciences

Put forward by

Diplom-Informatiker: Denis Wohlfeld

Born in: Leipzig

Oral examination: 16.12.2009

Simulation, Analysis, and Fabrication of Miniaturized Components with Applications in Optical Interconnects and Parallel Microscopy

Referees: **Prof. Dr. Karl-Heinz Brenner**

Prof. Dr. Stefan Sinzinger

Kurzfassung: Optik und Miniaturisierung sind zwei Schlüsseltechnologien mit vielfältigen Anwendungsfeldern, denn sie ermöglichen Produkte mit höherer Funktionalität bei gleichzeitiger Reduktion der Größe sowie der Kosten.

In dieser Arbeit werden zwei Anwendungsmöglichkeiten für Mikrooptik in den Bereichen optischer Übertragungstechnik und paralleler Mikroskopie untersucht. Weiterhin werden verschiedene optische Simulationsmethoden aus den Bereichen Strahlenoptik und skalarer Wellenoptik in homogenen und inhomogenen Medien analysiert und weiterentwickelt.

Die Herstellung und Optimierung von miniaturisierten und hochkompakten Faserkopplern, die unter anderem für "Active Optical Cables" geeignet sind, bilden den ersten Schwerpunkt der Arbeit. Dabei wird besonders auf die Herstellung mittels UV Tiefenlithographie in SU-8 sowie mögliche Replikationstechniken eingegangen. Durch die Verwendung von mehreren Belichtungungen unter unterschiedlichen Einstrahlwinkeln wird die lithographische Herstellung von hochpräsizen Strukuren mit einer Höhe von mehreren hundert Mikrometern und schrägen Flächen ermöglicht, die zudem auf einfache Weise replizierbar sind.

Im letzten Teil werden die Vorteile der Mikrooptik im Bereich paralleler Mikroskopie untersucht, sowie das neue Konzept eines parallelen Mikroskops auf der Basis von GRIN-Stablinsen vorgestellt.

Abstract: Optics and miniaturization of components are both key technologies supporting the progress in many multidisciplinary areas and enabling products with more functionality at reduced size and costs.

Two applications of microoptic integrations in the field of optical communications and parallel microscopy are investigated. This thesis also deals with light propagation in geometrical optics and scalar wave optics, both in homogeneous and inhomogeneous media.

The fabrication and optimization of integrated fiber couplers with applications in active optical cables are the first focus of the thesis. A new concept for compact fiber coupling with a pitch distance of 250 μm and an integrated 45° mirror is introduced and all steps from fabrication over replication to coupling efficiency measurements are described.

For the fabrication of miniaturized components a new method using UV deep lithography in SU-8 with multidirectional exposure for structure angles above 45° is developed. Replication technologies like direct UV replication and soft lithography using PDMS are also analyzed with respect to large-scale production of highly integrated structures.

Miniaturization is also investigated in parallel microscopy to speed up high content screens in life science. The concept of parallel microscopy is analyzed and a compact GRIN-rod lens system is developed with the capability of scanning microwell arrays with 10k spots in one scan.

Contents

Introduction

Chapter 1

Introduction and overview

In the last decades a change in the communication market took place. Established electrical communication systems were replaced by optical systems. Using higher frequencies, electrical interconnects are restricted by different physical limitations, while optical interconnects are not. Unlike optical transmission, the primary challenge for electrical conductors is the attenuation of wires with increasing length and frequency. In addition photons show no cross talk and are not influenced by electrical and magnetic fields, at least not with normal field strength. These advantages are used in long distance communication where the processing is done by electronic circuits and the transmission by optical fibers. Optics for transmission is used for ever shorter distances. From connecting continents, countries, cities, and homes, one is now looking into the advantages of optics in the range of less than a hundred meters and even to chip-to-chip as well as chip internal interconnects.

This work started with the demands of the FAIR project where a new acceleration facility at the GSI Darmstadt is planned to be built until 2015. One detector in this experiment is the CBM detector (compressed barionic matter), which is designed to analyze highly compressed nuclear matter. Due to the design of the detector and the surroundings, special demands on the interconnections have to be met. They have to work on different voltage levels in the range of $\pm 300\,\mathrm{V}$ and be radiation hard. They have to be pluggable, no pig tails, and have to cover a first distance of $30\,\mathrm{m}$. The best solution would be a cable which is pluggable like ordinary electrical cables but transmits the information on the basis of light. This concept is called 'Active Optical Cables' and is not only interesting for high energy physics but although for the whole communication and computer market. Recently a study showed a potential market of several billion dollars. Intel, Emcore, Finisar and some other companies already have products on the market. Unfortunately these are still expensive and do not use the full potential concerning the density of optical interconnects. The optimal pitch distance for optical channels is determined by the pitch of the fabricated sources and photodiodes, in the case of VCSELs the pitch is $250\,\mu\mathrm{m}$ allowing a density of four channels per millimeter. As the conversion from electric signals to optical ones has to be done in a very small connector there is no place for large bend radii which would be needed if the fibers were directly coupled to the VCSELs. For fibers parallel to the board on which the VCSELs are mounted one needs some kind of deflecting element next to the fiber alignment structure. The resulting micro optical element has to fulfill at least three tasks: the deflection of light by 90°, the alignment of the fiber, and a funnel to simplify the insertion of fibers. Additionally, an optimized surface of the mirror will focus the light into the fiber to reach higher coupling efficiencies. An application of these coupling structures will only be successful if two or more criteria are met. First, the replication of these structures has to be accurate, fast, and at low costs. Secondly, a process to align the fiber couplers with the VCSELs has to be found.

A total different field of miniaturized components is microscopy. While classic microscope objectives consists of many bulky glass lenses, alternatives using miniaturized lenses are being investigated. The design goal here is a largely parallel and compact system where the components do not have to be time-consumingly aligned and where the lenses are fabricable by replication techniques suitable for mass production. Such a miniaturized system is not only better suited for parallelization, its production is also cheaper.

Overview

The first part of the thesis investigates different fabrication and replication techniques, especially UV deep lithography for the fabrication of integrated micro optical structures. Starting with an investigation of the UV illumination system for lithography using mask projection, the chapter goes on with UV deep lithography and points out some alternatives to it. UV deep lithography is examined in detail with a focus on multidirectional exposure. The subsequent chapter introduces two replication techniques: direct UV replication and soft lithography.

Part 2 deals with different light propagation methods, from ray tracing to the propagation of waves in inhomogeneous media. The chapter on geometrical optics introduces a customized ray tracer which is developed to simulate and optimize the coupling efficiencies of fiber couplers including the propagation of rays in inhomogeneous media. In order to describe light propagation from mask patterns into thick resist, the next chapter deals with aspects of scalar wave optics and analyzes different methods for the propagation of waves in homogeneous and inhomogeneous media. Part 2 is concluded with a UV deep lithography simulation which is based on the methods derived in the chapter on scalar wave optics.

Two applications for miniaturized components are described in Part 3. The main application of the thesis is the development and characterization of an integrated fiber coupler fabricated by UV deep lithography. A compact optical coupling technique is one of the main features of active optical cables.

Miniaturized parallel microscopy designed for the ViroQuant project is the topic of the second application part. The concept is based on GRIN-rod lenses and integrated beam splitters. The chapter also compares analytical paraxial equations for GRIN rod lenses to simulations including higher order terms.

The thesis is concluded with a summary and perspectives.

Part I

Fabrication of miniaturized components

Chapter 2

Fabrication

In the 20th century lithography became one of the most important fabrication techniques for miniaturized components. One distinguishes between many different types of lithography such as transfer lithography, soft lithography, micro lithography, and photolithography.

Among these different lithographies the photolithography stands out because it enables most of the important micro fabrication techniques. It starts with the complete market of integrated circuits, where the size of the smallest circuit path is given by the resolution of the lithography, and continues as the most important technology for the fabrication of microoptics (Sinzinger and Jahns [47]).

Two types of photolithographic fabrication procedures are distinguished: scanning lithography and mask lithography. In scanning lithography a modulated laser writes directly into a light-sensitive material called photoresist. In mask lithography the pattern of an amplitude mask is transfered into the photoresist, either by projection optics or by uniform illumination of the mask positioned directly on the photoresist. In the latter, one distinguishes between hard contact, where mask and photoresist are in direct contact, and soft contact, where a small gap is left in between. During exposure the photoresist changes its properties. In the following development step and in the case of negative photoresist, exposed areas remain and unexposed areas are dissolved.

Deep lithography means using thick resist layers, typically $> 10\,\mu$m. The achievable resolution strongly depends on the exposure source used. In deep lithography the resist is exposed with particles like protons or with electro-magnetic sources of different wavelengths. UV deep lithography stands for photolithography using thick resist and a UV light source of about 365 nm. This has to be distinguished from Deep UV lithography where a radiation between 150 nm and 300 nm is used. In this work, scanning lithography is used to produce binary amplitude masks, which are later used in contact lithography to transfer their pattern into a thick resist.

The chapter starts with an analysis and optimization of a given UV illumination system used for photolithography. The photoresist SU-8 allows to produce structures with heights of up to several $100\,\mu$m. Applying illumination under different angles of incident increases the variety of functions which can be integrated into micro optical components. Ultra precision machining as an emerging alternative for the fabrication of micro optical components is also investigated. At the end of the chapter a comparison in terms of surface quality and accuracy is given.

2.1 UV illumination systems

The quality of structures achieved by contact lithography depends strongly on the properties of the illumination system. Important parameters are the spectrum of the light source, the illumination homogeneity on the substrate, and the angular spread. In the field of UV illumination systems, mercury vapor lamps are commonly used. The spectral lines at near UV are the i-line at 365 nm, the h-line at 405 nm, and the g-line 434 nm. Due to the spatial dimension of the bulb and the radiating volume within, no passive optical system can be built to achieve a homogeneous illumination with high power efficiency and an angular spread close to 0°. For this reason, every illumination system is a trade-off between power, homogeneity and angular spread. In the following chapter the characteristics and particularly the angular spectrum of a given UV illumination system are analyzed and improvements for a reduced angular spectrum are described.

2.1.1 Properties of light sources for deep lithography

The main properties of a UV illumination system for deep lithography are the intensity distribution, the angular spread, and the radiation spectrum. The spectrum of the light source has to be suitable for the photoresist used. SU-8 for example is sensitive in the near UV region which corresponds to the i-line of a mercury vapor source. The intensity at the illumination area defines the time needed to expose the resist. Lower intensity means longer exposure times. A homogeneous irradiance across the whole illumination area is also needed. Critical is the angular spread of the system because an increasing spread has a direct impact on the side walls of the obtained structures.

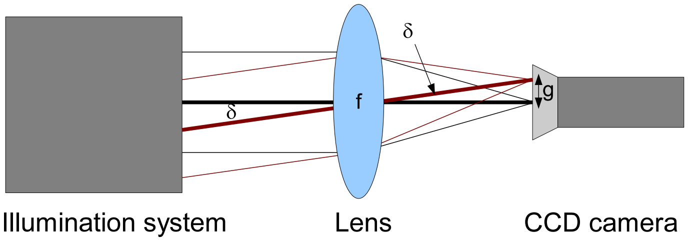

Figure 2.1: Angular measurement of the UV illumination system

The angular spectrum of a light source can be measured using an optical Fourier transform system, see Liu´s doctoral thesis [34, chapter 5]. Her measurement setup consisted of a lens and a camera placed in the focus of the lens to determine the angular spectrum of the light source (see fig. 2.1). The relation between the divergence angle δ and the lateral shift g in the image is given by the formula

$$\pm\delta = atan\left(\frac{g}{f}\right). \tag{2.1}$$

In the geometric optics approximation of a thin and symmetric lens, a ray going through the center of the lens is not refracted, hence the angle δ is found on both sides of the lens. This is also depicted in figure 2.1 where the rays through the center of the lens are bolder than the two border rays. For completeness, the relation between the pixel in the image and the lateral shift g is given by

$$g = n \cdot d_{pix} \tag{2.2}$$

where n is the number of pixels and d_{pix} the size of one pixel on the CCD camera.

The measured angular spectrum of the mask aligner was ±3.3 °. Figure 2.2 shows the horizontal deviation Δx of a theoretical SU-8 structure with height h, which was exposed by an illumination system with an angular divergence of δ.

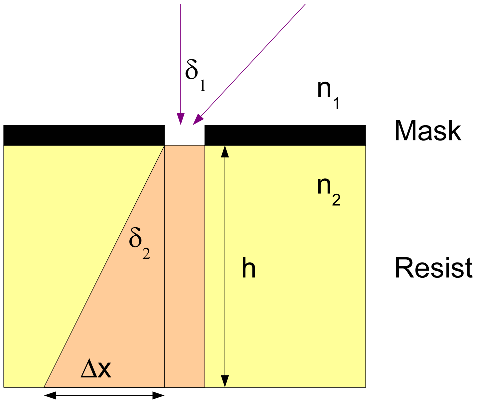

Figure 2.2: Impact of angular spread on SU-8 structures

Taking Snell's law into account the horizontal error Δx is

$$\Delta x = h \cdot tan\left(asin\left(\frac{n_1}{n_2} sin\left(\delta_1\right)\right)\right). \tag{2.3}$$

For a structure with $h = 100\,\mu$m and an angular spread of $\alpha_1 = 3.3\,°$ the lateral error is $\Delta x = 3.4\,\mu$m.

In the following paragraphs different methods to reach a homogeneous light distribution with low angular deviation will be examined.

2.1.2 Uniform illumination

In photolithography, a uniform light distribution in the illumination plane is very important to reach constant quality of structures along the whole substrate. An optical setup for a mask aligner with uniform illumination often consists of an elliptical mirror for collimation, a light source mounted in the first focal point of the collimator, a fly's eye for uniform radiation, and a condenser lens (see fig. 2.3). Since the source is a luminous volume, the light focused by the collimator into the second focal point is expanded. The light distribution in the focal area is further distorted by elements inside the light paths from the bulb to the focal point such as wires for electrical contacts and holding structures which cast shadows.

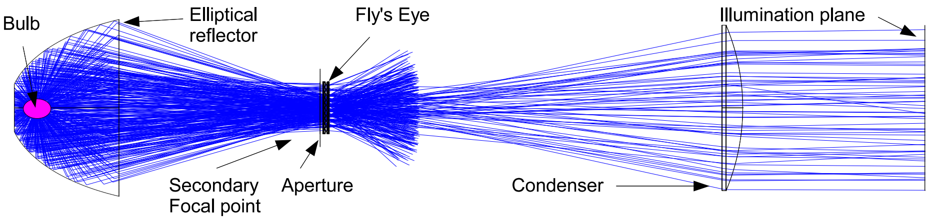

Figure 2.3: Typical UV illumination setup in photolithography

The fly's eye, positioned in the second focal point of the collimator, consists of two lens arrays. The first fly's eye array is often called objective array and the second array is called field array. Each objective lens of the array forms an image of the collimated light source at the focal plane of the objective lens. A uniform illumination is achievable with one lens array and one condenser lens positioned in the focal plane of the objective array, if the angular divergence of the incoming light is close to zero. In this scenario the radiation of each image is transformed to fill most of the illumination plane. The result is an accumulation of all images of the light source which forms a uniform illumination. Since the angular divergence of the light source is not zero, the images overlap only partly, building a nonuniform distribution. If the field array is added to this setup and put into the focus of the objective array, and if the condenser lens is moved behind the field array, a uniform intensity distribution on the illumination plane is achieved. The figures 2.4 and 2.5 show the result of a Zemax simulation of the mask aligner without and with a fly's eye.

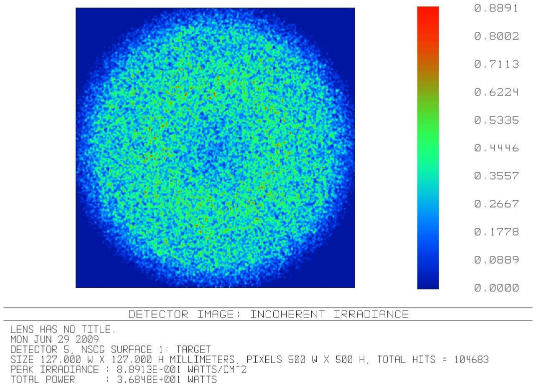

```
DETECTOR IMAGE: INCOHERENT IRRADIANCE
LENS HAS NO TITLE.
MON JUN 29 2009
DETECTOR 5, NSCG SURFACE 1: TARGET
SIZE 127.000 W X 127.000 H MILLIMETERS, PIXELS 500 W X 500 H, TOTAL HITS = 104683
PEAK IRRADIANCE : 8.8913E-001 WATTS/CM^2
TOTAL POWER     : 3.6848E+001 WATTS
```

Figure 2.4: Without a fly's eye: donut-shaped irradiance on the plane of illumination

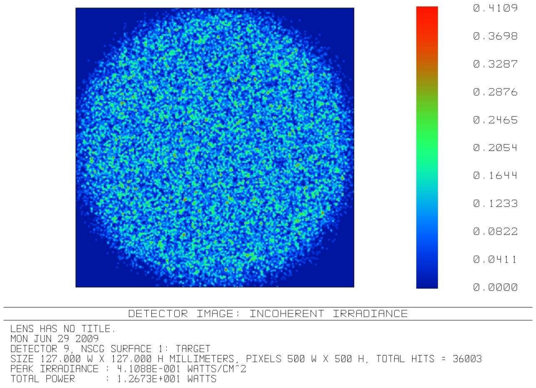

```
DETECTOR IMAGE: INCOHERENT IRRADIANCE
LENS HAS NO TITLE.
MON JUN 29 2009
DETECTOR 9, NSCG SURFACE 1: TARGET
SIZE 127.000 W X 127.000 H MILLIMETERS, PIXELS 500 W X 500 H, TOTAL HITS = 36003
PEAK IRRADIANCE : 4.1088E-001 WATTS/CM^2
TOTAL POWER     : 1.2673E+001 WATTS
```

Figure 2.5: With a fly's eye: uniform irradiation on the plane of illumination

The profile without a fly's eye is that of a donut, since the lens is a Fourier transformer of the angular distribution inside the aperture, which is donut-shaped. With a fly's eye, the desired top hat is obtained. It is obvious that the homogeneity of the top hat in the illumination plane depends on the number of images which are accumulated. The more channels of the arrays are added in vertical and horizontal direction, the better the homogeneity becomes. There is also a draw back if too many channels are used. Since the edges between two lenses are not infinitely sharp, light is scattered in these regions. As a rule of thumb, approximately seven channels or more are needed for uniform irradiance at the illumination plane. The fly's eye of the mask aligner used in this thesis consisted of ten channels in both directions with a total size of 4 cm × 4 cm.

2.1.3 Trade-off between intensity, uniformity and angular spectrum

The condenser lens with focal distance f_{cond} is located one focal length f_{cond} behind the field array. Therefore, the lens transforms a spatial deviation $d(r)$ at the field array into an angle deviation δ on the plane of illumination as follows:

$$\delta = atan\left(\frac{d(r)}{f_{cond}}\right). \tag{2.4}$$

The parameter $d(r)$ corresponds to an aperture radius, which covers the field of view of the condenser lens. For homogeneity, a large number of channels is needed, which results in a larger aperture causing an increase of the angular divergence. In order to minimize δ, the aperture has to be reduced while keeping the homogeneity in a tolerable region. If a miniaturized fly's eye with equal performance were available, this would be the first choice because the angular deviation is reduced while keeping the homogeneity. The miniaturization of the fly's eye is limited by the diameter of the second focal spot of the light source d_{2nd}. If the diameter of the aperture becomes smaller than d_{2nd}, the intensity in the illumination plane decreases rapidly. The simplest way to reduce δ of a mask aligner is to insert an aperture behind the field array at the costs of power and homogeneity. In order to find the best parameters for the insertion of an aperture, the available mask aligner system was simulated in Zemax. Figure 2.6 shows the system setup for the simulation.

In order to minimize the energy loss from the aperture, the best location is a few millimeters behind the field lens in the focal plane (see fig.2.7).

The simulated irradiance behind the field lens shows (fig. 2.8) that the energy in the different images from the primary light source decreases from the center to the outer regions of the field array. Thus an aperture which cuts of the outer parts reduces the angular divergence without losing too much power. Table 2.2 shows a comparison between different radii of apertures. The aperture in the first line reduces the 10 × 10 array to the inner four images of the primary source, while the aperture in the second line includes the inner sixteen images, and the last is without an aperture. All three setups have been simulated, realized and measured. The detector in the simulation with a length of 12.7 cm

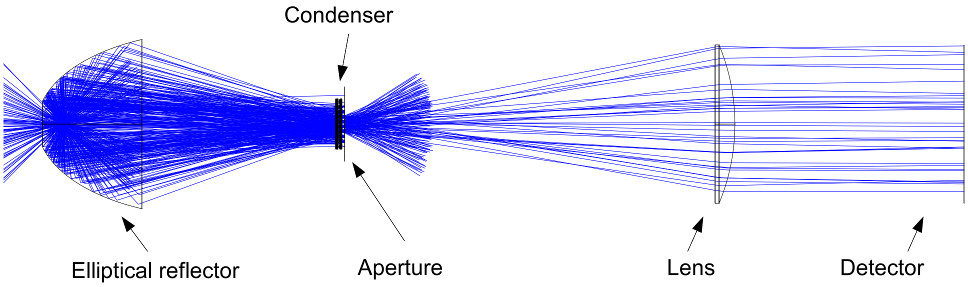

Figure 2.6: Zemax Simulation of the mask aligner with aperture

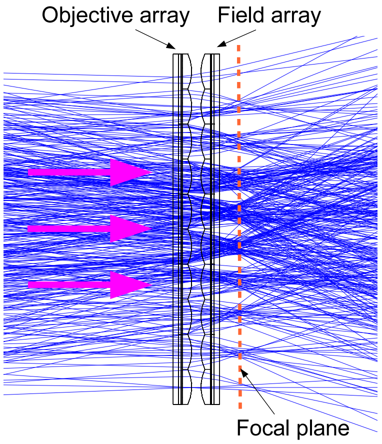

Figure 2.7: Side view on the fly's eye

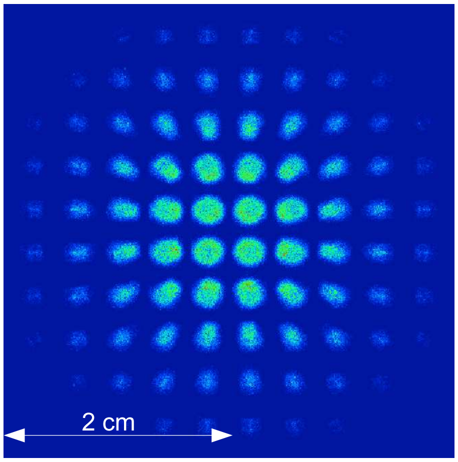

Figure 2.8: Irradiance 1.5 mm behind the field array (Zemax)

was divided into 15×15 squares. In order to reduce the influence of statistics in the Monte Carlo simulation, the number of emitted rays was chosen so that more than 1.4 million hit the detector. The values for the uniformity on the detector, i.e. the plane of illumination, are calculated within an aperture of $r = 5\,\mathrm{cm}$. Valley intensity Iv and peak intensity Ip are given relative to the mean value. The standard deviation is calculated from the normalized intensities I within the illumination plane

$$\sigma_{sim} = \sqrt{\frac{1}{N}\sum_{N}\left(1 - \frac{I}{\bar{I}}\right)^2}. \tag{2.5}$$

The standard deviation σ_{sim} in formula 2.5 is only calculated for the simulation because the number of measured data points was insufficient.

Table 2.2 shows the correlation between radius of aperture, intensity, and uniformity: decreasing the aperture size decreases the angular spectrum however also the intensity and uniformity. The measured intensities for both apertures were lower than the simulated

Aperture	Intensity $\left[\frac{mW}{cm^2}\right]$		Angle		Relative uniformity [%]				
Radius	I_{sim}	I_{mes}	δ_{sim}	δ_{mes}	Iv_{sim}	Iv_{mes}	Ip_{sim}	Ip_{mes}	σ_{sim}
4.0 mm	9.7	6.4	0.7°	0.7°	94.2	72.1	115.1	120.2	4.3
8.5 mm	32.4	22.4	1.6°	x	95.0	90.0	110.3	109.6	3.2
none	72.0	72.0	3.0°	3.3°	96.4	96.1	106.5	102.6	2.1

Table 2.2: Comparison of system parameters for different radii of aperture, simulated and measured : intensity, angular spread, relative peak and valley intensity, and the coefficient of variation for the simulation

ones. This indicates that the illumination distribution on the field array is spread more widely over the field than in the simulation. Another reason can be that the aperture was not positioned perfectly in the focal plane of the field array. Both errors lead to lower intensity. The variation in the peak to valley intensities is an indicator for an alignment error of the aperture with the optical axis, because peak and valley intensity were in the plane of illumination opposite to each other, peak on the right, valley on the left. Another influencing factor is the distortion of the second focal point of the light source. If it is not radially symmetric around the optical axis, but shifted for example, the uniformity on the illumination plane is also distorted. Figure 2.9 shows the intensity distribution and figure 2.10 the angular divergence. In both figures an aperture with $r = 8.5\,\text{mm}$ is used.

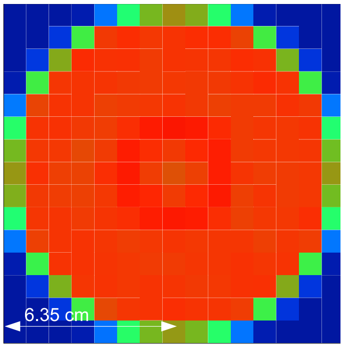

Figure 2.9: Simulated intensity on the detector with aperture $r = 8.5\,\text{mm}$

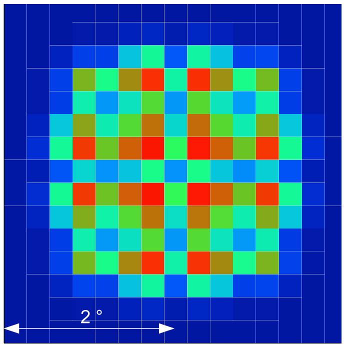

Figure 2.10: Simulated angular spectrum on the detector with aperture $r = 8.5\,\text{mm}$

In summary, the angular deviation of the mask aligner can be reduced by inserting an aperture in the focal plane behind the field array. It depends on the application whether intensity and uniformity or angular divergence are more important. A better choice, however, is a miniaturized fly's eye with more channels.

2.1.4 Light rod as homogenizer

Light distributions are also homogenized with light rods. The principle of a light rod, which is often rectangular to avoid caustics [24], is based on superposition of the incident light field with every total internal reflection. The number of reflections m for a single ray propagating under the angle α inside a light pipe with length L and diameter d is calculated in 1D with the equation

$$m = \frac{2L \cdot tan\,(\alpha)}{d}. \tag{2.6}$$

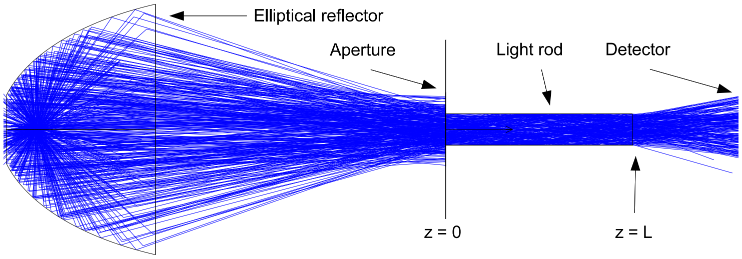

Figure 2.11: Zemax Simulation of the mask aligner with a light rod

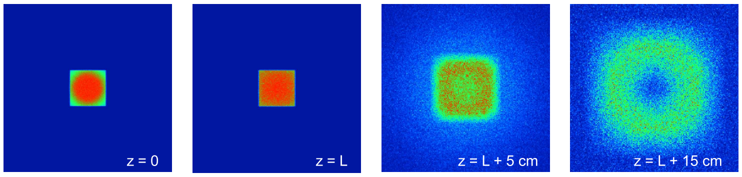

Figure 2.12: Intensity distribution in front of the light rod at $z = 0$, at the end of the light rod $z = 100\,\text{mm}$, at $z = 150\,\text{mm}$ and at $z = 250\,\text{mm}$

The level of uniformity at the end of the light rod is a function of the number of internal reflections. The uniform light distribution is only given at the end of the light rod, since the angular characteristics are not changed. This is illustrated by the following simulation. The fly's eye of the mask aligner is swapped with an aperture and a light rod with $d = 17\,\text{mm}$. The length $L = 100\,\text{mm}$ corresponds to three reflections for an angle of incident $\alpha = 10°$. Figure 2.11 shows the simulation setup.

The simulated intensity distribution at different z locations are shown in figure 2.12. In order to achieve uniformity in a certain distance behind the light rod, an imaging system is indispensable. The size of the illumination area is then given by the magnification factor and the diameter of the light rod. To investigate the performance of such a system the following one was simulated (fig. 2.11): Light rod with $L = 20\,\text{cm}$ and $r = 8.5\,\text{mm}$, two apertures, two lenses for imaging with magnification $m = 3$.

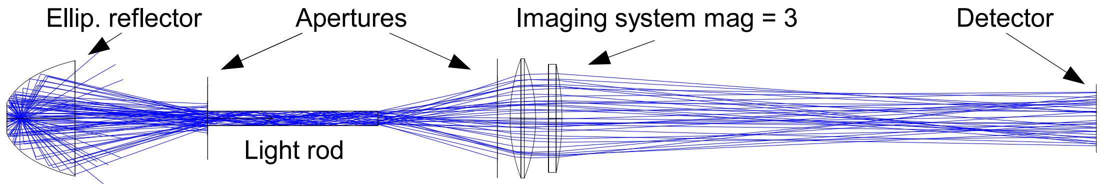

Figure 2.13: System with light rod and imaging optics

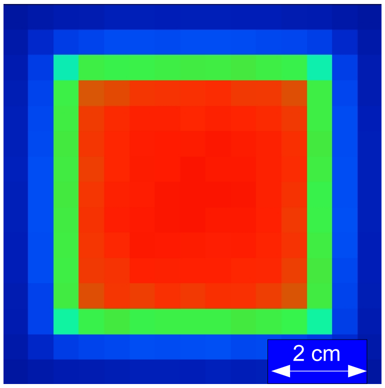

Figure 2.14: Intensity on the illumination plane

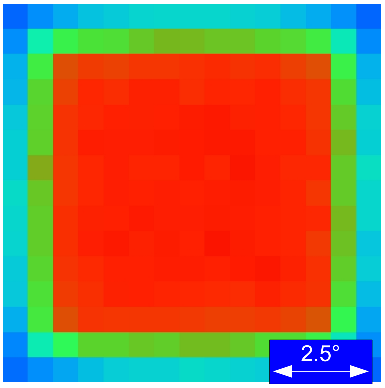

Figure 2.15: Angular spectrum on the illumination plane

The characteristics are summed up in table 2.3, and the intensity distribution on the illumination plane as well as the angular spectrum are shown in figure 2.14 and 2.15.

The system design study with a light rod shows that it is in principle possible to obtain uniformity with light rods. Considering UV illumination systems, the results propose the usage of a fly's eye instead of a light rod. The performance of the fly's eye in every analyzed property was equal or better.

Image width	Intensity $\left[\frac{mW}{cm^2}\right]$	Angle	Relative uniformity [%]		
			I_v	I_p	σ
5 cm	50.3	6.8°	88.9	107	4.7

Table 2.3: Performance of a simple light rod and imaging system

2.2 UV deep lithography

Deep lithography stands for lithography using resist thicknesses $> 10\,\mu$m which are exposed by particles or photons. With the invention of high functionally resists, which are sensitive to the near UV range, lithography in thick resist is not limited to the high requirements of particle beams or synchrotron radiation anymore. UV illumination systems described in the previous section are sufficient now.

The first section introduces the photolithography process with SU-8, which was used in this work to fabricate master structures for different applications. The following sections investigate the exposure process step and describe the development from normal exposure over inclined exposure to multidirectional exposure. The chapter is closed with an analysis of the surface quality, additional fabrication methods like ultra precision machining, and a conclusion.

2.2.1 SU-8 process

The negative tone photoresist SU-8, based on EPON SU-8 epox resin from Shell Chemical, was originally developed by IBM (LaBianca and Delorme [31] and Shaw [46]) and further decribed by Lorenz et al. [36]. With thicknesses up to 2 mm, high aspect ratios, mechanical stability, and sensitivity to UV light, it is used in many applications like micro fluidic, MOEMS, etc. (Despont et al. [14], Zhang et al. [59], Liu et al. [33]).

The SU-8 process ([26], [38]) is divided into eight steps shown in figure 2.16.

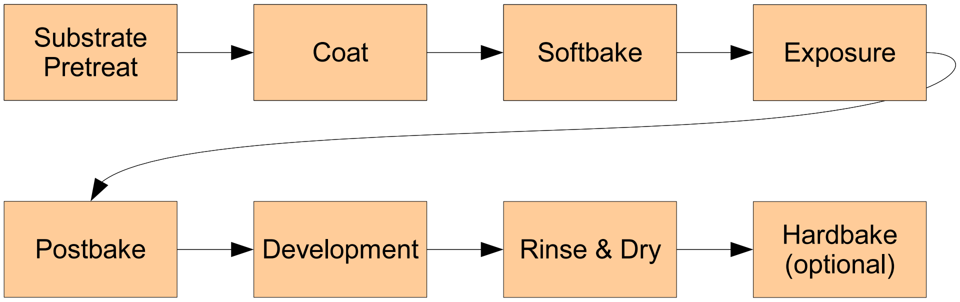

Figure 2.16: The SU-8 process chain

The ‘Exposure’, where the acid for the polymerization is generated in the illuminated regions, is the critical step and the focus of this section. The exposed regions of negative tone resist remain after development. That is, if the energy is high enough to allow cross links near the substrate for adhesion. Depending on the sequence, mask, resist, and substrate, one distinguishes between two setups for illumination. In the commonly used setup the mask lies on top of the resist, but it is also possible to turn the substrate upside down and set the mask on the substrate with the resist below. In this case, gray tone lithography in SU-8 is possible at the cost of structure resolution. The loss in resolution is a result of the diffractions at the mask and the longer distance between mask and resist. This effect is also visible if the mask is in contact with the resist and the resist surface is not perfectly planar. Therefore it is important in the coating process to minimize the height variation of the resist. So called 'edge beads' have to be removed. The term 'edge bead' refers to the effect in spin coating that the resist layer near the border of the substrate is thicker due to surface tension. Since the edge beads only occur in the outer region of the substrate, a reduction of the mask size in hard contact lithography reduces the impact of edge beads. This approach was used in this work. With a substrate size of 6 cm × 6 cm all masks were cut down to at least 3 cm × 3 cm, the planar region of the resist. The impact of edge beads on the resolution of structures is shown in figures 2.17 and 2.18.

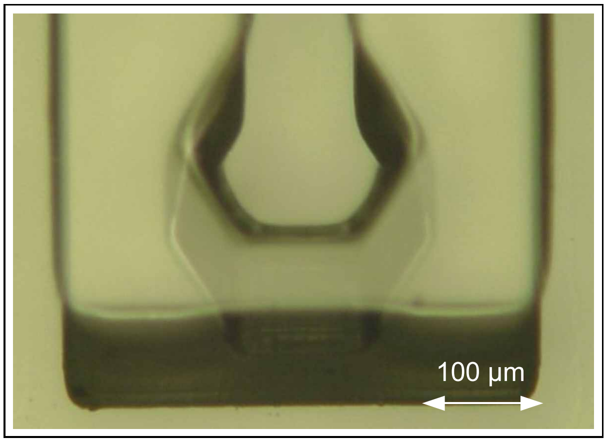

Figure 2.17: SU-8 structure exposed through 6 cm mask

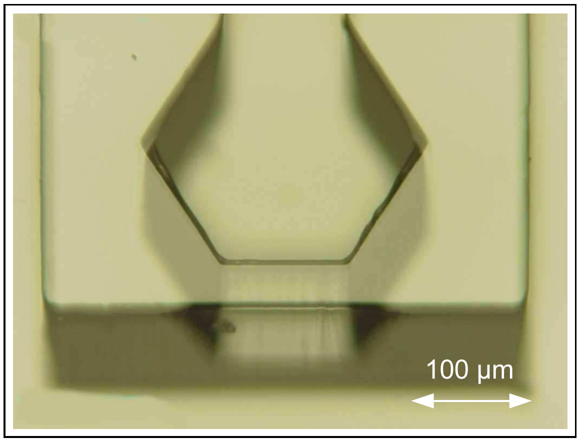

Figure 2.18: SU-8 structure exposed through 2 cm mask

2.2.2 Spin coating

In all lithography experiments 3 gr SU-8 were deposited on square float-glass substrates with a length of 6 cm after those had been cleaned. The following spinning process started with a rotation speed at 500 rpm to spread the SU-8 for $t_1 = 15\,\text{sec}$ and defined the film thickness in a following step with faster rotations for $t_2 = 25\,\text{sec}$. Figures 2.19 and 2.20 show the correlation between final structure height and spinning speed in the coating process. For an approximation of interim values, the function

$$h(x) = A \cdot e^{-\alpha \cdot x} + c \tag{2.7}$$

with the parameters A, α, c was fitted. Knowing the exact film thickness is very important in order to be able to apply the correct exposure time.

2.2.3 Exposure dose

The precise control of the exposure dose $D = I_0 \cdot t$ is of the utmost importance in the whole process. Insufficient exposure time results in total loss of the structures due to

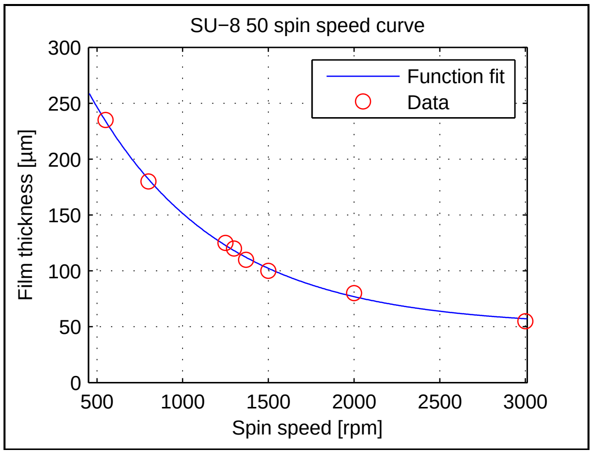

Figure 2.19: SU-8 50 spin speed curve ($t_2 = 25\,\text{sec}$), fit parameters: $A = 381.5\,\mu\text{m}$, $\alpha = 0.001325\,\text{rpm}^{-1}$, $c = 50\,\mu\text{m}$

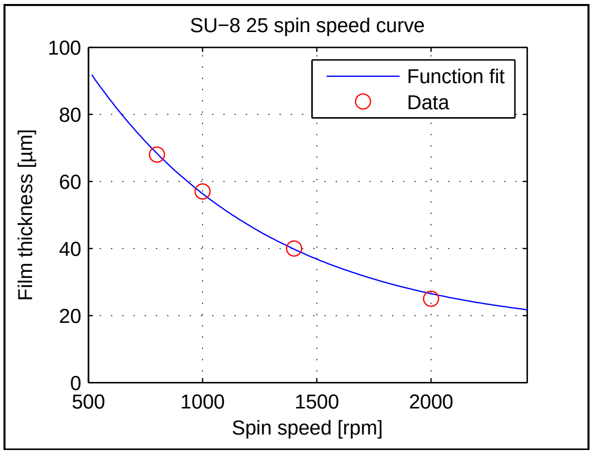

Figure 2.20: SU-8 25 spin speed curve ($t_2 = 25\,\text{sec}$), fit parameters: $A = 148.3\,\mu\text{m}$, $\alpha = 0.00128\,\text{rpm}^{-1}$, $c = 15\,\mu\text{m}$

the insufficient cross linking with the substrate, while longer exposure times reduce the resolution. The correct exposure time depends strongly on the thickness of the resist. Fabrication of structures with new thicknesses typically requires a series of time consuming experiments to determine the correct exposure time. The results of experiments with gray lithography in the next section suggest a minimum exposure dose for different film thicknesses, while the section following gray lithography examines the exposure dose needed for sufficient adhesion in standard lithography.

2.2.3.1 Gray tone lithography

In 2002 experiments with gray tone lithography in SU-8 were made by the group of Brenner to fabricate continuous phase elements (Wohlfeld and Kufner [55]). The exposure setup and two fabricated phase elements are shown in figures 2.21 to 2.23.

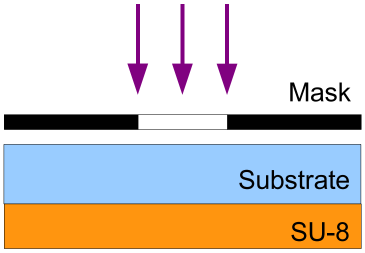

Figure 2.21: Exposure setup for gray tone lithography in SU-8

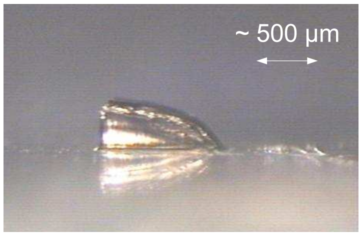

Figure 2.22: Wedge by linear gray tone mask

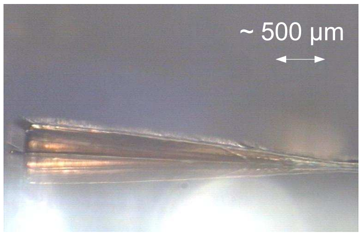

Figure 2.23: Wedge by exponential gray tone mask

In order to determine the threshold between remaining and dissolving SU-8 in relation to the exposure dose, two experiments were undertaken. In a first step a mask with an array of rectangular apertures was exposed to increasing doses and the SU-8 height was measured after development (see table 2.4).

Height h [μm]	0	96	164	233	342	425
Exposure time t[sec]	10	20	40	70	130	250

Table 2.4: Dependence of structure height on exposure time

These results suggest an exponential relation between the structure height h and the exposure dose D

$$D(h) = I_0 \cdot c \cdot e^{\alpha \cdot h}. \tag{2.8}$$

A function fit with $c = 11.1256\,\mathrm{sec}$, $I_0 = 7.97\,\frac{\mathrm{mW}}{\mathrm{cm}^2}$, and $\alpha = 0.0073\,\frac{1}{\mu\mathrm{m}}$ is shown in figure 2.24 where I_0 is the intensity in the plane between substrate and SU-8.

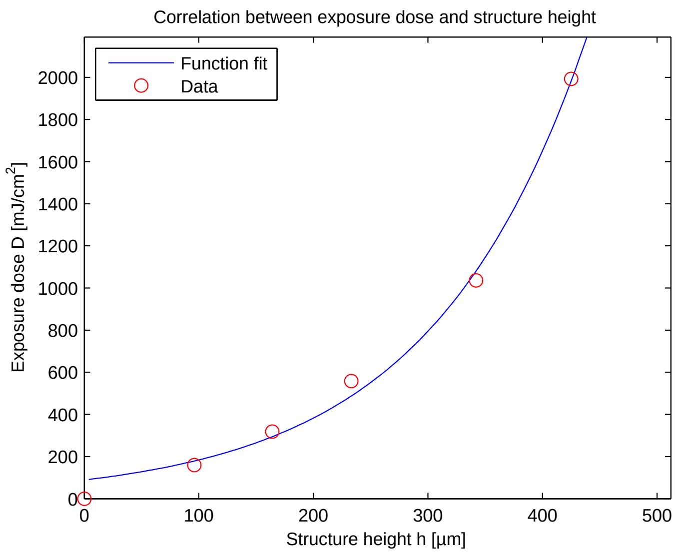

Figure 2.24: Correlation between SU-8 cross link depth and exposure dose in gray tone lithography

The height of the structures corresponds to the threshold between remaining and dissolving SU-8 during the development. This threshold is the lower limit for the exposure time. It does not correspond to the minimum exposure dose in standard lithography (mask on SU-8) because the cross linking has not only to be strong enough to resist the development but also to provide enough adhesion to the substrate.

2.2.3.2 Standard lithography

In standard lithography the results of an exposure dose experiment are of four kinds: no structure (lift off), under cut structure (low exposure), normal structure (correct exposure), and blurred structure (over exposure). These four are illustrated in figure 2.25.

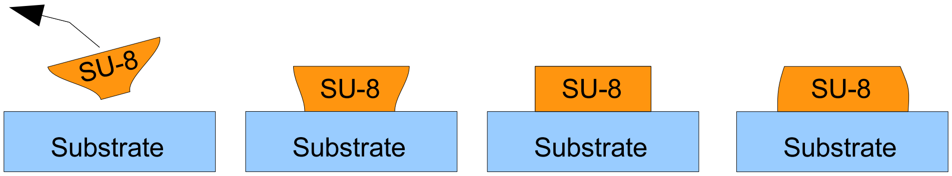

Figure 2.25: Structure variation with increasing exposure dose: lift off, under cut, normal, blurred

The difference between a remaining structure and one that lifts off is narrow and does not only depend on the exposure dose. Other factors are impure substrate surface, too high temperature steps in the postbake process, i.e. thermal stress, size of the adhesion area, etc.. Applying adhesion promoter like HMDS (Hexamethyldisilazane) before coating SU-8 increases the adhesion of SU-8 on glass or silicon wafers and therefore reduces the minimum required exposure dose. The exposure dose also depends on the reflectivity of the substrate, which has to be taken into account if the substrate used is not glass.

The SU-8 experiments on glass substrates at our chair of the last 5 years are depicted for different thicknesses and structure sizes in figure 2.26. The results for mask apertures smaller than $50\,\mu$m are from the diploma student Ehrle.

The figure distinguishes between good results (green symbols), insufficient exposure (blue symbols), and over exposure (red symbols). The experiments from the student in the upper left corner were made to characterize the new mask aligner 3 years ago. His mask included many small structures the size of $25\,\mu$m, while the structure size of the other experiments were in the range of $75 - 150\,\mu$m. Since adhesion for smaller structures becomes increasingly critical, he used higher exposure doses than the other results suggest. In summary, the exposure dose not only depends on the film thickness but also on the size of the smallest structures to guarantee sufficient adhesion on the substrate. The compilation in figure 2.26 is still useful to get an idea, in which exposure dose region one should start with new film thickness and or structure size.

Since most lab notes only included the exposure time and the date, the actual exposure dose had to be estimated from the known intensity measurements. For completeness, the compilation of the intensity variations over the past 5 years is depicted in figure 2.27

The intensity compilation shows that the intensity dropped by 40% over a time scale of 2 years and 5 months, or 110 h of mask aligner operation.

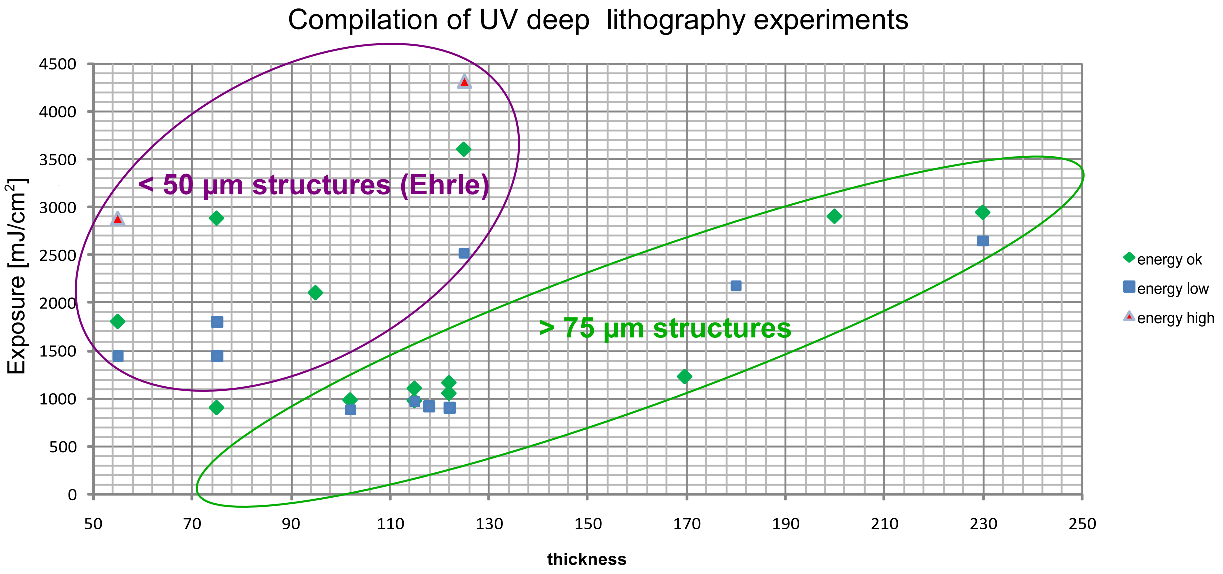

Figure 2.26: Exposure experiments in the last 5 years

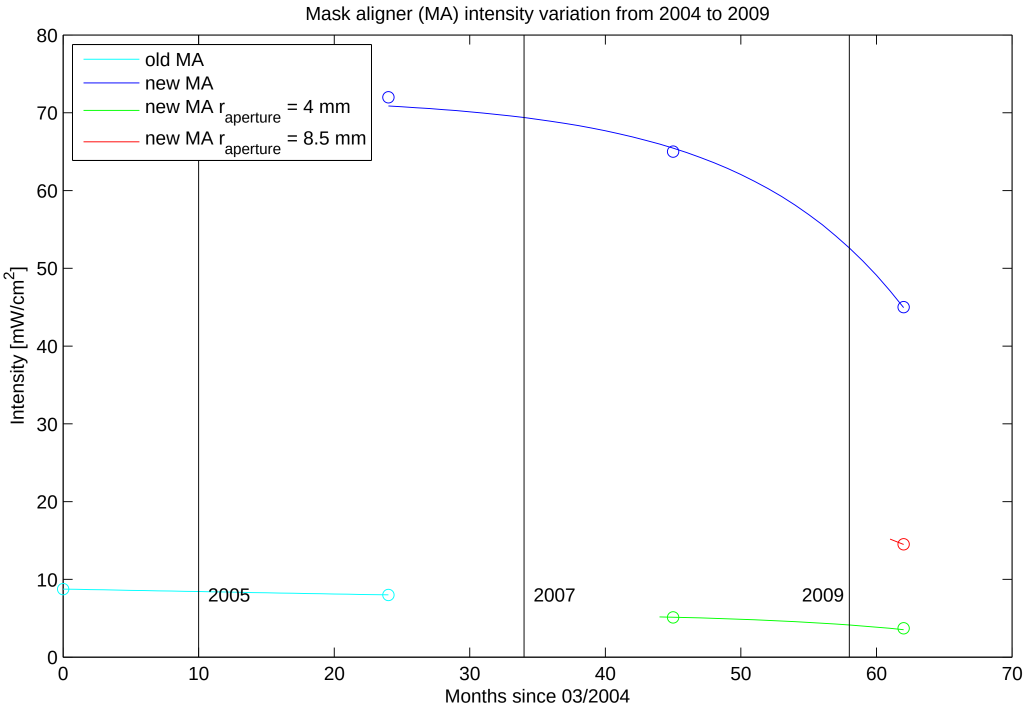

Figure 2.27: Development of mask aligner intensity in the last 5 years, measured values are represented by circles

2.2.4 Inclined exposure

Lithography is not restricted to perpendicular exposure. The angle of incidence is another degree of freedom in the fabrication of micro structures. Standard methods for inclined exposure, demonstrated by others (Yoon et al. [57], Han et al. [27], and Ling and Lian [32]), are limited to structure angles < 36° due to the refraction law. Using additional components like coupling prisms and immersion liquids, every angle from 0° to > 55° can be realized.

2.2.4.1 Slanted structures and angle of incidence

The relation between the angle of incidence θ_i and the angle of the light inside the resist θ_t, determining the angle of the structure, is given by Snells's law

$$n_i sin\left(\theta_i\right) = n_t sin\left(\theta_t\right). \tag{2.9}$$

Without any additional components, θ_t is limited by

$$\theta_{t_{max}} = asin\left(\frac{n_i}{n_t}\right). \tag{2.10}$$

From air with $n_i = 1$ to SU-8 $n_t = 1.69$ the limit is $\theta_{tmax} < 36.3°$. Additional components like prisms are needed to increase θ_{tmax}. For example, in a setup with a 90° quartz prism, θ_{tmax} is increased above 55°. Figure 2.28 depicts a setup for slanted exposure with water immersion and figure 2.29 depicts the corresponding angles inside the resist.

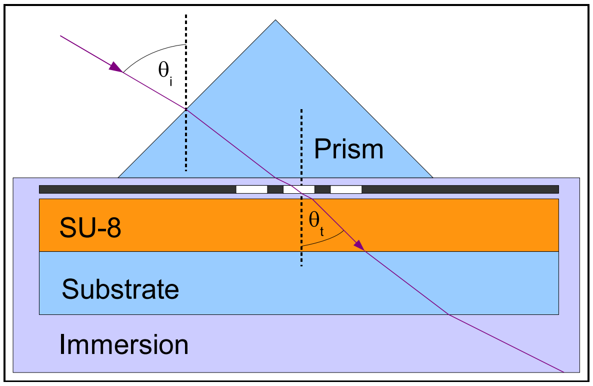

Figure 2.28: Photolithography setup for inclined exposure with water immersionand 90° prism

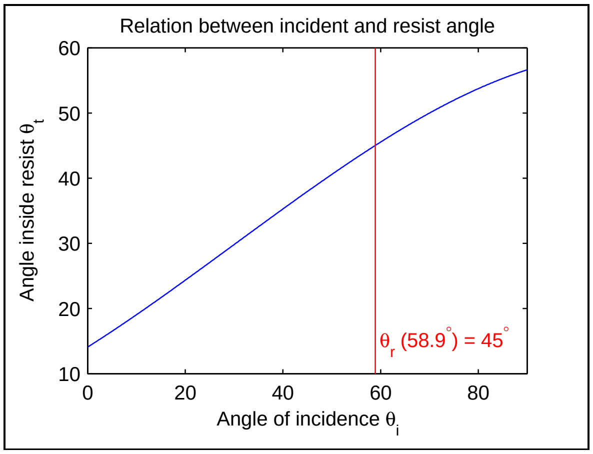

Figure 2.29: Relation between θ_i coming from air ($n_i = 1$) and θ_t inside the resist ($n_t = 1.69$) for the setup with 90° prism. 45° structure are obtained with $\theta_i = 58.9°$

Structures with 45° angles are of special interest in this thesis. The slanted surfaces can be used as mirrors, for example in integrated fiber couplers in the application part of this work. Slanted structures for different rectangular apertures are shown in figure 2.30.

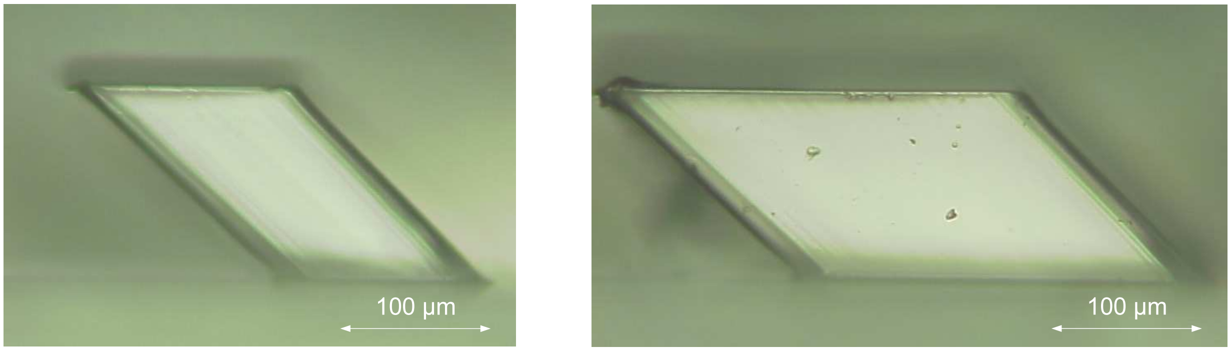

Figure 2.30: Slanted 45° structures in SU-8 for different rectangular aperture sizes

2.2.4.2 Transmissivity and reflectivity

Going from perpendicular to slanted exposure, reflections and energy transfer between surface boundaries have to be more careful evaluated.

Reflections on boundary surfaces deform structures and can cause additional ghost structures. A ghost structure is some remaining resist in a shadow area of the mask, often the form of an aperture near by. To prevent these, index matching in every possible layer is indispensable. Water with a refraction index of 1.33 proved to be practical.

The following derivation of transmission and reflection follows the explanations of Born and Wolf [1] and Brenner [4].

The transmission and reflection for the amplitude of polarized light on surface boundaries are described by the Fresnel formuale. By using the law of refraction one obtains

$$r_{\perp} = -\frac{sin\,(\alpha_i - \alpha_t)}{sin\,(\alpha_i + \alpha_t)} \tag{2.11}$$

$$t_{\perp} = \frac{2sin\,(\alpha_t)\,cos\,(\alpha_i)}{sin\,(\alpha_i + \alpha_t)} \tag{2.12}$$

$$r_{||} = \frac{tan\,(\alpha_i - \alpha_t)}{tan\,(\alpha_i + \alpha_t)} \tag{2.13}$$

$$t_{||} = \frac{2sin\,(\alpha_t)\,cos\,(\alpha_i)}{sin\,(\alpha_i + \alpha_t)\,cos\,(\alpha_i - \alpha_t)}. \tag{2.14}$$

The Fresnel coefficients r and t describe the relation between the amplitude of the incident electro magnetic field, and the reflected or transmitted field.

To meet the energy conservation, the incident energy on a unit square dA has to be equal to the reflected and transmitted energy per unit dA, thus

$$I_i \cdot cos\theta_i \cdot dA \cdot dt = I_r \cdot cos\theta_r \cdot dA \cdot dt + I_t \cdot cos\theta_t \cdot dA \cdot dt. \tag{2.15}$$

With the definition of the optical intensity I for $\mu = 1$ with the electrical field amplitude E

$$I = \frac{n}{2\mu_0 c} E^2 \tag{2.16}$$

and the law of reflection $\theta_i = \theta_r$, the energy conservation on surface boundaries becomes

$$n_i \cdot E_i^2 \cdot cos\theta_i = n_i \cdot E_r^2 \cdot cos\theta_i + n_t \cdot E_t^2 \cdot cos\theta_t. \tag{2.17}$$

or

$$E_i^2 = E_r^2 + \frac{n_t cos\theta_t}{n_i cos\theta_i} E_t^2. \tag{2.18}$$

By normalizing $E_i^2 = 1$ and inserting the definition of the Fresnel coefficients $r = \frac{E_r}{E_i}$ and $t = \frac{E_t}{E_i}$ one obtains

$$1 = |r|^2 + \frac{n_t cos\theta_t}{n_i cos\theta_i} |t|^2 . \tag{2.19}$$

with r and t either for $||$ or $\perp$ polarization.

For unpolarized light one has to average over all orientations for each polarization. Be E_u the part of one orientation of the polarized amplitude E_p with

$$E_u(\theta) = E_p cos\theta, \tag{2.20}$$

the average over all θ of E_u^2 is $\frac{1}{2}E_p^2$ since $\overline{cos^2} = 0.5$. The calculation for the perpendicular polarization E_{pp} of E_p is similar, exchanging $\cos\theta$ with $\sin\theta$, and also results $\frac{1}{2}E_{pp}^2$. Finally, the transmissivity T and reflectivity R for unpolarized light are

$$R = \frac{1}{2}\left(|r_\perp|^2 + |r_{||}|^2\right) \tag{2.21}$$

$$T = \frac{1}{2}\left(|t_\perp|^2 + |t_{||}|^2\right) \frac{n_t cos\theta_t}{n_i cos\theta_i}. \tag{2.22}$$

The diagram in 2.31 depicts the transmissivity and reflectivity for polarized and unpolarized light going from air to silica.

The second diagram in 2.33 shows the transmissivity for the slanted exposure setup for each boundary, with 90° prism (see 2.28) and water immersion: air to prism T_{prism}, prism to immersion T_{im1}, immersion to mask T_{mask}, mask to immersion T_{im2}, immersion to resist (SU-8) T_{resist}, and finally the transmissivity as product of all factors from air to resist T. For the energy transfer, there is no difference going from refraction index n_1 to refraction index n_2 or from n_1 to n_2. Therefore $T_{im1} = T_{mask} = T_{im2}$ share the same curve. The second figure shows the limit of water immersion. The transmitted energy drops fast beyond $\theta_i = 60°$. Structures with angles $\theta_r > 45°$ demand immersions with higher refraction indexes in order to keep reflections small. The improvement going from water immersion $n_w = 1.33$ to an immersion liquid with $n_i = 1.5$ is shown in the third diagram 2.34.

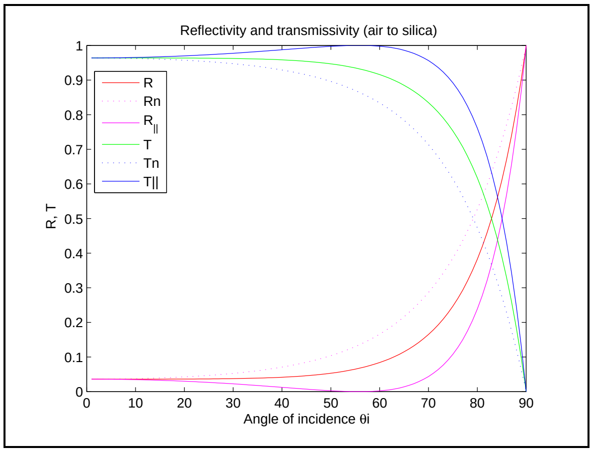

Figure 2.31: Reflectivity R and transmissivity T for normal, parallel, and unpolarized light going from air to silica

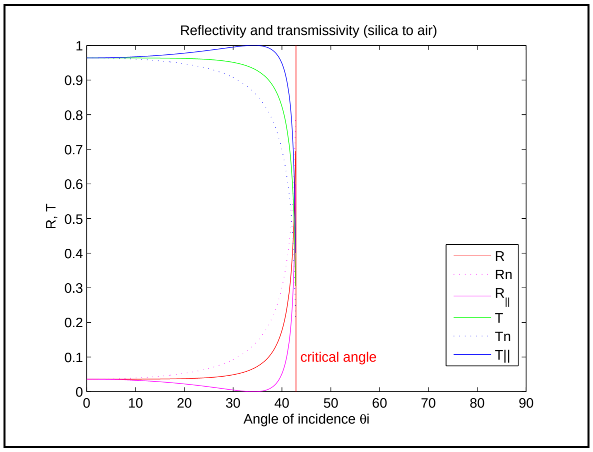

Figure 2.32: Reflectivity R and transmissivity T for normal, parallel, and unpolarized light going from silica to air

2.2.4.3 Exposure dose

During exposure, the important unit is the exposure dose D

$$D = I \cdot t \tag{2.23}$$

with the intensity I defining the exposure time t.

From the two equation forms of energy conservation

$$1 = |r|^2 + \frac{n_t cos\theta_t}{n_i cos\theta_i} |t|^2 \tag{2.24}$$

and

$$1 = \frac{I_r \cdot cos\theta_i}{I_i \cdot cos\theta_i} + \frac{I_t \cdot cos\theta_t}{I_i \cdot cos\theta_i} \tag{2.25}$$

with the incident intensity I_i, the reflected and transmitted intensities I_r and I_t, and the Fresnel coefficients r and t, a formula for the reflected and transmitted intensity is derived. Since the ratio I_r to I_i must be equal to the energy ratio E_r^2 to E_i^2 which is $|r|^2$, one derives the relation

$$I_r = I_i \cdot |r|^2 \,. \tag{2.26}$$

By setting formula 2.24 equal to formula 2.25, both formulas equaling 1, and inserting formula 2.26 one derives the relation between incident and transmitted intensity as:

$$\begin{aligned} \frac{n_t cos\theta_t}{n_i cos\theta_i} |t|^2 &= \frac{I_t \cdot cos\theta_t}{I_i \cdot cos\theta_i} \\ I_t &= I_i \cdot \frac{n_t}{n_i} \cdot |t|^2 \,. \end{aligned} \tag{2.27}$$

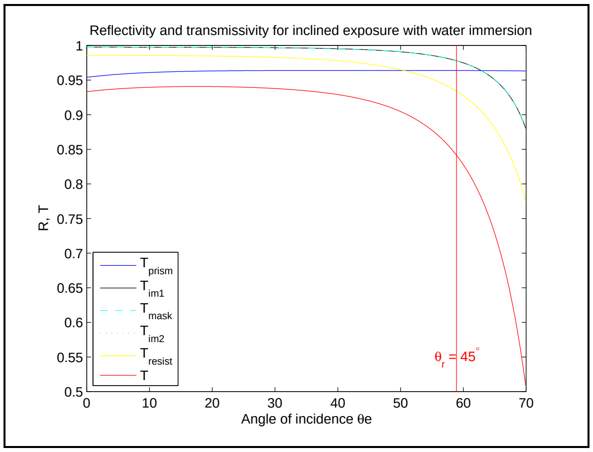

Figure 2.33: Transmissitivy T at every boundary for the inclined exposure setup from figure 2.28 with water immersion

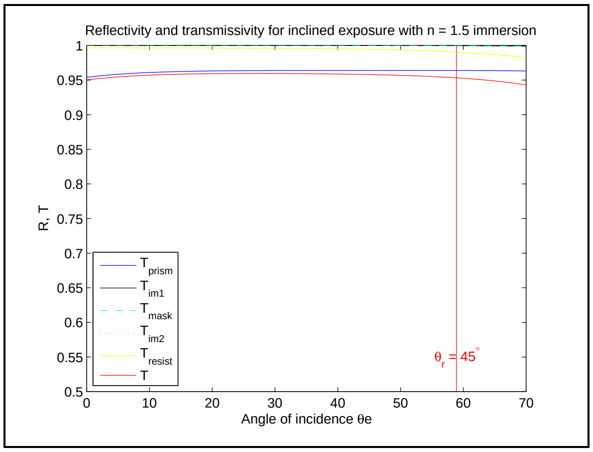

Figure 2.34: Transmissitivy T at every boundary for the inclined exposure setup from figure 2.28 with n = 1.5 immersion

Analog to the previous considerations for unpolarized reflectivity and transmissivity, the intensities for unpolarized light are

$$I_r = I_i \cdot \frac{1}{2}\left(|r_\perp|^2 + |r_{||}|^2\right) \tag{2.28}$$

$$I_t = I_i \cdot \frac{n_t}{n_i} \cdot \frac{1}{2}\left(|t_\perp|^2 + |t_{||}|^2\right). \tag{2.29}$$

The transmitted intensities on all surfaces for the 90° prism setup with water immersion are depicted in figure 2.35. In this setup the intensity inside the resist drops for 45° structures to 68%.

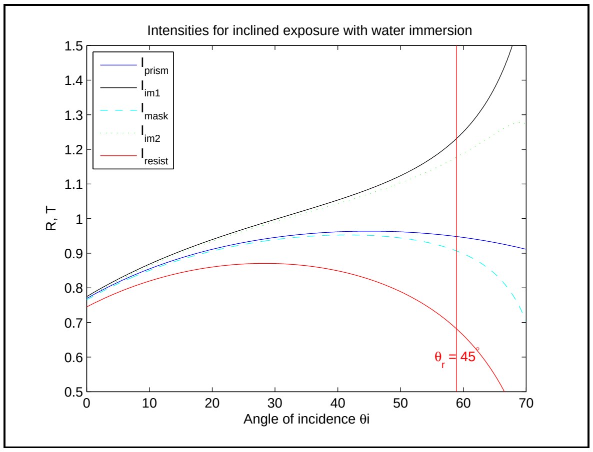

Figure 2.35: Transmitted intensites for inclined exposure (setup fig. 2.28)

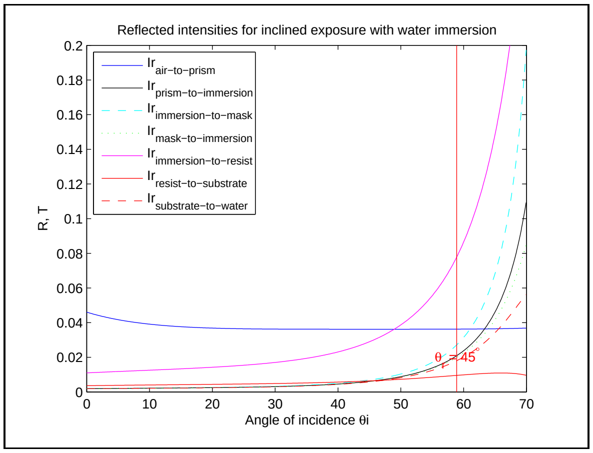

Figure 2.36: Reflected intensites for inclined exposure (setup fig. 2.28)

The reflections from each boundary are represented in diagram 2.36. Two reflections are critical, the reflection from the bottom side of the substrate back into the substrate (and to a great amount back into the resist) and the reflection from the boundary resist to substrate. The calculation above showed that the reflected intensity from the substrate back to the resist is less than 1%, and the reflected intensity from the water back into the substrate is 2% of the incident intensity, thus both are in a tolerable region.

2.2.5 Exposure setup

In inclined exposure, people often use setups where the substrate is inclined and the illumination source is left unchanged ([58], [27]). This is the setup of choice if index matching is dispensable. If index matching is indispensable, all air boundaries have to be filled with the immersion liquid, including the last interface substrate to air. Thus the substrate has to be put into a tank containing liquid, illustrated in figure 2.37. A more practicable solution is an inclined illumination while leaving the substrate in a horizontal position. In this setup only a few droplets of immersion liquid are needed between mask, prism, and resist and only a small volume under the substrate to fulfill the index matching requirements. The new setup is depicted in figure 2.38. Due to the easier handling and the minor consumption of immersion liquid - which does not matter for water but matters for other immersion liquids - the inclined illumination setup was used in this thesis for all inclined exposures.

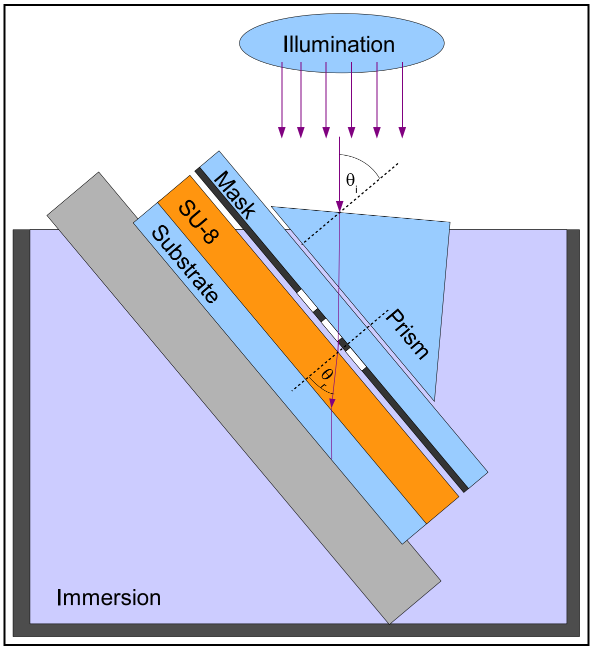

Figure 2.37: Multidirectional exposure setup with inclined substrate and immersion tank

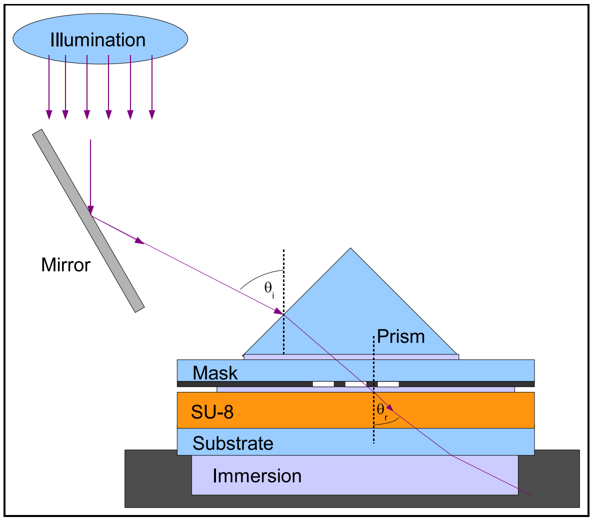

Figure 2.38: New multidirectional exposure setup with inclined illumination and minimum immersion liquid consumption

2.2.6 Multidirectional exposure

The functionality of structures, fabricated by photolithography, is further increased by illuminating under different angles of incidence. Figure 2.39 depicts a combination of slanted and perpendicular illumination.

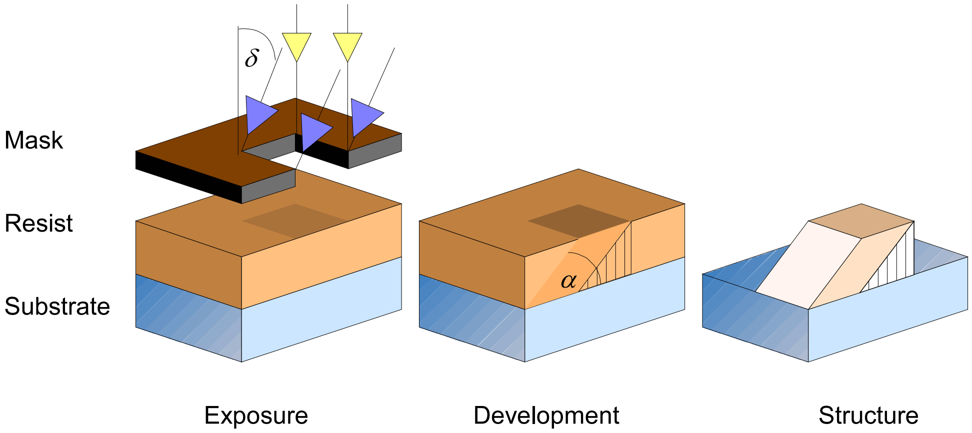

Figure 2.39: UV deep lithography with double exposure

Parallel to the work presented here, multidirectional exposure was investigated by Yoon et al. [58] who presented in their paper many different slanted SU-8 structures fabricated by variable inclined and normal exposure. Since they used no additional components like prisms presented in the paragraph before, their structure angle is limited.

The combination of inclined and normal exposure is beneficial for slanted micro structures used as masters for replication. Since cavities cause problems in molding replication approaches, the cavities generated by inclined exposure have to be filled. This is done with a preliminary exposure step with normal illumination. Naturally, the correct alignment of the mask in multi exposure has to be guaranteed. In the case of only one mask, the displacement of the mask in the different exposure steps has to be prevented, for example, with UV adhesive. Figure 2.40 and 2.41 show an integrated fiber coupling structure for two channels, fabricated by double exposure (normal, slanted).

In multi exposure lithography with one mask, some areas under the mask are exposed more than once. These areas show signs of overexposure since each single exposure step has to be long enough to provide enough energy for the polymerization down to the substrate. The effect of overexposure can be partly compensated by reducing each exposure time to slightly less than the minimum dose, the dose where a single exposure would result in insufficient adhesion. If the area, which is illuminated more than once, is large enough, the cumulated energy will provide enough polymerization for sufficient adhesion.

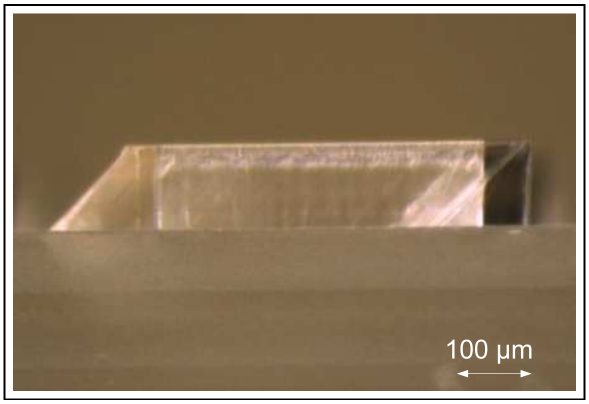

Figure 2.40: Micro structure fabricated by double exposure in SU-8 (side view)

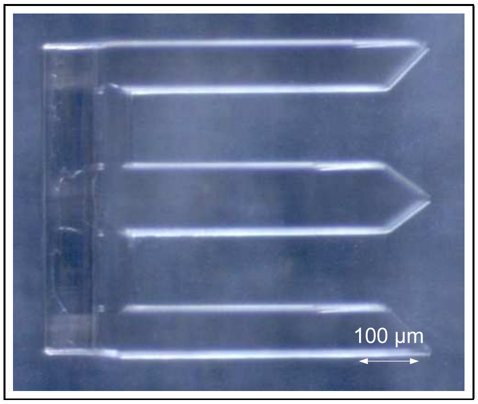

Figure 2.41: Micro structure fabricated by double exposure in SU-8 (top view)

2.2.7 Quality of structures

The quality of structures is defined by many properties depending on the requirements. For most miniaturized components the contour and position accuracy are important. The roughness of a surface is another relevant property for structures, if these surfaces have to provide functionality like deflecting and guiding light.

2.2.7.1 Position and contour accuracy

In lithography, the position accuracy is classified into the accuracy of alignment between mask and resist and the position accuracy of the fabricated structures. Mask alignment is critical in applications like chip fabrication with many layers, where each new layer has to be perfectly aligned with the last one, or in the fabrication of micro optical electrical mechanical systems (MOEMS) where the structure has to be placed in a specific position. The position accuracy of fabricated structures without mask change is defined by the accuracy of the mask production. The amplitude masks in this work were fabricated on a lithography scanner with a position accuracy of 50 nm and a minimum feature size of 800 nm.

The contour accuracy depends mainly on the resist and the illumination properties. A perfect rectangular aperture, imaged into resist, only generates vertical side walls with the correct exposure time (see fig. 2.25). Due to diffraction on the boundaries of the mask, the contour accuracy decreases with the thickness of the resist. In slanted exposure, the accuracy of the structure angle is important, especially if the surface is used as a mirror with the structure angle defining the reflection angle. Figure 2.42 demonstrates that an angular accuracy in the order of 1° over 80% of the surface is achievable.

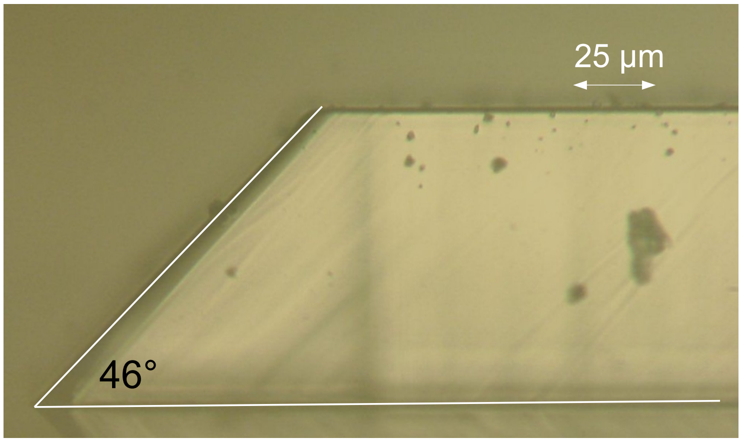

Figure 2.42: Micro structure with 46° angle obtained by UV deep lithography with double exposure

2.2.7.2 Surface quality

The side wall surfaces of SU-8 structures often show some kind of riffles. The experienced diversity of these riffles is large, but their general direction is always similar to the applied exposure direction. From stochastic riffles, figure 2.43, over periodic riffles, figure 2.44, to structures with smooth regions interrupted by small regions with riffles, everything has been observed.

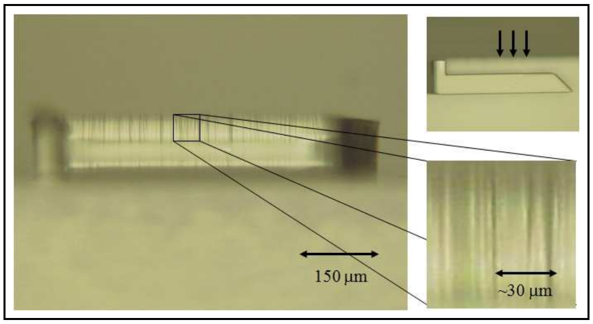

Figure 2.43: SU-8 sidewalls fabricated by normal exposure

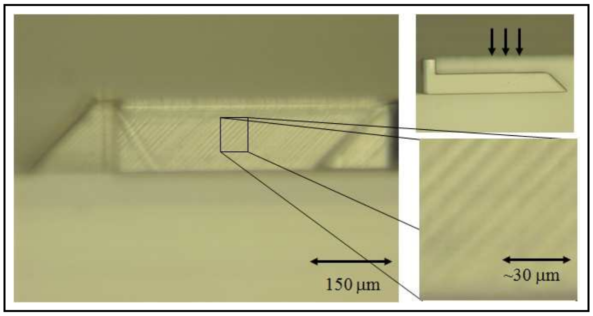

Figure 2.44: SU-8 sidewalls fabricated by double exposure (normal, inclined)

For the characterization of the surface gradients and roughness, a reflection measurement and a roughness measurement using a white light interferometer are employed.

Reflection measurement The local gradients of a surface determine the characteristics of a reflected beam. Therefore, a reflection measurement using a known source and evaluating the reflected intensity is one way to characterize the gradients of a reflective surface. One important application of slanted SU-8 structures use the slanted surface as energy reflector. Important here is, how much the surface disturbs the reflection of a Gaussian beam. Variables to characterize are, energy spread in x- and y-direction and the encircled energy within an aperture. All three parameters are normalized according to the σ of the Gaussian beam.

The measurement setup consists of a HeNe laser followed by a pinhole with radius $r_a = 50\,\mu$m. In the first step the intensity distribution behind the pinhole is measured. In the second step the beam is reflected on an optical flat and the intensity is measured again. In the third step the optical flat is exchanged with the slanted SU-8 surface. The three steps are depicted in figure 2.45.

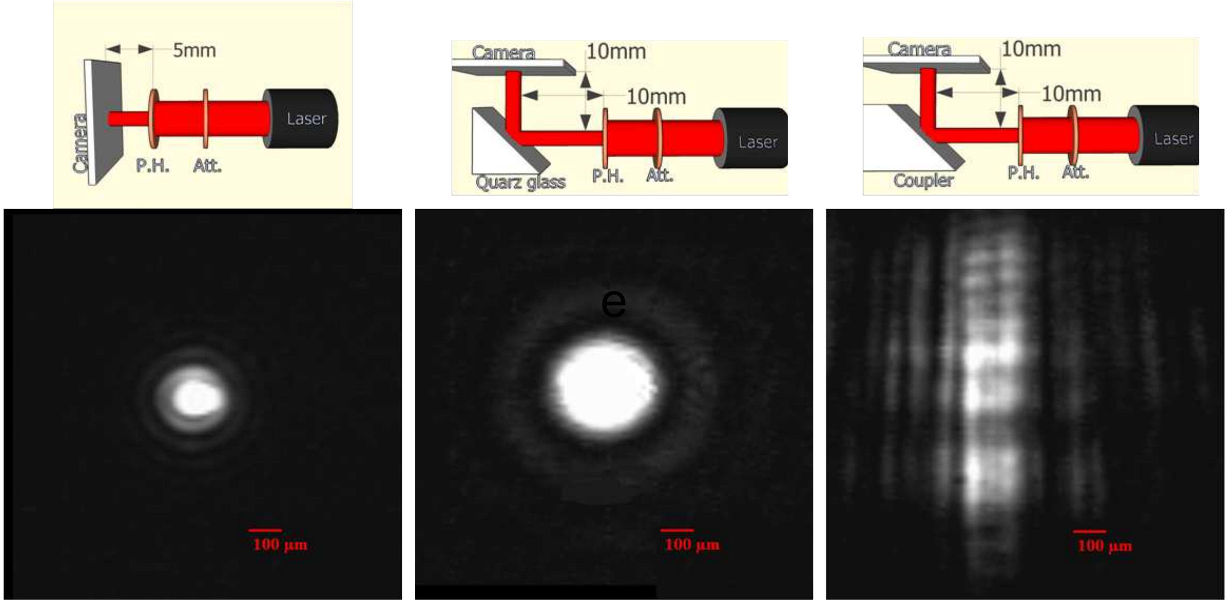

Figure 2.45: Reflective measurement of a 45° SU-8 surface in 3 steps, using a laser, a pinhole, and a camera

In the evaluation of the measurement results the image of the Gaussian beam from step 2 and the reflection from the SU-8 surfaces are first normalized in terms of total energy. For the energy spread in x- and y-direction the values, once along the columns and once along the rows, are accumulated. The results are set in relation to the Gaussian beam, by normalizing the abscissa to σ_i of the Gaussian beam at $(1/e^2)$, see figure 2.46.

While the energy spread in x-direction is similar to the Gaussian beam, the spread in y-direction is almost $3\sigma_i$. Whether this characteristic is due to a general curvature of the surface or to localized gradients will be analyzed with the white light interferometer in the next paragraph.

The calculated energy flow through a circular aperture with radius r/σ_2 is plotted in figure 2.47, once for the Gaussian beam, and ten times for different SU-8 surface measurements. Normalizing the encircled energy at $r/\sigma_2 = 1$ for the Gaussian beam to 1, the

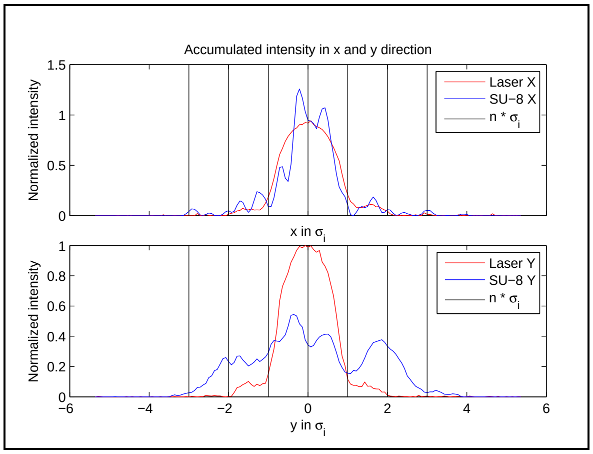

Figure 2.46: Reflective measurement: intensity distribution in x and y direction

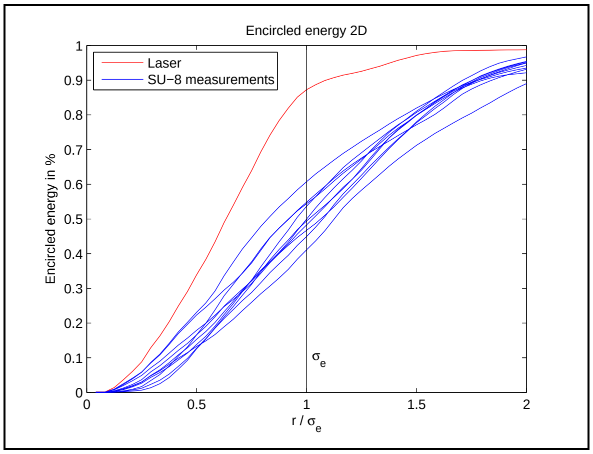

Figure 2.47: Reflective measurement: energy within a circular aperture with radius r/σ_e (10 measurements)

mean efficiency of the reflectors at $r/\sigma_2 = 1$ is 58%. Due to the low sampling number, the standard deviation is calculated by Bessel's corrected formula ($N \rightarrow N-1$) with the measured intensity sampling values y

$$\sigma_{SU8} = \sqrt{\frac{1}{N-1}\sum_{N}(y-\bar{y})^2} \tag{2.30}$$

as $\sigma_{SU8} = 6.5\%$. This result will be interesting for the efficiency analysis of the fiber coupler in the application part of this thesis.

One last note: these measurements are only a first estimation of the reflection losses since some sources of error were not eliminated. These were the unknown total power of the reflection in relation to the Gaussian beam and also the unknown saturation behavior of the camera. The latter error source was partly prevented by the usage of a gray filter.

White light interferometer The white light interferometer (WLI) measurements were performed by the PhD student Sebastian Stoebenau from the TU Ilmenau.

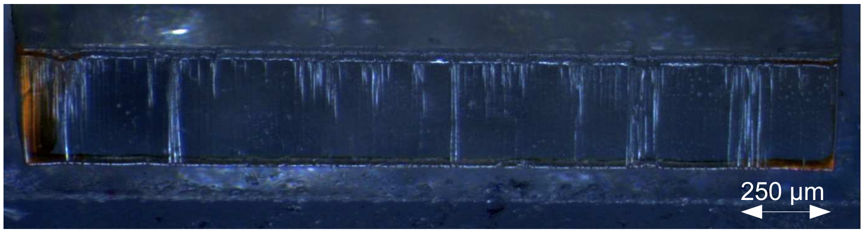

Figure 2.48: Perpendicular view on the 45° SU-8 surface measured by WLI

The test sample was a double exposed SU-8 structure with a structure height of 230 μm and a 2 mm long 45° surface. The structure was fixed on a 45° mount for the measurement. The surface of the structure is shown in figure 2.48.

The structure was chosen because it shows typical distortions in form of riffles but also shows some high quality sectors. The measurement results are depicted in figure 2.49 for the complete surface and for a sector containing a distortion in figure 2.50.

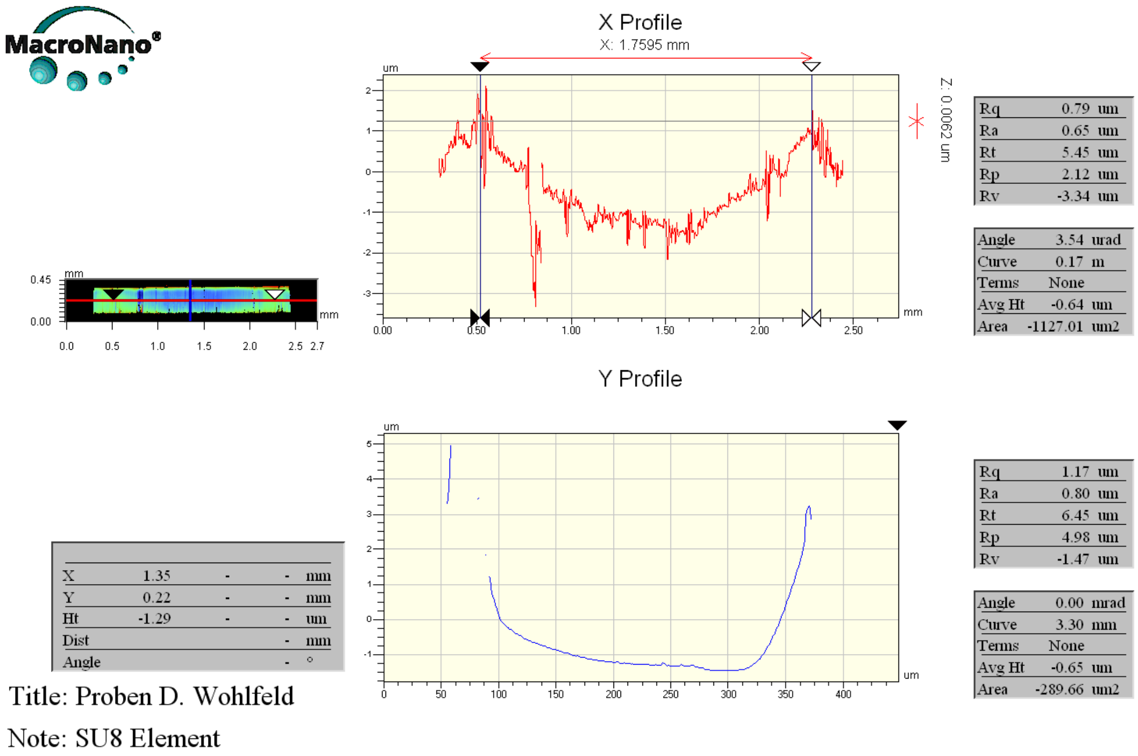

Rq	0.79	um
Ra	0.65	um
Rt	5.45	um
Rp	2.12	um
Rv	-3.34	um

Angle	3.54	urad
Curve	0.17	m
Terms	None	
Avg Ht	-0.64	um
Area	-1127.01	um2

X	1.35	-	-	mm
Y	0.22	-	-	mm
Ht	-1.29	-	-	um
Dist			-	mm
Angle			-	°

Rq	1.17	um
Ra	0.80	um
Rt	6.45	um
Rp	4.98	um
Rv	-1.47	um

Angle	0.00	mrad
Curve	3.30	mm
Terms	None	
Avg Ht	-0.65	um
Area	-289.66	um2

Title: Proben D. Wohlfeld

Note: SU8 Element

Figure 2.49: WLI measurement of the 45° SU-8 surface (TU Ilmenau)

For the complete surface, along the long axis the peak to valley value is $R_T = 5.45\,\mu$m with an RMS roughness of $R_q = 790$ nm and along the short axis the peak to valley value is $R_T = 6.45\,\mu$m with an RMS roughness of $R_q = 1.17\,\mu$m. The RMS roughness here is primary to the form distortion of the surface and not to the real surface roughness. In the smaller surface section, the RMS roughness is reduced to $R_q = 374$ nm. The maximum peak to valley value is $R_t = 3.34\,\mu$m giving an upper estimation limit of the depth of the riffles of less than 3 μm.

2.2.7.3 Summary

For inclined exposure, the angular accuracy is in the order of ±1° over 80% of the surface and the contour within ±3 μm for the inner 90% of the surface. The clear visible riffles

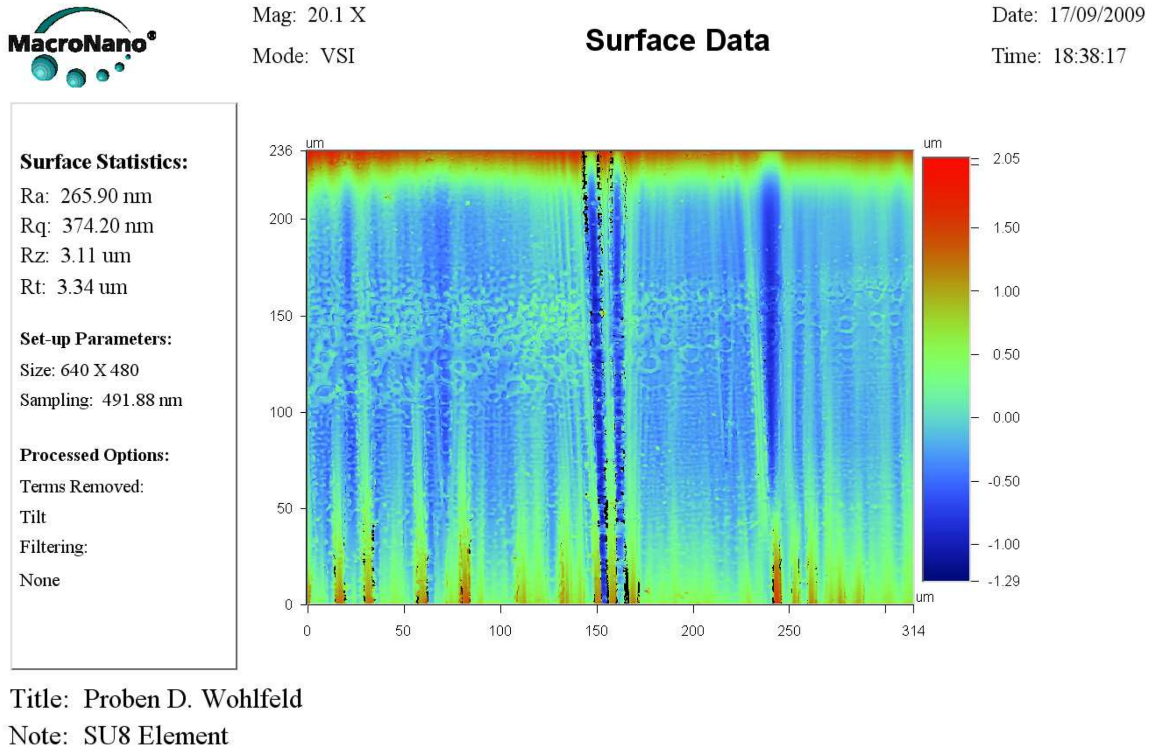

Mag: 20.1 X
Mode: VSI

Surface Data

Date: 17/09/2009
Time: 18:38:17

Surface Statistics:
Ra: 265.90 nm
Rq: 374.20 nm
Rz: 3.11 um
Rt: 3.34 um

Set-up Parameters:
Size: 640 X 480
Sampling: 491.88 nm

Processed Options:
Terms Removed:
Tilt
Filtering:
None

Title: Proben D. Wohlfeld
Note: SU8 Element

Figure 2.50: WLI measurement of a sector containing a distortion (TU Ilmenau)

along the light propagation direction are less than 3 μm from peak to valley. The surface RMS roughness is about 350 nm. Finally, the reflective measurement showed that about 58% of a laser's energy are reflected on SU-8 surfaces within σ of the laser. The reflection is distorted by the local gradients and not by a general contour of the surface.

2.3 Ultra precision machining and other fabrication methods

The previous paragraphs presented techniques to fabricate miniaturized structures in thick resist with UV lithography. Inclined and multi exposure increase the degree of freedom of such structures and enable new functionality for example with integrated micro prisms. Other fabrication techniques for slanted SU-8 structures are described for example by Chang et al. [10] who used the effect of overexposure to generate slanted sidewalls with 54°.

In the past decade, photolithography was the main fabrication technique for structures in the regions of several microns up to a few millimeters. But micro precision machining kept advancing and is nowadays in competition with lithography in thick resist; free form surfaces with position accuracy of $< 0.5\,\mu$m and surface roughnesses $Rq < 10\,$nm for microscale production (Brecher et al. [2]) are achieved with sophisticated tool path methods (Brinksmeier et al. [6]). The combination of free form surfaces with optical surface qualities and high accuracy over large areas enables new miniaturized components which are not possible in standard photolithography. Figure 2.51 shows a beam splitter master for a parallel confocal microscope fabricated by ultra precision machining, and figure 2.52 shows the white light interferometer roughness measurement, both from LFM Bremen. Another advantage of precision machining is the freedom in the choice of material from metals to PMMA where in lithography additional steps are needed to transfer the pattern of the resist into another material. But there is still one important drawback with precision machining. The geometric freedom of producible structures is limited by the tool size used. Structures with high aspect ratio and little space in between are still restricted to lithography in thick resist. This limitation is mentioned here because the direct fiber coupling arrays with a pitch of $250\,\mu$m in the application part of this thesis are not producible with ultra precision machining at this time.

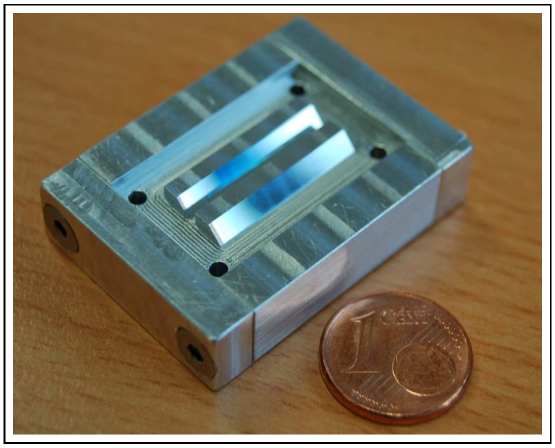

Figure 2.51: Beam splitter master for parallel fluorescence microscopy fabricated by ultra precision machining (LFM Bremen)

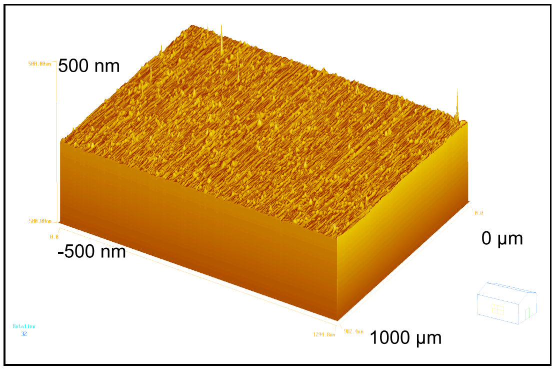

Figure 2.52: White light interferometer roughness measurement of the beam splitter master, $R_a = 4\,$nm and $R_q = 6\,$nm (LFM Bremen)

One other interesting technique has to be mentioned here: direct laser writing based on two photon processes in resist which was demonstrated by Sun et al. [51]. In this method, the resist is exposed by focused 100 fs, 800 nm laser pulses which only provide enough intensity for the two photon processes in the focus region. Deubel et al. [15] fabricated 3D structures in SU-8 and showed a minimum structure size of $< 200\,$nm.

2.4 Conclusion

Three properties are important for conventional mask aligners: intensity in the luminous region, uniformity, and the angular spectrum. The decisive element is the homogenizer in the focal plane of the elliptical reflector. Fly's eye condensers and light rods produce uniform light distributions, but the analysis showed that fly's eye condensers are the best choice for illumination systems in lithography. One has to decide how important the three main properties, mentioned above, are for the process. In this thesis, the angular spectrum is of more importance than uniformity and power, thus an aperture with $r = 8.5\,\mathrm{mm}$ was mounted into the OAI mask aligner. The aperture reduces the angular spectrum from ±3.3° down to ±1.7° while keeping the other parameters in a tolerable region.

Photolithography in thick resist and ultra precision machining enable many new concepts for miniaturized systems, each fabrication technique with its advantages and disadvantages. Photolithography in thick resist depends strongly on the exposure dose and the structure height. In order to determine the exposure dose, the intensity in the resist has to be calculated according to the Fresnel coefficients. Slanted structures with more than 36° require index matching on all interfaces and additional components like coupling prisms. A new inclined exposure setup was introduced to reduce the handling effort and immersion liquid consumption. Multidirectional exposure, as extension of inclined exposure, further increases the degree of freedom in designing micro structures.

Chapter 3

Replication

The previous paragraphs described different technologies to fabricate miniaturized components. None of them is the best choice concerning large-scale production. Replication techniques based on molding are commonly used for the fabrication of high volumes. Mostly, the mold consists of a hard material, like metal, as negative form of the desired replica. In the replication process, the mold is filled with a temperable or UV curable polymer. After curing, the mold is separated from the polymer and one obtains a negative replica of the master mold. Figure 3.1 illustrates the replication process with a UV curable polymer.

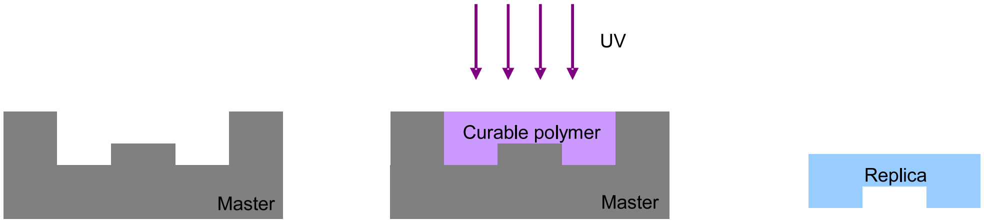

Figure 3.1: Replication process with a UV curable polymer

One well known replication technique of this kind is injection molding. The biggest challenge here is the fabrication of the molding master. Since a hard material is needed, either precision machining is applied or photolithography with an additional step to transfer the features into a suitable material.

An alternative was presented by Xia and Whitesides in 1998, which they called soft lithography [56]. The word Soft Lithography refers to the use of a soft polymer, which serves as a negative master for ensuing molding operations.

In this study direct UV replication was used to replicate a metal master, a beam splitter fabricated by ultra precision machining, in UV adhesive. Soft lithography was used to replicate lithographically produced structures.

3.1 Direct UV replication

UV replication methods use a polymer, which is cured by UV light. Since the curing step is realized with a UV flash, this method is very attractive for large-scale production. The word 'direct' in direct UV replication states that the master structure is directly filled with the polymer. Since most UV curable polymers show similar adhesion to glass and metal, it is beneficial to coat the master structure to reduce the adhesion with the polymer in the separation step, which is critical in UV replication. Some polymers adhere better to glass than to metal, like the UV adhesive from Norland NOA 72 and NOA63. If the bond between master and replica is too strong for simple mechanical separation without damaging the structures, cooling off the system proved to be helpful because the thermal expansion coefficient α_{metal} is smaller than the thermal coefficient of polymers α_{poly}.

Figure 3.2 shows a direct UV replication from the beam splitter from figure 2.51. The UV adhesive used was characterized with stronger adhesion to glass than to metal but the separation was still difficult. It only became possible by using the different thermal expansion coefficients of metal and the polymer.

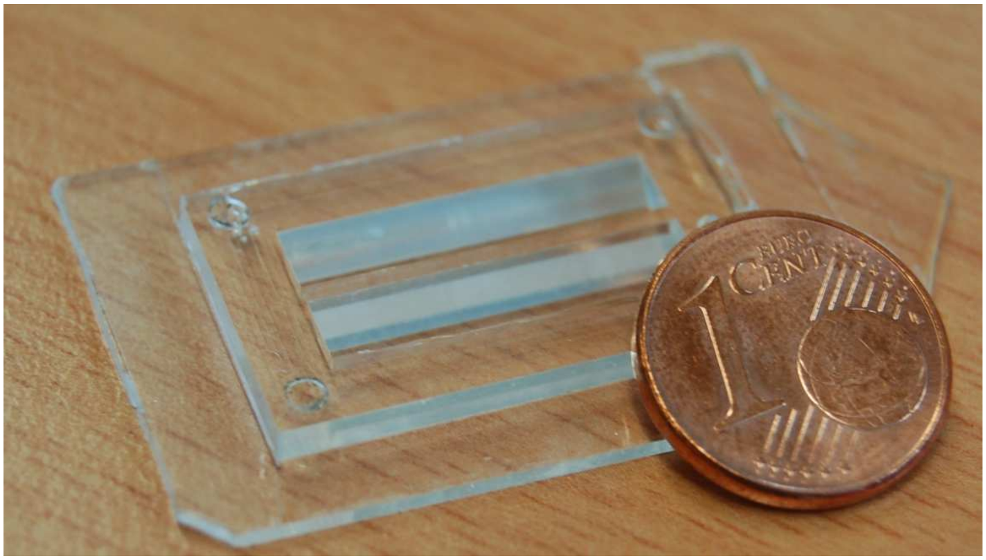

Figure 3.2: Direct UV replication from the beam splitter master depicted in figure 2.51

3.2 Soft Lithography

In direct UV replication, the fabricated structure has to meet the demands of a replication tool, and is therefore often made of metal or similar hard materials, whereas in soft lithography any fabricated structure is suitable, which can be in principle replicated by a molding process. Figure 3.3 illustrates the process steps of soft lithography with PDMS (tridecafluoro-1,1,2,2-tetrahydrooctyl trichlorosilane).

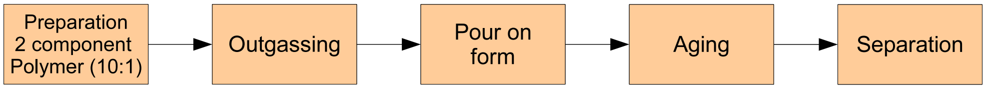

Figure 3.3: Fabrication of a PDMS master

In the first step of this process, PDMS is mixed with a curing agent and put under vacuum for outgassing. The result is a clear viscous liquid, which can easily be poured over the object to replicate. Side walls are used to keep the PDMS within a certain volume. The aging is achieved by keeping the form at room temperature for 24 hours; higher temperatures decrease the aging time. After curing, the PDMS form can be easily separated from the master due to its soft character.

The performance of soft lithography in large-scale production using PDMS stamps was demonstrated recently by Philips and SUSS MicroOptics (Verschuuren et al. [54]). They called the technique 'Substrate Conformal Imprint Lithography' SCIL and characterized it on 150 mm wafers with a sub-100 nm resolution and measured pattern distortion over several square centimeters of less than 0.01%. Another advantage of soft stamps is that the influence of small distortions like particles is locally restricted (see fig. 3.4).

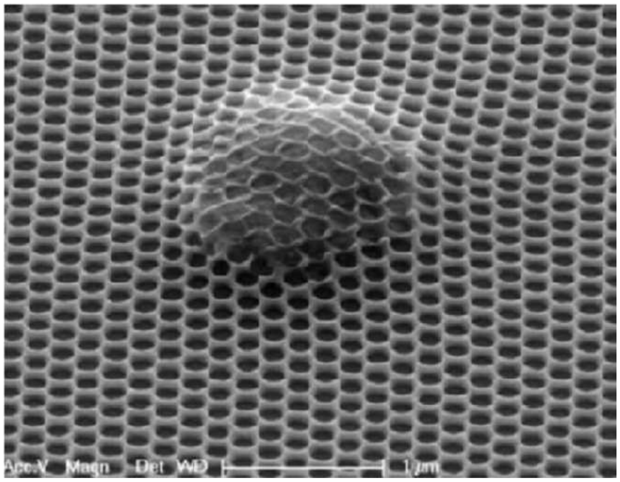

Figure 3.4: Influence of small distortions on the replica (image from Verschuuren et al. [54])

3.2.1 Replica measurements

In his diploma thesis, the student Scheffelmeier [43] characterized and analyzed the accuracy of soft lithography. He found, that the shrinkage from master to PDMS stamp is about 1% and the shrinkage from the UV adhesive NOA65 and NOA61 $< 2\%$.

While shrinkage is a deterministic effect, there are more factors that influence the replication results further. Another comparison between double exposed SU-8 structures and replicas with a small applied pressure showed that the size variation is within $< 2.5\%$, but in this case positive, since pressure deforms the soft PDMS master, see figures 3.5 to 3.7 and table 3.1.

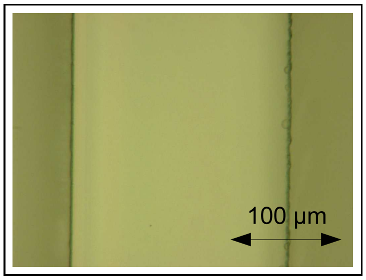

Figure 3.5: SU-8

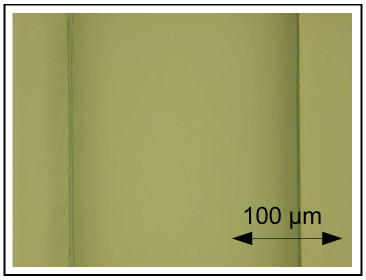

Figure 3.6: PDMS

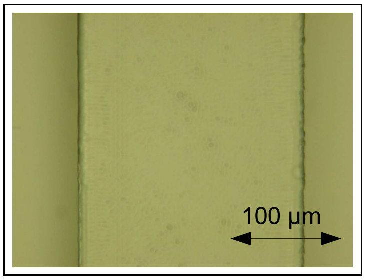

Figure 3.7: NOA

Size mask	Size SU-8	Size PDMS	Size NOA-61
200 μm	204 μm	209 μm	207 μm

Table 3.1: Width variation going from SU-8 via PDMS to NOA

In this measurement, the SU-8 structure was 115 μm high and 204 μm wide. Due to the double exposure, the side walls were not perfectly vertical and became some microns thicker at the bottom. Since all measurements were made at the top of the structures and the top of the PDMS structure is the bottom of its master, the PDMS structure was a bit broader. The NOA structure, a replica from PDMS, corresponded to the original SU-8 structure and was 3 μm thicker. The reason was the applied pressure of about 0.1 N/cm^2 which was needed to minimize the remaining curable polymer between structures and substrate. Since the accuracy was sufficient for the intended applications, the process was not further investigated.

3.2.2 Bias of replicated structures

One problem remains with the replication process. Due to the soft character of the stamp, the pressure on the stamp is limited to small forces, otherwise the stamp deforms. However, the pressure has to be high enough to push unnecessary polymer aside. The layer of remaining polymer, which is not pushed aside, is called bias. The result of a replication without pressure and a 1.5 cm thick stamp is shown in figure 3.9.

The bias was in the order of 300 μm and varied over an area of 1 cm^2 about $\pm 50\,\mu$m.

In applications, where the bias has to be as small as possible and variations in height are only tolerable within some microns, a solution is needed. The main influence on both, the

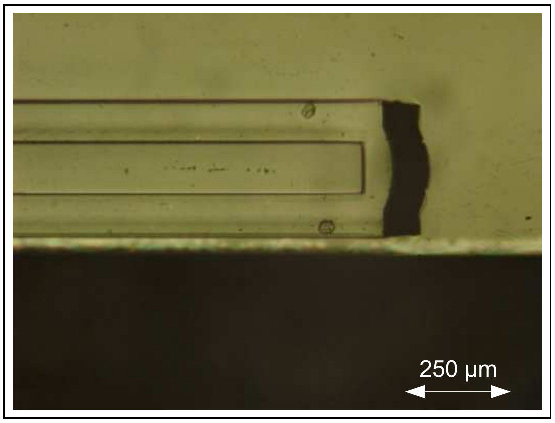

Figure 3.8: Top view on a replicated double exposed SU-8 structure in UV adhesive

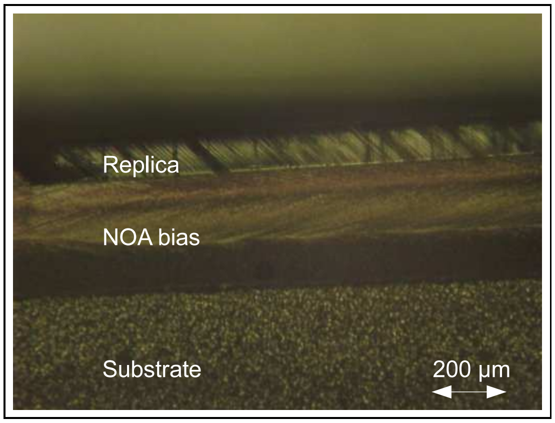

Figure 3.9: Side view on a structure replicated by a 1.5 cm high PDMS stamp

bias and the variations in height, comes from the height of the PDMS stamp. A reduction from 1 cm to 1.5 mm greatly improved the replication behavior. The bias decreased from 300 μm to 40 μm. In this experiment, a small ring with 100 gr was set on top of the substrate to apply some pressure. In a control experiment for the bias, two substrates were glued together by the same UV adhesive and the bias measured. The bias was again 40 μm. Figure 3.10 depicts a sandwich of a replica on a thin substrate (150 μm thick) which was glued on a thicker substrate for handling.

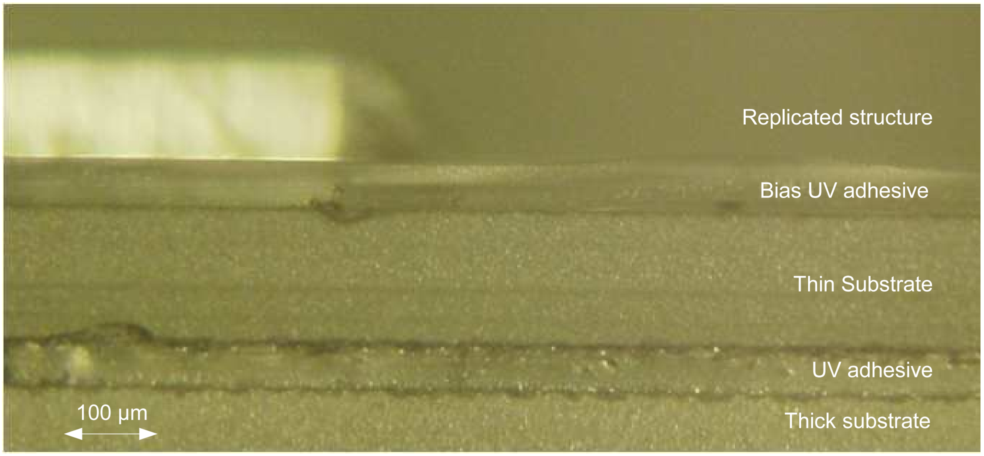

Figure 3.10: Side view on a replica on a thin substrate

The homogeneity of the bias, which was measured on the four corners of a 1 cm^2 square, was within ±14 μm (see fig. 3.11).

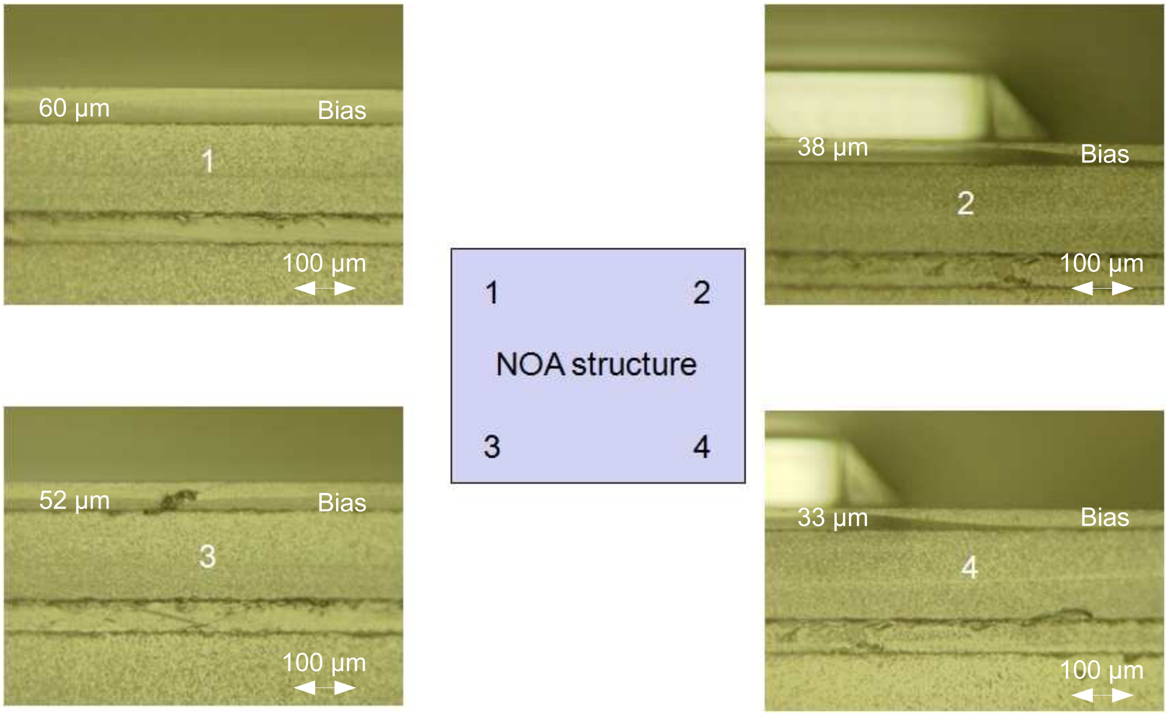

Figure 3.11: Measurement of the bias homogeneity within 1 cm^2

3.3 Conclusion

Direct UV replication and soft lithography are well suited for high volume replication of micro structures. Direct UV replication with hard molds is good for large-scale production as long as the master can be fabricated in the desired material or transfered into it. Depending on the replication material, non-stick coating is necessary. Cooling after aging supports the separation step.

Soft lithography proved to be a proper replication technique for lithographically fabricated structures from several microns up to 1 mm. The advantages of the soft master, i.e. the strength of soft lithography, is also a disadvantage because deformations increase with higher structures. Therefore, the stamp should not be thicker than 2 mm. The bias of the replica polymer is within 40 μm and depends on the applied pressure and the thickness of the PDMS stamp.

Part II

Simulations

Chapter 4

Geometrical optics

The field of light propagation methods is mainly divided into three parts: geometrical optics, wave optics, and quantum optics. Wave optics base on the Maxwell equations, which treat light as an electro magnetic wave and describe the vast majority of optical phenomena. Wave optics are accurate for radiations high enough to omit quantization effects and systems considerably larger than atomic dimensions. Effects, where the dualism of wave and particle behavior of light and its quantization are relevant, are the field of quantum optics.

Geometrical optics are a simplification of wave optics, where the wave nature of light such as interference and polarization effects are omitted. The propagation of light is described by rays which are perpendicular to a corresponding wave front and collinear with the wave vector. Rays bend, if the refraction index changes and travel straight in all other cases. Despite the significant simplification, geometrical optics are a good approximation when the wavelength is small compared to the size of structures with which the light interacts. The majority of optic design simulations are based on geometrical optics.

The development of a customized ray tracer (RayTrace) was part of this thesis. This was required in order to simulate and to optimize coupling efficiencies between light sources and fibers, and in order to analyze the behavior of GRIN lenses. One specific characteristic of the customized ray tracer is the combination of ray tracing in the media, and wave optics on boundaries to calculate the energy transfer according to the Fresnel formula. This chapter covers the generation of rays, reflection on customized surfaces, and the propagation of rays in inhomogeneous media.

4.1 Generation of rays

In illumination simulations, an optical system is often traced with a large number of independent rays ($> 1\,\text{million}$), generated by a random method within defined boundaries. Other methods are differential ray tracing and the Gaussian beam approach. Differential ray tracing in homogeneous media (Cox and King [13]) and in inhomogeneous media (Stone and Forbes [50]) trace base rays with corresponding differential rays close to the base rays. The differential rays describe the propagation of light near the base ray and form, together with the base ray, a light patch. In the Gaussian beam approach (Cerveny et al. [9]), a Gaussian profile is connected with a ray and traced through the system. A challenge in both methods are caustics. This thesis describes another approach. If only the energy within a certain aperture is of interest, it is sufficient to weigh each ray with a corresponding energy and to arrange the rays in a way that a planar surface would be uniformly hit by the rays - each ray with approximately the same distance to its neighbors. This deterministic approach here is fundamentally different from a Monte-Carlo-Simulation.

4.1.1 Gaussian point source

This section describes a deterministic way to generate a ray package which produces a Gaussian energy distribution on a screen. It is based on the far field approximation of the Gaussian beam, which states that the waist σ_z of a Gaussian beam expands linearly:

$$\sigma_z \approx \frac{\lambda \cdot z}{\sigma_0}. \tag{4.1}$$

Here, a Gaussian point source is a point source which generates a Gaussian energy distribution on a screen in distance r from the point source; the surface normal of the screen is parallel to the optical axis and the screen is centered on the optical axis (fig. 4.1).

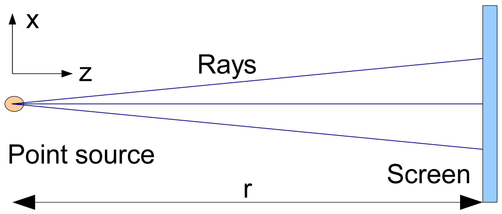

Figure 4.1: Illustration of the setup for the Gaussian point source

The Gaussian energy distribution is attainable by two methods. Either every ray starts with the same energy and the density of the rays on the screen determines the intensity, or the rays are uniformly distributed over the screen and the energy of each ray is adapted.

The second approach requires two steps: uniform ray distribution on a plane and the weighting of rays. The uniform ray distribution on a plane is solved by the optic simulation software Zemax with the following algorithm.

A center ray is surrounded by concentric rings. All rings have the same distance to each other. The first ring starts with m points equally distributed over 2π. Every following ring with Pr_{n+1} points has m more points than the previous one with Pr_n points.

$$\mathrm{Pr}_{n+1} = \mathrm{Pr}_n + m \tag{4.2}$$

The total number of points P as a function of the number of rings N_{rings} is given by:

$$P\left(N_{rings}\right) = 1 + \sum_{i=1}^{N_{rings}} i \cdot m \tag{4.3}$$

In the following, this method with $m = 6$ is referred to as the 'hexa'-method. In this method source rays are determined by the largest source angle ϑ_{max} and the number of desired rings. The largest source angle defines the outer ring with radius r_{max} on a screen centered on the optical axis with the optical axis as normal vector. The other ring radii $(N_{rings} - 1)$ are equally distributed between 0 and r_{max}. On each ring, the rays are equally arranged over 2π. The ray distribution in hexa-mode is illustrated in figure 4.2 for $N_{rings} = 6$ and $m = 6$.

In the hexa-mode, the angles of the source are only sampled by the number of rings N_{rings}. If the energy transfer through a concentric aperture is to be determined, a large number of rings is needed and therefore a large number of rays has to be traced.

A better sampling of the source's angles is achieved in the helix-mode. While in the hexa-mode all rays are equally distributed in 2π along the ring, each ray of the ring with the same radius. In the helix mode, the rays are still equally distributed in 2π along the ring, but the radius for each ray increases in constant steps from r_{n-1} to r_n. The helix-mode is depicted in figure 4.3 also for $N_{rings} = 6$ and $m = 6$.

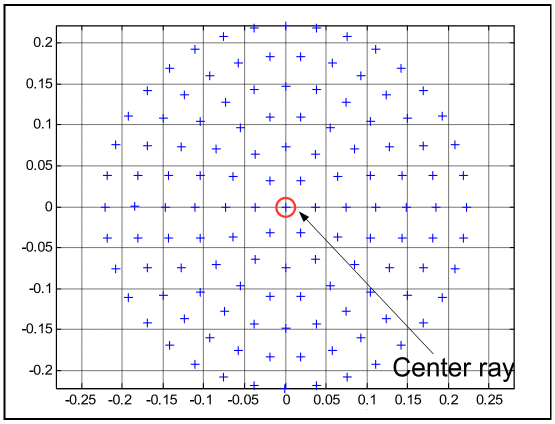

Figure 4.2: Hexa-mode: ray distribution on a screen with $m = 6$ and $N = 6$

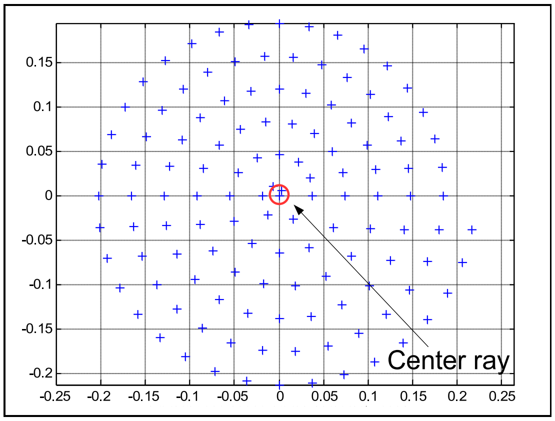

Figure 4.3: Helix-mode: ray distribution on a screen with $m = 6$ and $N = 6$

While the hexa-mode looks quite uniform, the helix-mode does not. The rays are more compact in the middle than in the border area.

For an estimation of the accuracy of the two methods in comparison with a Gaussian intensity profile, the energy inside a concentric aperture with distance d_a from the source is calculated analytically and compared with the ray trace result for different numbers of rings N_{rings}. The radius of the aperture is set to $r_a = \frac{\sigma}{2}$.

In Fourier optics, the Gaussian function is defined as

$$g_1(x) = \frac{1}{\sigma} e^{-\pi\left(\frac{x}{\sigma}\right)^2} \tag{4.4}$$

with

$$\int \frac{1}{\sigma} e^{-\pi\left(\frac{x}{\sigma}\right)^2} dx = 1. \tag{4.5}$$

In 2 dimensions, the gaussian function for $\sigma_x = \sigma_y$ is

$$g_2(x) = \frac{1}{\sigma^2} e^{-\frac{\pi}{\sigma^2}\left(x^2+y^2\right)}. \tag{4.6}$$

The encircled energy is calculated by

$$\begin{aligned} E_{rev} &= \frac{1}{\sigma^2} \int_0^{2\pi} \int_0^{\frac{\sigma}{2}} e^{-\frac{\pi}{\sigma^2} r^2}\, r\, dr\, d\phi \qquad (4.7) \\ E_{rev} &= 1 - e^{-\frac{\pi}{\sigma^2}\left(\frac{\sigma}{2}\right)^2} \\ E_{rev} &= 1 - e^{-\frac{\pi}{4}} \\ E_{rev} &= 0.54406. \end{aligned}$$

The normalized reference energy within an aperture of $r_a = \frac{\sigma}{2}$ is 0.54406.

The rays generated by the ray tracer are within a certain angle ϑ_{max}. This angle determines the radius of the outer ring R_{max} on the screen and it also corresponds to σ of the Gaussian weight function. After all rays are generated, the total energy of all rays is normalized to 1. In the simulation in figure 4.4 an aperture was set right in front of the screen with an aperture size of $R_{max}/2$. The energy behind the aperture was simulated for the hexa, the helix, and a mixed mode $(hexa + helix)/2$ with increasing N_{rings}. Since the ray tracer only simulates rays within σ, the results were once more normalized by $1 - e^{-\pi} \approx 0.9568$, the energy within σ of the Gaussian weight function.

The figures show that both modes converge towards a value near the reference, the hexa-mode from the bottom, the helix-mode from the top. The oscillations of the hexa-mode are a result of their ring structure, either a complete ring is cut off by the aperture or not. The similar converging behavior from two sides suggests a combination of both modes into a mixed mode. The relative error (see fig. 4.5) of the mixed mode for $N_{Rings} > 40$ is smaller than 1% ($N_{Rings} = 40$ in mixed-mode equals to less than 10k rays).

4.1.2 Gaussian area source

The previous section presented a deterministic way to simulate a Gaussian point source with a package of rays. This is a fair approximation for a point source in the far field like VCSEL. For the simulation of area sources, like the end surface of a fiber, a new Gaussian area source is needed.

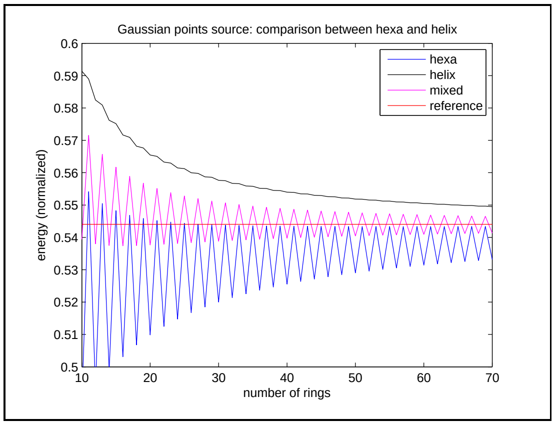

Figure 4.4: Comparison between hexa, helix, and mixed mode of the ray tracer with the analytical reference 0.54406

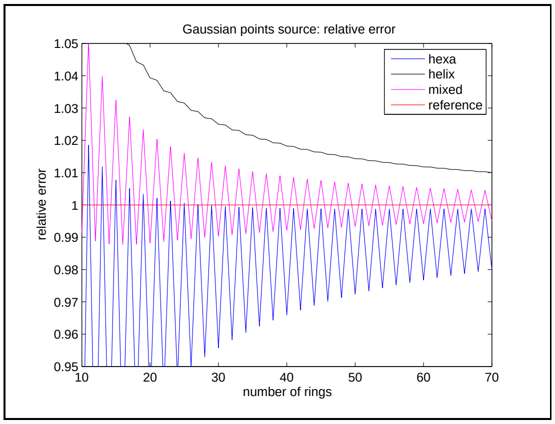

Figure 4.5: Relative error: hex, helix, and mixed mode

A fiber, in a first approximation, is a cylindrical light rod which uniforms a given light distribution by convolution (see section 2.1.4 on page 17). Every point on the end surface of the fiber is therefore an image of the source. If a Gaussian beam is coupled into the fiber, each light source on the end surface is also a Gaussian point source. The final light distribution L is then given by the superposition of all Gaussian point sources which corresponds to a convolution of the fiber core surface A_{fiber} with the Gaussian function g_2:

$$L(x, y) = c_{norm} \cdot g_2(x, y) * A_{fiber}(x, y) \tag{4.8}$$

with

$$A_{fiber}(x, y) = \begin{cases} 1, & \text{if } \sqrt{x^2 + y^2} \leq r_f \\ 0, & \text{else} \end{cases},$$

c_{norm} to normalize the total output, and the fiber core radius r_f.

Accordingly, the rays in the ray tracer for an area source are generated in 3 steps: generation of a uniform point distribution on the surface (hexa, helix, or mixed), replacement of each point by a point source, and normalizing of the energy. Gaussian point sources and the generation of uniform point distribution in a certain area were already described in the previous section. Area sources, generated by this method, are shown for $N_{rings} = 3$ in the figures: hexa-mode 4.6, helix-mode 4.7, and mixed-mode 4.8.

For validation, the following system is traced: area source $r_f = 31.25\,\mu\text{m}$, $\vartheta_{src} = 12.5°$, aperture size $r_a = 25\,\mu\text{m}$ in different distances d from the screen, and the results compared with the reference value.

The reference value for a certain propagation distance d through an aperture r_a is calculated by setting σ of the Gaussian function to $\sigma = \tan(\vartheta_{max}) \cdot d$ on the screen, convolution of g_2 with the fiber core area A_{fiber}, normalization of the energy on the screen

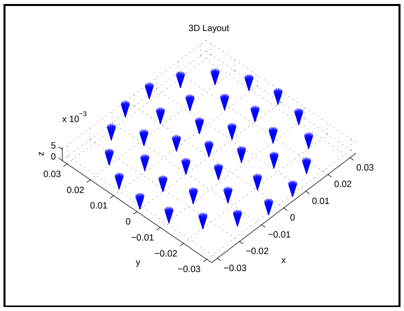

Figure 4.6: 2D hexa-mode

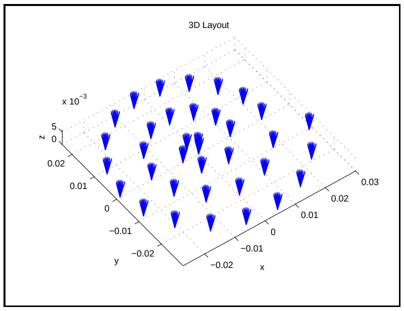

Figure 4.7: 2D helix-mode

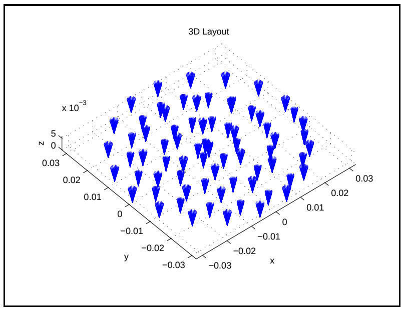

Figure 4.8: 2D mixed-mode

to 1, and accumulation of all energy distributions within the aperture with radius r_a.

$$E_{ref} = \iint\limits_{Aperture} \left[c_{norm} \cdot \left(g_2\left(\sigma, x, y\right) * A_{fiber}\left(x, y\right) \right) \right] dx\, dy, \tag{4.9}$$

with

$$A_{aperture}\left(x, y\right) = \begin{cases} 1, & \text{if } \sqrt{x^2 + y^2} \leq r_a \\ 0, & \text{else} \end{cases} .$$

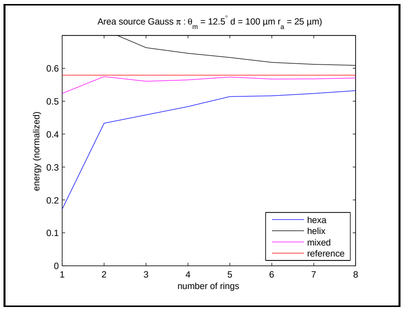

Figure 4.9: Area Source with σ_o, $d = 100\,\mu$m

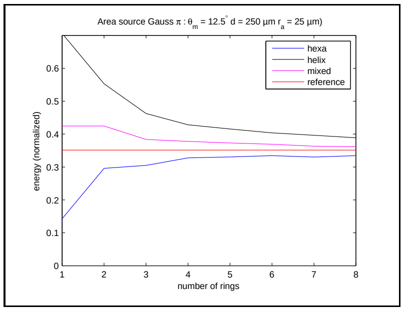

Figure 4.10: Area source with σ_o, $d = 250\,\mu$m

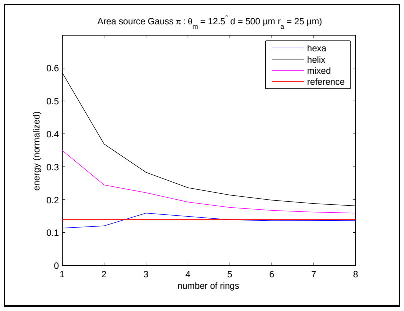

Figure 4.11: Area source with σ_o, $d = 500\,\mu$m

In this comparison, the rays of a Gaussian point source were generated within σ_o of the Fourier optic Gauss function (see formula 4.4). In praxis, the angular characteristics of VCSELs are often given by an angle ϑ_{max} and an appendix which states: $\frac{1}{e^2}$. Therefore, the rays for VCSEL sources have to be generated with another σ, the technical σ_v:

$$\sigma_v = \sqrt{\frac{2}{\pi}}\sigma_o \tag{4.10}$$

To evaluate, if another σ changes the results of the comparison, the validation was repeated with σ_v and is shown in the figures 4.12 to 4.14.

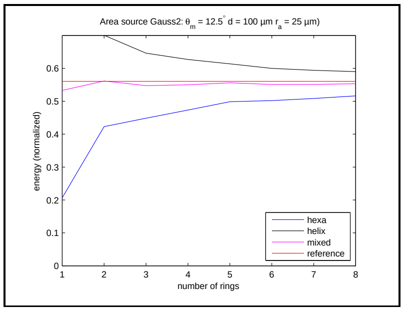

Figure 4.12: Area Source with σ_v, $d = 100\,\mu$m

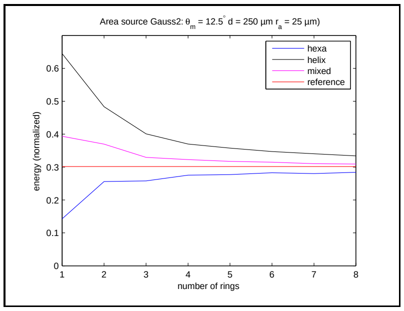

Figure 4.13: Area source with σ_v, $d = 250\,\mu$m

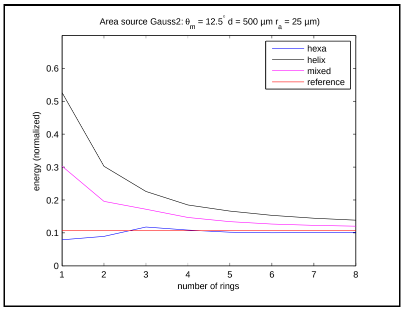

Figure 4.14: Area source with σ_v, $d = 500\,\mu$m

The comparisons show equal behavior for both σ. The question, which method (hexa, helix, or mixed) is the best choice, depends on the number of rays passing the aperture. For high ray counts, the mixed mode performs better. The hexa-mode again becomes better with low ray counts passing the aperture. In summary, for the described examples, the simulation accuracy of the area source is within ±2% for $N_{rings} \geq 4$.

4.1.3 Number of generated rays

The previous comparisons between the different ray generation modes, hexa, helix, or mixed, compared the number of rings and not the number of total rays generated. Since the latter determines the computation time, this paragraph briefly describes the relation of generated rays to the number of rings for 1D and 2D sources.

The relation for 1D sources is depicted in figure 4.15 while figure 4.16 depicts the relation for 2D sources. In the 1D case, the number of generated rays for the mixed mode is twice the rays generated by helix or hexa mode. In the 2D case, the number of generated rays for the mixed mode is four times the rays generated by helix or hexa mode.

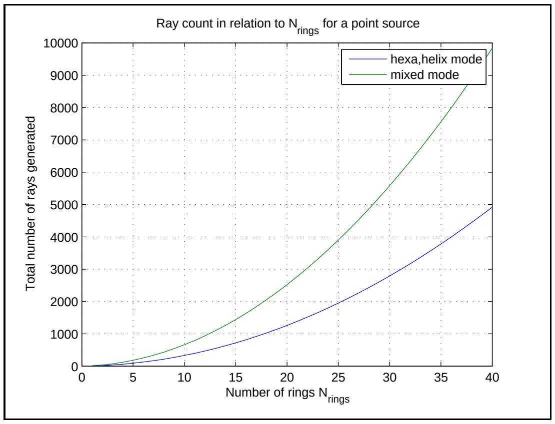

Figure 4.15: Total number of generated rays for point sources in the different modes

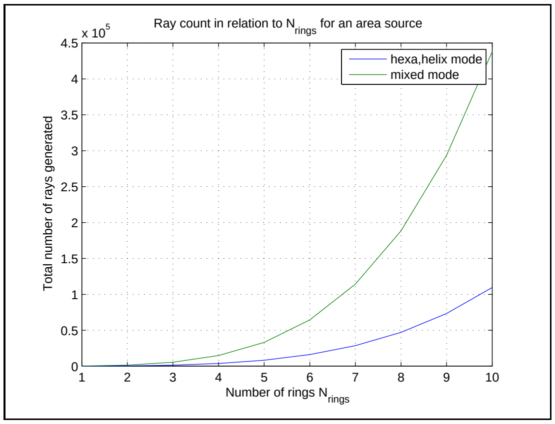

Figure 4.16: Total number of generated rays for point sources in the different modes

In summary, the mixed mode still improves the accuracy, considering equal numbers of generated rays. For 2D sources and restrictive apertures, the hexa mode performs best.

4.2 Customized surfaces

The intersection of rays with surfaces is the core of every ray tracer, but not every surface is available. For the simulation of coupling efficiencies and its optimization, reflections on the inside of slanted cylinder and ellipsoids will be described in the following section.

4.2.1 Slanted cylinder

The surface of a slanted cylinder is described by

$$\vec{P_c} = \vec{r_c} + \beta \cdot \vec{s_c} + R_c \begin{pmatrix} \cos t \\ \sin t \\ 0 \end{pmatrix} \tag{4.11}$$

and depicted in figure 4.17.

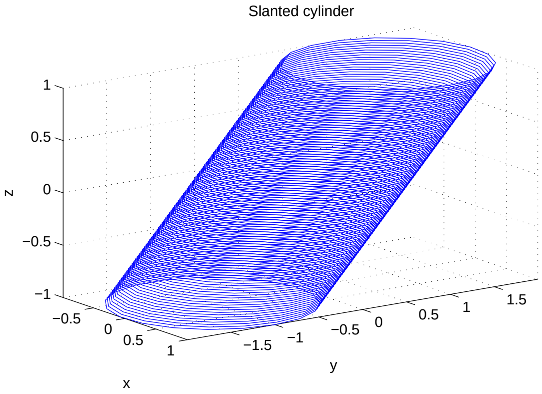

Figure 4.17: Slanted cylinder with $s_c = (0\,,1\,,1)$ and $R_c = 1$

4.2.1.1 Intersection

A straight line with $\vec{G} = \vec{r_g} + \lambda \cdot \vec{s_g}$ intersects with the cylinder if $\vec{P_c} = \vec{G}$.

$$\begin{aligned}
\vec{r}_g + \lambda \cdot \vec{s}_g &= \vec{r}_c + \beta \cdot \vec{s}_c + R_c \begin{pmatrix} \cos t \\ \sin t \\ 0 \end{pmatrix} \\
0 &= \lambda \cdot \vec{s}_g - \beta \cdot \vec{s}_c - R_c \begin{pmatrix} \cos t \\ \sin t \\ 0 \end{pmatrix} + (\vec{r}_g - \vec{r}_c) \,. \qquad (4.12)
\end{aligned}$$

The z-component gives a condition for λ:

$$\begin{aligned}
\lambda \cdot s_{gz} - \beta \cdot s_{cz} + (r_{gz} - r_{cz}) &= 0 \\
\lambda \cdot s_{gz} - \beta \cdot s_{cz} + r_{dgcz} &= 0 \\
\lambda &= \frac{\beta \cdot s_{cz} - r_{dgcz}}{s_{gz}} \qquad (4.13)
\end{aligned}$$

with $r_{dgcz} = (r_{gz} - r_{cz})$.

Here, a case differentiation is needed. If $s_{gz} = 0$, the straight line is within the xy-plane, otherwise the general case has to be calculated.

In the case $s_{gz} = 0$ the condition from the z-component is simplified to

$$r_{gz} = r_{cz} + \beta \cdot s_{cz}$$

and one derives the condition for β with

$$\beta = \frac{r_{gz} - r_{cz}}{s_{cz}}. \qquad (4.14)$$

With β, the offset center point of the cylinder P_{co} is

$$\vec{P}_{co} = \vec{r}_c + \beta \cdot \vec{s}_c \qquad (4.15)$$

and the start equation $\vec{P}_c = \vec{G}$ becomes

$$\vec{r}_g + \lambda \cdot \vec{s}_g - \vec{P}_{co} = R_c \begin{pmatrix} \cos t \\ \sin t \\ 0 \end{pmatrix} . \qquad (4.16)$$

Taking the square of the equation and a substitution of $\vec{p} = \vec{r}_g - \vec{P}_{co}$, it becomes

$$\begin{aligned} \left(\lambda \cdot \vec{s}_g + \vec{p}\right)^2 &= R_c^2 \\ \lambda^2 \left(\vec{s}_g\right)^2 + 2\lambda \left(\vec{s}_g \cdot \vec{p}\right) + \left(\left(\vec{p}\right)^2 - R_c^2\right) &= 0, \end{aligned}$$

a standard quadratic equation which delivers λ_1 and λ_2.

In the general case with

$$\vec{R}_c = R_c \begin{pmatrix} \cos t \\ \sin t \\ 0 \end{pmatrix}$$

the equation $\vec{P}_c = \vec{G}$ becomes

$$\begin{aligned} \lambda \cdot \vec{s}_g - \beta \cdot \vec{s}_c - \vec{R}_c + \vec{r}_{dgc} &= 0 \\ \frac{\beta \cdot s_{cz} - r_{dgcz}}{s_{gz}} \cdot \vec{s}_g - \beta \cdot \vec{s}_c - \vec{R}_c + \vec{r}_{dgc} &= 0 \\ \beta \cdot \left(\frac{s_{cz}}{s_{gz}} \cdot \vec{s}_g - \vec{s}_c \right) - \vec{R}_c + \vec{r}_{dgc} - \frac{r_{dgcz}}{s_{gz}} \cdot \vec{s}_g &= 0 \\ \beta \cdot \left(\frac{s_{cz}}{s_{gz}} \cdot \vec{s}_g - \vec{s}_c \right) &= \vec{R}_c - \vec{r}_{dgc} + \frac{r_{dgcz}}{s_{gz}} \cdot \vec{s}_g \end{aligned}$$

with $\vec{q} = \vec{r}_{dgc} - \frac{r_{dgcz}}{s_{gz}} \cdot \vec{s}_g$

$$\beta \cdot \left(\frac{s_{cz}}{s_{gz}} \cdot \vec{s}_g - \vec{s}_c \right) = \vec{R}_c - \vec{q}. \tag{4.17}$$

Splitting this equation in the x and y component and with $a_x = \left(\frac{s_{cz}}{s_{gz}} \cdot s_{gx} - s_{cx} \right)$ and $a_y = \left(\frac{s_{cz}}{s_{gz}} \cdot s_{gy} - s_{cy} \right)$ one derives the two equations:

$$\beta \cdot a_x = R_c \cos t - q_x \tag{4.18}$$

$$\beta \cdot a_y = R_c \sin t - q_y. \tag{4.19}$$

β_1 and β_2 result from the following quadratic equation

$$\begin{aligned} R_c^2 &= \left(\beta \cdot a_x + q_x\right)^2 + \left(\beta \cdot a_y + q_y\right)^2 \\ 0 &= \beta^2 \left(a_x^2 + a_y^2\right) + \beta \cdot 2 \left(a_x q_x + a_y q_y\right) + \left(q_x^2 + q_y^2 - R_c^2\right) \qquad (4.20) \end{aligned}$$

and deliver λ_1 and λ_2 by inserting them into equation 4.13.

4.2.1.2 Reflection

The law of reflection determines the new direction vector $\vec{s_2}$ of a ray as function of its direction $\vec{s_1}$ and the surface normal $\vec{N}$

$$\vec{s_2} = \vec{s_1} - 2\left(\vec{s_1}\cdot\vec{N}\right)\cdot\vec{N}. \tag{4.21}$$

The tangential vectors on a surface given by an equation in parameter form are derived by derivation of the equation to its parameters. The tangential vector for a slanted cylinder in respect to β and t are:

$$\begin{aligned}\vec{t_1} &= \vec{s_c}\\ \vec{t_2} &= \begin{pmatrix}-\sin t\\ \cos t\\ 0\end{pmatrix}.\end{aligned}$$

The normal vector $\vec{N}$ results from the cross product $\vec{N} = \vec{t_1}\times\vec{t_2}$

$$\vec{N} = \vec{s_c}\times\begin{pmatrix}-\sin t\\ \cos t\\ 0\end{pmatrix}. \tag{4.22}$$

This equation requires the calculation of parameter t for the point of intersection. Starting with the two equations 4.18 and 4.19 which can be written as

$$\begin{aligned}\frac{\beta_1\cdot a_y + q_y}{\beta_1\cdot a_x + q_x} &= \frac{R_c\sin t}{R_c\cos t}\\ \tan t &= \frac{\beta_1\cdot a_y + q_y}{\beta_1\cdot a_x + q_x}.\end{aligned}$$

t_1 and t_2 are derived by the atan2 function

$$t_1 = \operatorname{atan2}\left(\beta_1\cdot a_y + q_y\,,\ \beta_1\cdot a_x + q_x\right) \tag{4.23}$$

$$t_2 = \operatorname{atan2}\left(\beta_2\cdot a_y + q_y\,,\ \beta_2\cdot a_x + q_x\right). \tag{4.24}$$

The parameters t_1 and t_2 are also useful in order to decide which of the two intersection points are of interest, simply by choosing the quadrant of interest.

This concludes the description of the slanted cylinder.

4.2.2 Ellipsoid

An ellipsoid is the 3D version of an ellipse. It is described in 2 ways: the parametric form

$$\left(\frac{x}{a}\right)^2+\left(\frac{y}{b}\right)^2+\left(\frac{z}{c}\right)^2=1 \tag{4.25}$$

or by its axises $\vec{s_x}$, $\vec{s_y}$, $\vec{s_z}$, and an offset point $\vec{P_o}$

$$\vec{s_x}=a\begin{pmatrix}1\\0\\0\end{pmatrix}\quad,\quad \vec{s_y}=b\begin{pmatrix}0\\1\\0\end{pmatrix}\quad,\quad \vec{s_z}=c\begin{pmatrix}0\\0\\1\end{pmatrix}. \tag{4.26}$$

The first description is useful for the calculation of the normal vector $\vec{N}$ and the second one simplifies the calculation of the intersection with a ray.

4.2.2.1 Intersection

The intersection of a ray with an ellipsoid is simplified by a mathematical trick, which scales the ray in a way that the intersection with the ellipsoid equals the intersection with a sphere and the scaled ray.

Let $\boldsymbol{T}$ be a matrix composed of the three axis vectors $\vec{s_x}$, $\vec{s_y}$, and $\vec{s_z}$ multiplied with a rotation matrix $\boldsymbol{D}$ which is used to rotate the ellipsoid in any direction

$$\boldsymbol{T}=\boldsymbol{D}\cdot\left[\vec{s_x}\ \vec{s_y}\ \vec{s_z}\right] \tag{4.27}$$

with $\boldsymbol{D}$ being any combination of the three rotation matrix

$$D_x=\begin{pmatrix}1&0&0\\0&\cos\alpha&-\sin\alpha\\0&\sin\alpha&\cos\alpha\end{pmatrix} D_y=\begin{pmatrix}\cos\alpha&0&\sin\alpha\\0&1&0\\-\sin\alpha&0&\cos\alpha\end{pmatrix} D_z=\begin{pmatrix}\cos\alpha&-\sin\alpha&0\\\sin\alpha&\cos\alpha&0\\0&0&1\end{pmatrix}. \tag{4.28}$$

The position vector $\vec{r_g}$ and the direction vector $\vec{s_g}$ of the ray are transformed by

$$\begin{aligned}\vec{r}_{gT} &= \boldsymbol{T}^{-1}\cdot\left(\vec{r_g}-\vec{P_o}\right) &(4.29)\\ \vec{s}_{gT} &= \boldsymbol{T}^{-1}\cdot\vec{s}_g. &(4.30)\end{aligned}$$

Now, only the intersection of the transformed ray with a sphere with $R=1$ has to be calculated

$$\begin{aligned}\left|\vec{r}_{gT}+\lambda\vec{s}_{gT}\right|^2&=1\\ \lambda^2\left(\vec{s}_{gT}\right)^2+2\lambda\left(\vec{r}_{gT}\vec{s}_{gT}\right)+\left(\vec{r}_{gT}\right)^2-1&=0\end{aligned}$$

and the derived λ_1 and λ_2 inserted into the original ray equation

$$\vec{P} = \vec{r}_g + \lambda \cdot \vec{s}_g \tag{4.31}$$

to get the intersection points.

4.2.2.2 Reflection

The normal of the surface at the intersection point P_i is derived by rotating and moving the point P_i in such a way back that the corresponding ellipsoid is rotated and moved into the origin with its axis parallel to the axis of the coordinate system

$$\vec{P}_{iT} = \boldsymbol{D}^{-1} \cdot \left(\vec{P}_i - \vec{P}_o\right). \tag{4.32}$$

The normal to the transformed ellipsoid is given by the gradient of formula 4.25 and the insertion of the transformed point $\vec{P}_{iT}$

$$\begin{aligned} \vec{N_T} &= \vec{\nabla}\left[\left(\frac{x}{a}\right)^2 + \left(\frac{y}{b}\right)^2 + \left(\frac{z}{c}\right)^2 - 1\right] \\ \vec{N_T} &= \left(\frac{2 \cdot P_{ix}}{a}\right)\vec{e}_x + \left(\frac{2 \cdot P_{iy}}{b}\right)\vec{e}_y + \left(\frac{2 \cdot P_{iz}}{c}\right)\vec{e}_z. \end{aligned} \tag{4.33}$$

In the last step, $\vec{N_T}$ has to be rotated back and normalized

$$\begin{aligned} \vec{N_e} &= \boldsymbol{D} \cdot \vec{N_T} \\ \vec{N} &= \frac{N_e}{|N_e|}. \end{aligned} \tag{4.34}$$

The characteristic of an ellipsoid, in which all rays coming from a point source in the first focal point are reflected into the second focal point, is now used to validate the formula and the implementation. Figure 4.18 shows the predicted behavior.

4.3 Energy transfer

The transmissivity and reflectiviy on index boundaries was already discussed in section 2.2.4.2 on page 26 for plane waves. Rays can be seen as a simplified representation of wave fronts carrying a certain energy E. For each interaction with index boundaries, the energy of the ray has to be recalculated. Depending on the polarization, and if reflection or transmission is regarded, the energy is adjusted by

$$Er_{\perp,||} = E_i \cdot \left(r_{\perp,||}\right)^2 \tag{4.35}$$

$$Et_{\perp,||} = E_i \cdot \left(t_{\perp,||}\right)^2 \frac{n_t cos\theta_t}{n_i cos\theta_i} \tag{4.36}$$

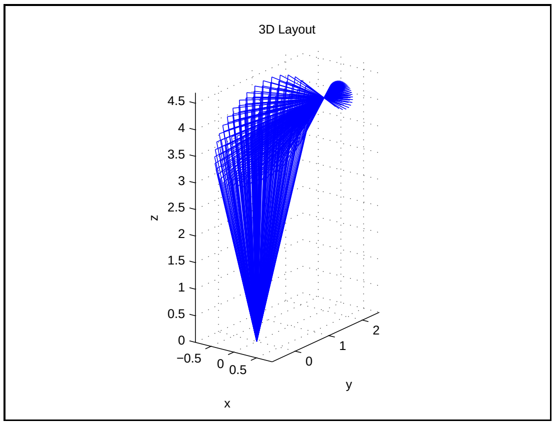

Figure 4.18: RayTrace simulation of a point source positioned in the focal point of an elliptical mirror (on the bottom) which perfectly focuses the rays into the second focal point

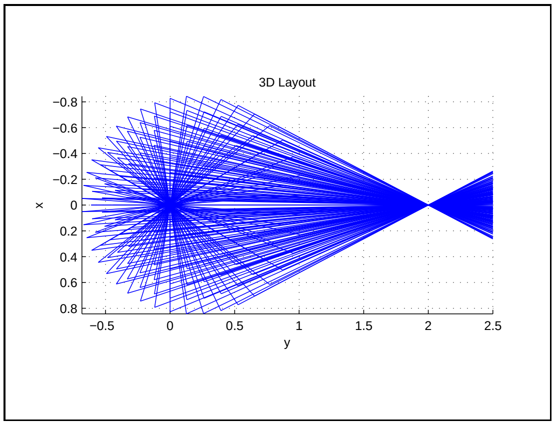

Figure 4.19: Top view

and for unpolarized light by

$$Er = E_i \cdot \frac{1}{2}\left(r_{\perp}^2 + r_{||}^2\right) \tag{4.37}$$

$$Et = E_i \cdot \frac{1}{2}\left(t_{\perp}^2 + t_{||}^2\right)\frac{n_t cos\theta_t}{n_i cos\theta_i}. \tag{4.38}$$

with E_i being the energy of the incident ray. The differences of the energy transfer regarding the transmission of parallel rays through a prism with two different orientations are depicted in figure 4.20.

4.4 Inhomogeneous media

Ray tracing in inhomogeneous media is based on solving the ray equation. Analytical solutions are only known for some gradient index distributions, while general distributions are solved by numerical methods. Montagnino described a numerical method which is applicable to any kinds of gradients in 1968 [39]. In 1982, Sharma developed an improved method, which reduces the computation effort [45]. The new method is based on an alternative description of the ray equation, which can now be solved with a standard numerical method for ordinary differential equations. The method developed by Sharma depends on a variable τ describing the ray propagation through the media and does not directly depend on the variables x, y, z making it difficult to follow a ray to a certain point or plane in space. Brenner showed in his lecture ‘Computational optics’ [3] that the ray equation can also be parametrized in z instead of τ. He also further expanded the method to obtain the optical path length with the same iteration method.

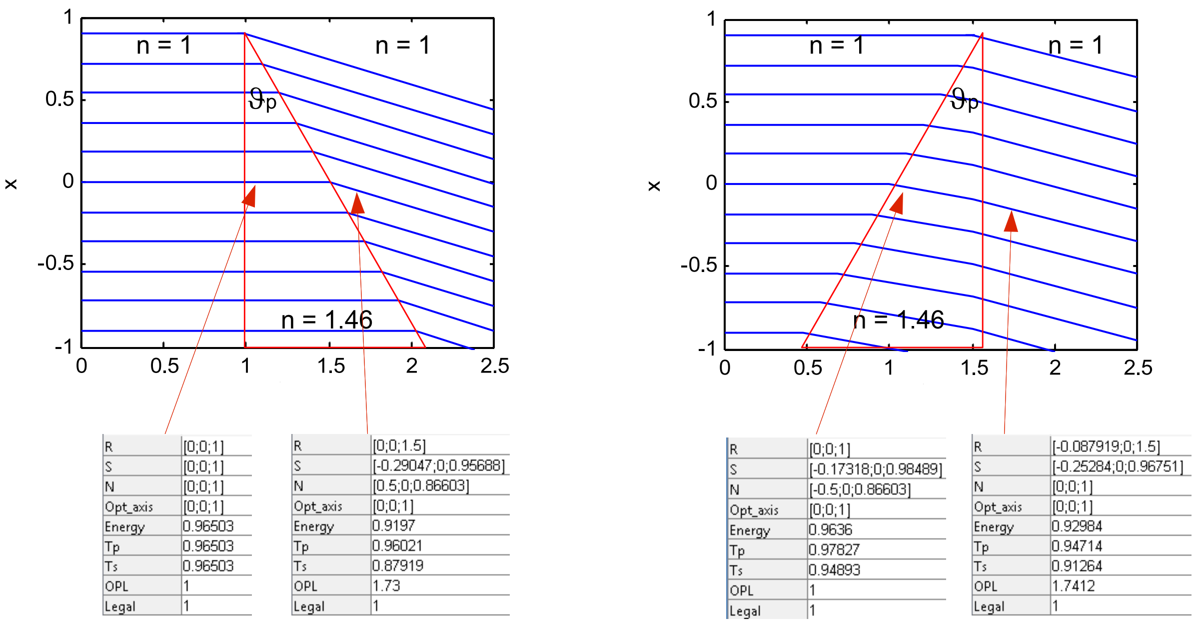

R	[0;0;1]
S	[0;0;1]
N	[0;0;1]
Opt_axis	[0;0;1]
Energy	0.96503
Tp	0.96503
Ts	0.96503
OPL	1
Legal	1

R	[0;0;1.5]
S	[-0.29047;0;0.95688]
N	[0.5;0;0.86603]
Opt_axis	[0;0;1]
Energy	0.9197
Tp	0.96021
Ts	0.87919
OPL	1.73
Legal	1

R	[0;0;1]
S	[-0.17318;0;0.98489]
N	[-0.5;0;0.86603]
Opt_axis	[0;0;1]
Energy	0.9636
Tp	0.97827
Ts	0.94893
OPL	1
Legal	1

R	[-0.087919;0;1.5]
S	[-0.25284;0;0.96751]
N	[0;0;1]
Opt_axis	[0;0;1]
Energy	0.92984
Tp	0.94714
Ts	0.91264
OPL	1.7412
Legal	1

Figure 4.20: Ray trace through two 30° prisms with the transmitted energy for p and s-polarization T_p and T_s, and for unpolarized light: $Energy = \frac{1}{2}\left(T_s + T_p\right)$.

The following paragraphs will describe the ray equation, the adaption to the Runge-Kutta methods, and the parametrization in z instead of τ. Finally, the method from Sharma and Brenner are compared in terms of accuracy using an equal number of iteration steps for different gradient index media.

4.4.1 The Ray Equation

In inhomogeneous media, the refraction index n depends on the location $\vec{r}$.

$$n = n\left(\vec{r}\right) \tag{4.39}$$

The optical path length L is given by

$$L = \int n\, ds \tag{4.40}$$

with $ds = d\left|\vec{r}\right|$. Expansion by $ds = dt \cdot ds/dt$ and $ds/dt = v$ leads to

$$L = \int n \cdot v\, dt. \tag{4.41}$$

Fermat's principle of least time demands: $L \rightarrow min$. This leads to an Euler-Lagrange equation, $F = F(r_j, v_j, t)$, $j = x, y, z$, with the ray equation as solution:

$$\frac{d}{ds}\left(n\,\frac{d\vec{r}}{ds}\right) = \vec{\nabla} n. \tag{4.42}$$

The substitution of

$$ds = n \cdot d\tau \tag{4.43}$$

changes the ray equation into

$$\frac{d^2\vec{r}}{d\tau^2} = n \cdot \vec{\nabla} n, \tag{4.44}$$

a second order differential equation.

4.4.2 The Runge-Kutta method

Around 1900, C. Runge and M.W. Kutta developed an important family of iterative methods for the approximation of ordinary differential equations, called the Runge-Kutta methods. They are described at length by Butcher [7] and approximate equations of the kind

$$\frac{d\vec{y}}{dx} = \vec{f}\,(x, \vec{y}) \tag{4.45}$$

in their fourth order (RK4) with the step length h by

$$\begin{aligned}
\vec{k}_1 &= h \cdot \vec{f}\,(x_n, \vec{y}_n)) \\
\vec{k}_2 &= h \cdot \vec{f}\left(x_n + \frac{h}{2}, \vec{y}_n + \frac{\vec{k}_1}{2})\right) \\
\vec{k}_3 &= h \cdot \vec{f}\left(x_n + \frac{h}{2}, \vec{y}_n + \frac{\vec{k}_2}{2})\right) \\
\vec{k}_4 &= h \cdot \vec{f}\,(x_n + h, \vec{y}_n + k_3) \\
\vec{y}_{n+1} &= \vec{y}_n + \frac{1}{6}\left(\vec{k}_1 + 2\vec{k}_2 + 2\vec{k}_3 + \vec{k}_4\right).
\end{aligned} \tag{4.46}$$

4.4.3 Adaption for the ray equation

The ray equation is an ordinary differential equation of second order while the Runge-Kutta method solves equations of first order. An adaption of RK4 solves this problem by stacking $\vec{y}\,'$ and $\vec{y}\,''$

$$\begin{pmatrix} y' \\ \\ y'' \end{pmatrix} = \begin{pmatrix} f\,(x, y) \\ \\ f\,(x, y') \end{pmatrix}. \tag{4.47}$$

For the ray equation, y' corresponds to $\frac{d\vec{r}}{d\tau}$ which is derived by the following considerations:

$$\begin{aligned}
\vec{v} &= \frac{d\vec{r}}{dt} = \frac{d\vec{r}}{ds} \cdot \frac{ds}{dt} = v \cdot \frac{d\vec{r}}{ds} \\
\frac{d\vec{r}}{ds} &= \frac{\vec{v}}{v} = \vec{s} \qquad (4.48) \\
\frac{d\vec{r}}{d\tau} &= \frac{d\vec{r}}{ds} \cdot \frac{ds}{d\tau} = \frac{d\vec{r}}{ds} \cdot n \\
\frac{d\vec{r}}{d\tau} &= n \cdot \vec{s} \\
\frac{d\vec{r}}{d\tau} &= \vec{t}. \qquad (4.49)
\end{aligned}$$

$\vec{s}$ is the direction vector of the ray and $\vec{t} = \vec{s} \cdot n$; both are known for the initial ray.

4.4.4 Optical path length

The optical path length L of rays in inhomogeneous media can also be derived by an ordinary differential equation which is again solved by RK4:

$$L = \int n \, ds$$

with the definition of $d\tau = \frac{ds}{n}$ (formula 4.43), the equation becomes

$$L = \int n^2 \, d\tau$$

or

$$\frac{dL}{d\tau} = n^2. \qquad (4.50)$$

4.4.5 Propagation steps

Since the RK4 method depends on $d\tau$, the propagation to a fixed plane at a certain z requires additional effort. A description with step length dz rather than $d\tau$ is desirable. Brenner [3] described a new parametrization in z instead of τ, which is briefly repeated here.

With the transposition of the equation 4.49, regarding only the z-component of $\vec{r}$

$$\begin{aligned}
\frac{d\vec{r}}{d\tau} &= \vec{t} \\
\frac{dr_z}{d\tau} &= t_z \qquad (4.51)
\end{aligned}$$

and $d\tau = \frac{d\tau}{dr_z} \cdot dr_z$ with $\frac{d\tau}{dr_z} = \frac{1}{t_z}$ one obtains

$$d\tau = \frac{1}{t_z} dr_z. \tag{4.52}$$

This transformation allows to propagate all rays exactly to the same z-plane without additional effort. But there is also one disadvantage. While the step size along one ray path is constant using $d\tau$, the step size with dz is not, getting longer with increasing propagation angles, which might reduce the accuracy. This will be discussed in the comparison with Sharma's method.

4.4.6 Computational scheme

The start vector $\vec{Y_0}$ is given by the start position of the ray $\vec{r_0}$ and the vector $\vec{t_0}$ which is calculated by multiplying $\vec{s}_0$ by $n(\vec{r_0})$.

$$\vec{Y_0} = \begin{pmatrix} \vec{r_0} \\ \vec{t_0} \\ L \end{pmatrix}. \tag{4.53}$$

The iteration is then

$$\vec{Y}_{n+1} = \begin{pmatrix} \vec{r}_{n+1} \\ \vec{t}_{n+1} \\ L \end{pmatrix} = RK4 \left[d\tau, \begin{pmatrix} Y_{\vec{r}_n}/d\tau \\ Y_{\vec{t}_n}/d\tau \\ Y_L/d\tau \end{pmatrix} \right] = RK4 \left[d\tau, \begin{pmatrix} Y_{\vec{t}_n} \\ n\vec{\nabla} n \\ n^2 \end{pmatrix} \right] \tag{4.54}$$

and with the parametrization in dz instead of $d\tau$ since $d\tau = dz/tz$

$$\vec{Y}_{n+1} = \begin{pmatrix} \vec{r}_{n+1} \\ \vec{t}_{n+1} \\ L \end{pmatrix} = RK4 \left[dz, \begin{pmatrix} Y_{\vec{t}_n} \\ n\vec{\nabla} n \\ n^2 \end{pmatrix} \cdot \frac{1}{t_{nz}} \right]. \tag{4.55}$$

Example: Luneburg lens The Luneburg lens is a spherical symmetric structure with a refraction index distribution of:

$$n\left(\vec{r}\right) = \sqrt{2 - \left(\frac{\vec{r}}{R}\right)^2} \tag{4.56}$$

It focuses every incoming ray, parallel to the optical axis, on its back surface. In the following, a two dimensional Luneburg lens will be traced by the adapted RK4 method, derived from the previous sections. The start vector is

$$Y_0 = (x_0\,, \quad z_0\,, \quad tx_0 = 0\,, \quad tz_0 = 1\,, \quad L_0 = 0) \tag{4.57}$$

and the iteration vector in z parametrization for the adapted RK4 method is

$$\begin{pmatrix} y'_{xi} \\ y'_{zi} \\ y''_{xi} \\ y''_{zi} \\ L \end{pmatrix} = RK4 \left[dz, \begin{pmatrix} t_{xi} \\ t_{zi} \\ \left[\left(n\vec{\nabla}n\right)\vec{e}_x\right]_{xi} \\ \left[\left(n\vec{\nabla}n\right)\vec{e}_z\right]_{zi} \\ n^2 \end{pmatrix} \cdot \frac{1}{t_{zi}} \right] . \tag{4.58}$$

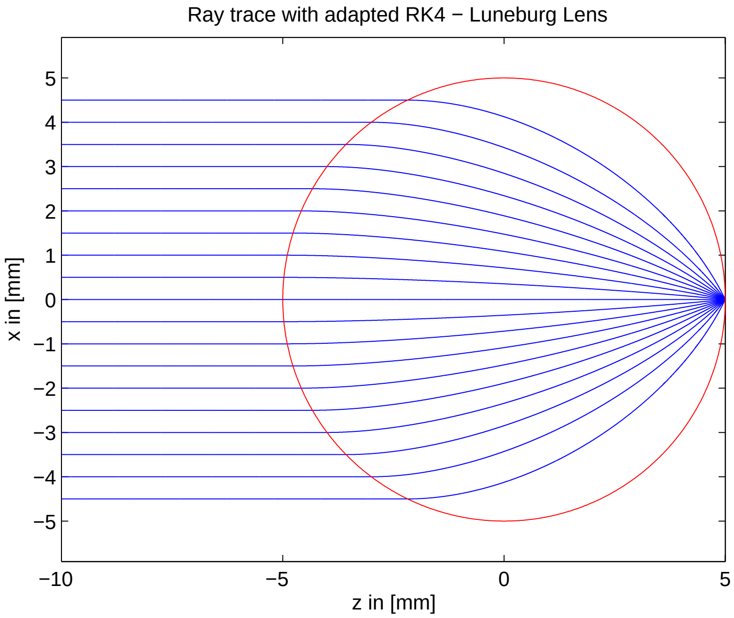

Figure 4.21: Ray trace of a Luneburg lens with the adapted RK4 method

The trace, depicted in figure 4.21, demonstrates the correctness of the adapted method. All parallel rays are focused perfectly onto the back surface at $z = R$.

4.4.7 Comparison between Sharma's and Brenner's method

Sharma compared his method to Montagnino's method in a refractive-index distribution given by

$$n(z) = n_0 - \gamma z \tag{4.59}$$

with $n_0 = 1.55$ and $\gamma = 0.2$. He traced a ray starting at $\vec{r}_0 = \vec{0}$ with a certain angle ϑ in the xz-plane and compared the numerically estimated position with the analytical one at $z = 2$, once for his method and once for Montagnino's method. Since his method is parameterized in τ he had to take the analytically calculated τ_{end} for $z = 2$ as reference position.

For a comparison between Sharma and Brenner, Sharma's refractive index distribution is taken and his method is compared once with Brenner's τ parametrization to qualify the numerical accuracy and once with the z parametrization. In order to compare the methods on exact the same position, τ_{ref} is calculated from the analytical solution. This comparison is repeated for a second index distribution, the Luneburg lens.

The analytical solutions are given in the next paragraphs, followed by the comparison between the methods of Sharma and Brenner for different numbers of steps.

4.4.7.1 Analytical solution for $n(z) = n_0 - \gamma z$

Considering a ray starting at $\vec{r}_0 = \vec{0}$ under a certain angle ϑ in the xz-plane, the differential equation of second order is once solved for the x-component and once for the z-component. The solution is parametrized in τ

$$\vec{r}(\tau) = \begin{pmatrix} n_0 \sin(\vartheta) \cdot \tau \\ 0 \\ C_1 \cdot e^{\gamma\tau} + C_2 \cdot e^{-\gamma\tau} + C_3 \end{pmatrix} \tag{4.60}$$

with the parameters C_1, C_2 and C_3

$$C_1 = \frac{n_0}{\gamma}(\cos\vartheta - 1) \tag{4.61}$$

$$C_2 = -\frac{n_0}{\gamma}(\cos\vartheta + 1) \tag{4.62}$$

$$C_3 = \frac{n_0}{\gamma}. \tag{4.63}$$

In the following comparison, the ϑ of Sharma is used, $\vartheta = 17°27'$. For the given parameters, the analytical solution delivers:

$$\vec{r}\,(\tau_{end}) = \begin{pmatrix} 0.740920295008490 \\ \\ 0 \\ \\ 2 \end{pmatrix} \tag{4.64}$$

with $\tau_{end} = 1.594049613977570$.

4.4.7.2 Analytical solution for the Luneburg lens

The Luneburg lens distribution focuses incoming parallel light onto the back surface of the sphere with radius R_L (see figure 4.21). The analytical solution for a ray in the xz-plane, starting parallel to the z-axis, is given by

$$\vec{r}(\tau) = \begin{pmatrix} x_0 \cdot \cos\left(\frac{\tau}{R_L}\right) \\ \\ 0 \\ \\ R_L \cdot \sin\left(\frac{\tau}{R_L}\right) - \sqrt{R_L^2 - x_0^2} \cdot \cos\left(\frac{\tau}{R_L}\right) \end{pmatrix}. \tag{4.65}$$

Considering a Luneburg lens positioned at the origin with radius $R_L = 5$ and incoming parallel light to the optical axis z, the ray's x-position at $z = 5$ has to be $x = 0$.

4.4.7.3 Comparison

The methods are compared for two refractive index distributions: Montagnino's and Sharma's distribution from formula 4.59 described in the previous paragraph and once for the Luneburg lens. Each comparison shows both methods with τ parametrization in order to compare the position accuracy, but also once for Brenner's z-parametrization in order to show the advantages and disadvantages of the new parametrization. The position error is calculated as

$$Pos_{error} = \sqrt{\left(x_{num} - x_{ref}\right)^2 + \left(z_{num} - z_{ref}\right)^2}. \tag{4.66}$$

All comparisons are based on the achieved position accuracy in relation to the number of iteration steps for each method.

Sharma's refractive index distribution Figure 4.22 depicts the ray path through the inhomogenous media with $n(z) = 1.55 - 0.2z$ and figure 4.23 shows the position accuracy

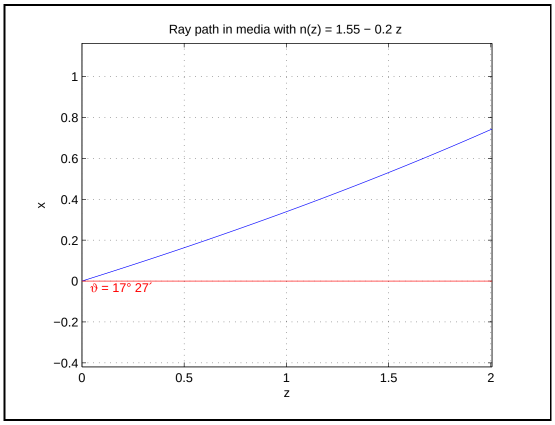

Figure 4.22: Ray path of a ray starting with $\vartheta = 17°27'$ with the z-axis at $z = 0$ in the media $n(z) = 1.55 - 0.2z$

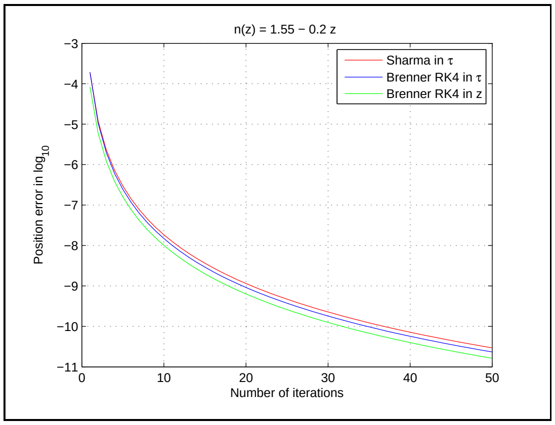

Figure 4.23: Parametrization in z and τ: position error at $z = 2$ of a ray launched at an angle of $\vartheta = 17°27'$ with the z-axis at $z = 0$ as a function of the number of iterations.

of both methods with τ parametrization and also once for Brenner's RK4 method with z-parametrization.

The comparison shows that Brenner's RK4 method with both parametrizations is slightly in the lead in terms of position accuracy for the regarded media.

Luneburg lens The reference ray starts on the surface of the Luneburg sphere with $\vec{r}_0 = \left(x_0,\ z_0 = -\sqrt{R_L^2 - x_0^2}\right)$ for $x_0 = 2$ and for $x_0 = 4.5$ to compare paraxial and nonparaxial behavior of the methods. Figure 4.24 depicts the position accuracy for $x_0 = 2$ and figure 4.25 for $x_0 = 4.5$.

While Brenner's RK4 method performed better in Sharma's media, Sharma's method is slightly better for the Luneburg lens considering only the τ parametrization. The z-parametrization of Brenner's RK4 performs better for paraxial rays, but worse for non-paraxial rays. The reason lies within the different step sizes. While the step size in a τ parametrization is constant along the ray path, the step size in z-parametrization is not, making larger steps with increasing ray angle to the z-axis. The small dip of Brenner's RK4 method with z-parametrization at iteration step 7 for $x_0 = 2$ marks a sign change of the computed x-position.

Summary Two methods for ray tracing in inhomogeneous media are compared: Sharma's method and Brenner's RK4 method. Both methods use an adapted form of the ray equation which allows a numerical solution using the Runge-Kutta method. In the standard parametrization in τ, both methods perform equally in terms of position accuracy and computational effort. The important advantage of Brenner's method comes with the new parametrization in z, which allows accurate ray tracing to defined positions in space. Care

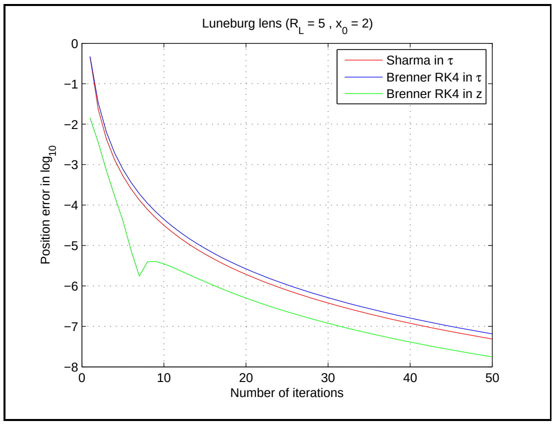

Figure 4.24: Paraxial position error at the back surface of the Luneburg lens sphere at $z = 5$. The considered ray starts on the sphere with $x_0 = 2$ and $z_0 = -\sqrt{R_L^2 - x_0^2}$ parallel to the z-axis.

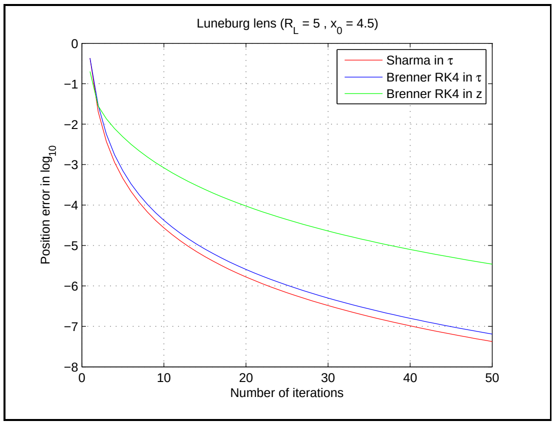

Figure 4.25: Non paraxial position error at the back surface of the Luneburg lens sphere at $z = 5$. The considered ray starts on the sphere with $x_0 = 4.5$ and $z_0 = -\sqrt{R_L^2 - x_0^2}$ parallel to the z-axis.

has to be taken with the z-parametrization in media where rays reach high propagation angles to the z-axis, because the step size is not constant with the ray path but with z.

4.5 Conclusion

Different aspects of a customized ray tracer were described in this chapter. The deterministic generation of rays with point and area sources was simulated and compared with the corresponding analytical solution. For reasonable ray counts, far below the needed rays of Monte-Carlo-Simulations, the error is within ±2%. The intersection and the reflection of rays on the inner side of two customized surfaces, the slanted cylinder and the ellipsoid, were derived analytically. A characteristic of the customized ray tracer is the correct calculation of the energy transfer on each boundary according to the Fresnel coefficients. The propagation of rays in inhomogeneous media is described by the ray equation that was numerically solved with an adapted Runge-Kutta algorithm and illustrated with the Luneburg lens as an example. Sharma described this method for a parametrization in τ while Brenner showed that the method can also be parametrized in z. A comparison shows that both methods perform equally in position accuracy considering the τ-parametrization. The important advantage of Brenner's method comes with the z-parametrization which allows accurate ray tracing to defined positions in space with the cost of a possible loss of accuracy due to the non-constant step length along the ray path.

Chapter 5

Scalar wave optics

Wave optics are based on the Maxwell equations and describe the vast majority of optical phenomena. In homogeneous dielectric media the wave equation

$$\Delta \vec{E} + \frac{\mu\epsilon}{c^2} \ddot{\vec{E}} = 0 \tag{5.1}$$

with the monochromatic plane wave as solution

$$\vec{E}\left(\vec{r}, t\right) = \vec{E}_0 \cdot e^{i\vec{k}\vec{r} - \omega t} \tag{5.2}$$

and

$$k = \frac{2\pi}{\lambda} \tag{5.3}$$

is used to derive a formula for the propagation of light:

$$\vec{E}\left(\vec{r}, t\right) = \vec{E}_0 \cdot e^{i(k_x \cdot x + k_y \cdot y + k_z \cdot z - \omega t)}. \tag{5.4}$$

Neglecting the temporal and vectorial character of light, acceptable in homogeneous media for small boundary condition areas in respect to the area the wave is passing (Goodman [23]), one obtains:

$$u\left(\vec{r}_\perp, z\right) = u_0 \cdot e^{i\left(\vec{k}_\perp \vec{r}_\perp\right)} e^{iz\sqrt{\left(\frac{n\omega}{c}\right)^2 - \vec{k}_\perp^2}} \tag{5.5}$$

and with $u\left(r_\perp, 0\right) = u_0 \cdot e^{i\left(\vec{k}_\perp \vec{r}_\perp\right)}$

$$u\left(\vec{r}_\perp, z\right) = u\left(\vec{r}_\perp, 0\right) e^{iz\sqrt{\left(\frac{n\omega}{c}\right)^2 - \vec{k}_\perp^2}}. \tag{5.6}$$

This equation describes the propagation of a monochromatic plane wave in z direction.

In the following sections, scalar propagation methods based on the principle of plane wave decomposition will be presented: Rayleigh & Sommerfeld, Fresnel, and Fresnel in a secondary representation, here called QFQ method. For each method, a formula for the maximum or minimum propagation length $z_{max,min}$ will be derived, and the transition from near to far field analyzed. The final section deals with light propagation in inhomogeneous media simulated by the beam propagation method and wave propagation method and their restrictions.

5.1 Scalar propagation methods

By the principle of plane wave decomposition, any given light field distribution can be regarded as a superposition of plane waves. The propagation of light from $z_0 = 0$ to z is then given by the decomposition of the light distribution u at $z_0 = 0$, the propagation of each planar wave according to formula 5.6, and the superposition of all plane wave at distance z.

5.1.1 Rayleigh and Sommerfeld diffraction integral

Without approximations one obtains the Rayleigh and Sommerfeld integral

$$u\left(\vec{r}_\perp, z\right) = \iint \tilde{u}\left(\vec{k}_\perp, 0\right) \cdot e^{iz\sqrt{\left(\frac{n\omega}{c}\right)^2 - \left(\vec{k}_\perp\right)^2}} \cdot e^{i\left(\vec{k}_\perp \vec{r}_\perp\right)} \, \frac{d^2 k_\perp}{\left(2\pi\right)^2} \tag{5.7}$$

with $k_\perp^2 = \left(k_x^2 + k_y^2\right)$ and $\tilde{u} = \mathcal{F}\left(u\right)$, $\mathcal{F}$ symbolizes the Fourier transform. The variables $k_{x,y}$ are alternatively expressed by the frequency components $\nu_{x,y}$ via the equation $k_{x,y} = 2\pi\nu_{x,y}$. The method is also called plane wave spectrum, short PWS. The propagation multiplier

$$P_{PWS} = e^{iz\sqrt{\left(\frac{n\omega}{c}\right)^2 - \left(\vec{k}_\perp\right)^2}} \tag{5.8}$$

is called the propagator of the PWS method.

5.1.2 Fresnel diffraction integral

The Fresnel method is an approximation of the PWS method. The Fresnel propagator P_F is obtained by the following approximation of the PWS propagator:

$$\begin{aligned} P &= e^{i\,z\,\sqrt{\left(n\,k_0\right)^2 - k_\perp^2}} \\ &= e^{i\,z\,n\,k_0\sqrt{1 - \frac{k_\perp^2}{\left(n\,k_0\right)^2}}} \\ &\approx e^{i\,z\,n\,k_0\left(1 - \frac{k_\perp^2}{2\left(n\,k_0\right)^2}\right)} \\ P_F &= e^{i\,z\,n\,k_0}\, e^{-i\,z\,\frac{k_\perp^2}{2n\,k_0}}. \end{aligned} \tag{5.9}$$

The square root approximation $\sqrt{1+\epsilon} \approx 1 + \frac{\epsilon}{2}$ is valid if $\frac{\vec{k}_\perp}{n\,k_0} << 1$. With the Fresnel propagator the propagation integral becomes:

$$u\left(\vec{r}_\perp, z\right) = e^{i\,z\,n\,k_0} \iint \tilde{u}\left(\vec{k}_\perp, 0\right) \cdot e^{-iz\frac{k_\perp^2}{2n\,k_0}} \cdot e^{i\left(\vec{k}_\perp \vec{r}_\perp\right)} \, \frac{d^2 k_\perp}{\left(2\pi\right)^2}. \tag{5.10}$$

This equation is known as the Fresnel diffraction integral.

5.1.3 QFQ - Fresnel transformation

Equation 5.10 is an inverse Fourier transform of a product. This corresponds to a convolution integral

$$u\left(\vec{r}_{\perp}, z\right) = \iint u\left(\vec{r}'_{\perp}, 0\right) G_F\left(\vec{r}_{\perp} - \vec{r}'_{\perp}, z\right)\, d^2 r'_{\perp} \tag{5.11}$$

with

$$G_F\left(\vec{r}_{\perp}, z\right) = e^{i\, z\, n\, k_0} \iint e^{-i\pi\, z\, \lambda\, \nu_{\perp}^2} \cdot e^{2\pi i\, \vec{\nu}_{\perp}\, \vec{r}_{\perp}}\, d^2\nu. \tag{5.12}$$

G_F represents a Fourier integral of a square phase which can be analytically derived and one obtains the Fresnel integral in position space.

$$u\left(\vec{r}_{\perp}, z\right) = \frac{-i}{\lambda\, z} \cdot e^{i\, n\, k_0\, z} \iint u\left(\vec{r}_{\perp}{}', 0\right)\, e^{i\pi \frac{1}{\lambda\, z}\left(\vec{r}_{\perp} - \vec{r}_{\perp}{}'\right)^2} d^2\vec{r}_{\perp}{}'. \tag{5.13}$$

When excluding one square phase factor the integral becomes:

$$u\left(\vec{r}_{\perp}, z\right) = \frac{-i}{\lambda\, z} \cdot e^{i\, n\, k_0\, z} \cdot e^{i\pi \frac{r_{\perp}^2}{\lambda z}} \cdot \iint u\left(\vec{r}_{\perp}{}', 0\right) \cdot e^{i\pi \frac{{r'_{\perp}}^2}{\lambda z}} \cdot e^{-2\pi i \frac{1}{\lambda z} \vec{r}_{\perp} \vec{r}_{\perp}{}'} d^2\vec{r}_{\perp}{}'. \tag{5.14}$$

Care has to be taken after the first Fourier transformation with $\vec{\nu}_{\perp} = \frac{\vec{r}_{\perp}}{\lambda z}$ because the axis is now scaled with λz.

This propagation method will be referred to as the QFQ method, which stands for: product with a square phase, Fourier transformation, and a second product with a square phase. The QFQ method is named after the German word for 'square' which is 'Quadrat'.

5.2 Numerical restrictions of the scalar propagation

During discretization of $u\left(x, y\right)$ one has to chose a suitable dx and a suitable dy, which are in the following equalized $dx = dy$. The selection of dx also defines the discretization in the Fourier space $d\nu$

$$d\nu = \frac{1}{N\, dx} \tag{5.15}$$

with N being the sampling number. Due to the anti proportional relation between dx and $d\nu$, a finer sampling in the spatial domain causes a rougher sampling in the frequency domain. The only way to increase the resolution in the frequency domain is by increasing N considering the same field size W.

5.2.1 Evanescent limit

The PWS propagator term

$$P_{PWS} = e^{iz\sqrt{\left(\frac{n\omega}{c}\right)^2 - \left(\vec{k}_{\perp}\right)^2}} \tag{5.16}$$

from equation 5.8 determines the evanescent limit

$$\begin{aligned}\left(\frac{n\omega}{c}\right)^2 &\geq \left(\vec{k}_\perp\right)^2 \\ \left(\frac{n}{\lambda_0}\right)^2 &\geq \left(\nu^2+\mu^2\right) \\ \frac{1}{\lambda^2} &\geq R_\nu^2 \\ \Rightarrow R_{\nu_{max}} &= \frac{1}{\lambda} \qquad (5.17)\end{aligned}$$

with the wavelength λ in the media. The frequency radius $R_{\nu_{max}}$ corresponds to waves propagating with wavelength λ at 90° in the spatial domain.

5.2.2 Maximum propagation length

The PWS propagator is an oscillating function with increasing frequency for higher νs. It is depicted for two different propagation lengths z in the figures 5.1 and 5.2.

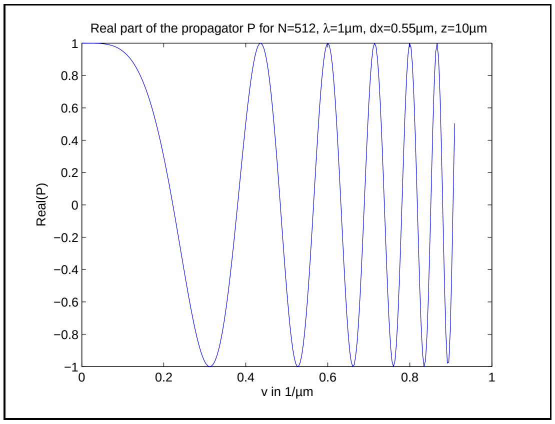

Figure 5.1: Real part of the propagator for $z = 10\,\mu$m

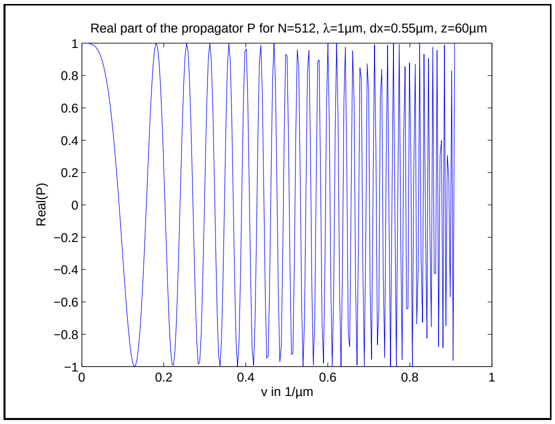

Figure 5.2: Real part of the propagator for $z = 60\,\mu$m

According to the Nyquist theorem, the sampling frequency has to be higher or equal than twice the highest frequency of the sampled function

$$f_{sample} \geq 2 \cdot f_{max}. \qquad (5.18)$$

As the sampling frequency is fixed at $d\nu$, z is limited to a certain z_{max}. Higher z_{max} will cause sampling errors in the outer frequency regions.

A condition for the highest or lowest propagation length z without sampling errors will be derived in the following for the PWS propagator P_{PWS}, the Fresnel propagator P_F, and the QFQ propagator P_{QFQ}.

5.2.2.1 z_{max} of the PWS propagator

The local frequency of a function is defined as

$$f = \frac{1}{2\pi}\frac{d\phi}{dq} \tag{5.19}$$

with the angular function ϕ and the variable q. The angular function of the PWS propagator is

$$\begin{aligned} \phi &= z\sqrt{\left(nk_0\right)^2 - k_\perp^2} \\ \phi\left(q\right) &= z\sqrt{\left(nk_0\right)^2 - \left(2\pi q\right)^2} \end{aligned} \tag{5.20}$$

with the derivative

$$\frac{d\phi}{dq} = z\frac{1}{2\sqrt{\left(nk_0\right)^2 - \left(2\pi q\right)^2}} \cdot \left(-8\pi^2 q\right). \tag{5.21}$$

Insertion into equation 5.19 delivers

$$\begin{aligned} f &= \frac{1}{2\pi}z\frac{1}{2\sqrt{\left(nk_0\right)^2 - \left(2\pi q\right)^2}} \cdot \left(-8\pi^2 q\right) \\ f &= -2\pi q z \cdot \frac{1}{\sqrt{\left(nk_0\right)^2 - \left(2\pi q\right)^2}}. \end{aligned} \tag{5.22}$$

The local period is defined as

$$P_{loc} = \frac{1}{|f|} \tag{5.23}$$

and becomes by inserting equation 5.22

$$P_{loc} = \frac{\sqrt{\left(nk_0\right)^2 - \left(2\pi q\right)^2}}{2\pi q z}. \tag{5.24}$$

The sampling theorem gives a condition for P_{loc}: $P_{loc} \geqslant 2dq$

$$\begin{aligned} 2dq &\leqslant \frac{\sqrt{\left(nk_0\right)^2 - \left(2\pi q\right)^2}}{2\pi q z} \\ z &\leqslant \frac{\sqrt{\left(nk_0\right)^2 - \left(2\pi q\right)^2}}{4\pi\, q\, dq}. \end{aligned} \tag{5.25}$$

With insertion of

$$nk_0 = \frac{2\pi}{\lambda}, \quad dq = \frac{1}{Ndx}, \quad q = \nu_{\max} = \frac{N}{2}dq = \frac{1}{2dx} \tag{5.26}$$

the condition for z_{max} is derived as

$$\begin{aligned} z &\leqslant \frac{\sqrt{(nk_0)^2 - \left(\frac{2\pi}{2dx}\right)^2}}{4\pi\, q\, dq} \\ z &\leqslant \frac{2N\, dx^2}{4\pi}\sqrt{\frac{4\pi^2}{\lambda^2} - \frac{4\pi^2}{4dx^2}} \\ z &\leqslant \frac{N\, dx^2}{\lambda}\sqrt{1 - \left(\frac{\lambda}{2dx}\right)^2}. \end{aligned} \tag{5.27}$$

With the computational field width $W = N\, dx$ equation 5.27 can be presented in another form:

$$\frac{z}{W} \leqslant \frac{dx}{\lambda}\sqrt{1 - \left(\frac{\lambda}{2dx}\right)^2} \tag{5.28}$$

$$\frac{z}{W} \approx \frac{dx}{\lambda} \text{ (for } \lambda << 2dx) \tag{5.29}$$

The rough approximation of formula 5.29 can be used as a rule of thumb to determine an estimation of z_{max} in relation to W; example: if $dx = 2\lambda$, $z_{max} = 2W$.

For figure 5.2, the maximal propagation length can now be calculated: $z_{max} = 64.5\,\mu$m.

5.2.2.2 Alternative derivation of z_{max}

Another interpretation of the sampling approach can be derived in the position space. The maximum propagation length is defined as the distance z, in which a plane wave, starting in the origin of the computational field, under the maximum propagation angle given by the sampling in the frequency space ν_{max}, hits the border of the field (figure 5.3).

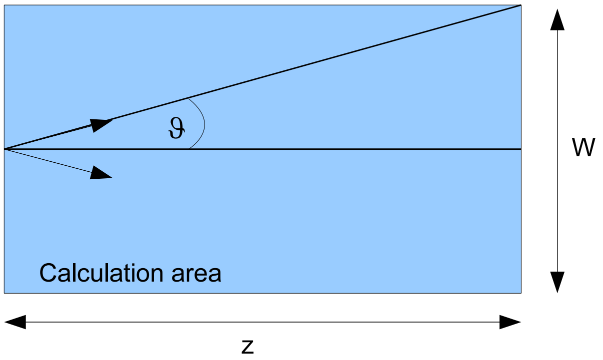

Figure 5.3: Computation area with a ray starting in the origin on the left side going under ϑ to the screen on the right side

The maximum propagation angle of a plane wave λ_0 is given by the minimum sampling in the position space λ_p which is $2dx$

$$\begin{aligned} \vartheta &= \arcsin\left(\frac{\lambda_0}{\lambda_p}\right) \\ &= \arcsin\left(\lambda_0 \cdot \nu_{\max}\right) \\ &= \arcsin\left(\lambda_0 \cdot \frac{1}{2\,dx}\right). \end{aligned} \tag{5.30}$$

The plane wave hits the border of the computational field $W/2$ if

$$z = \frac{W}{2\,\tan\vartheta}. \tag{5.31}$$

Insertion of formula 5.30 into equation 5.31 with

$$\tan\left(\arcsin\left(x\right)\right) = \frac{x}{\sqrt{1-x^2}} \tag{5.32}$$

delivers the same formula as the one derived for the PWS with the sampling approach (see 5.27)

$$\begin{aligned} z &= \frac{W}{2\,\tan\left(\arcsin\left(\frac{\lambda_0}{2\,dx}\right)\right)} \\ &= \frac{N\,dx}{2} \cdot \frac{\sqrt{1-\left(\frac{\lambda_0}{2\,dx}\right)^2}}{\left(\frac{\lambda_0}{2\,dx}\right)} \\ &= \frac{N\,dx^2}{\lambda_0} \cdot \sqrt{1-\left(\frac{\lambda_0}{2\,dx}\right)^2}. \end{aligned} \tag{5.33}$$

5.2.2.3 z_{max} of the Fresnel propagator

A repetition of the considerations for z_{max} for the PWS propagator delivers for the Fresnel propagator:

$$\begin{aligned} \phi\left(q\right) &= -z\,\lambda\,\pi\,q^2 \\ \frac{d\phi}{dq} &= -2z\,\lambda\,\pi\,q \\ f &= -z\,\lambda\;q \\ P_{loc} &= \frac{1}{z\,\lambda\;q} \\ 2dq &\leqslant \frac{1}{z\,\lambda\;q} \\ z &\leqslant \frac{N\,dx^2}{\lambda} \\ \frac{z}{W} &\leqslant \frac{dx}{\lambda}. \end{aligned} \tag{5.34}$$

This is the same result as the rough approximation for z_{max} of the PWS propagator in formula 5.29.

5.2.2.4 z_{min} of the QFQ method

The limitation of the QFQ method is inverse to the limitation of the Fresnel propagator: the method is not limited by a z_{max} but by a z_{min}. The limitation comes from the scaling in position space of the QFQ method. The sampling dx_{QFQ} scales with

$$dx_{QFQ} = \frac{\lambda \cdot z}{N \cdot dx}. \tag{5.35}$$

For small z, the sampling dx_{QFQ} becomes smaller than the sampling dx of $u(x,y)$ in the origin plane, thus information in position space are lost. Therefore, the limitation of the QFQ method is given by:

$$\begin{aligned} dx &\leq \frac{\lambda \cdot z}{N \cdot dx} \\ z_{min} &\geq \frac{N \cdot dx^2}{\lambda}. \end{aligned} \tag{5.36}$$

This is the same limit as for the Fresnel propagator, but the direction is inverse (compare with formula 5.34).

5.2.2.5 Comparison of z_{max} for the PWS and the Fresnel method

The analysis of z_{max} shows that $\frac{dx}{\lambda}$ is the determining relation. An increase of the sampling N, while keeping the computational area the same, even decreases the maximum propagation length. The only way to propagate into longer distances without sampling errors is by either decreasing the spatial sampling (increasing dx) or by increasing the computational area W while leaving dx unchanged. Figure 5.4 shows z_{max} in relation to $\frac{dx}{\lambda}$.

The smallest possible dx in the PWS method has to be bigger than $\lambda/2$. This might be confusing but ν_{max} for $dx = \lambda/2$ corresponds to a wave propagating with λ at 90° and therefore has no k_z component anymore.

One has to keep in mind that these limitations of dx and z_{max} are only solid in the worst case scenario, if the function $\tilde{u}\left(\vec{k}_{\perp}, 0\right)$ becomes considerably higher than zero near the evanescent limit. In the majority of cases, energies in the frequencies near the evanescent area are small enough to neglect sampling errors within these regions.

5.3 Propagation errors

The three described propagation methods stand for different physical wave models: the PWS method propagates spherical waves, while the Fresnel and QFQ method propagate

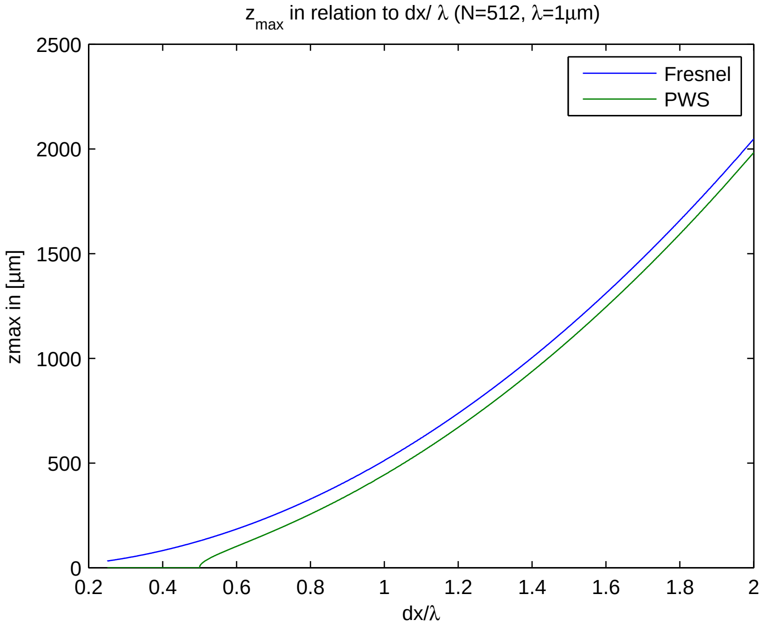

Figure 5.4: Maximum propagation length in relation to dx/λ

parabolic waves. In the far field, the spherical or parabolic waves become plane wave fronts, the field of the Fraunhofer far field approximation, which was not described here. The PWS and Fresnel method depend on the correct sampling of their propagator to avoid additional sampling errors while the QFQ method has no sampling problem with increasing distances.

In order to get an idea of the influence of the sampling error, the first part of this section compares the Fresnel method with an analytical solution of the Gaussian beam based on the Fresnel approximation.

5.3.1 Sampling errors of the Fresnel propagator

The sampling errors depend strongly on the frequency components of the regarded light distribution $u(x, y, z = 0)$. Distributions with only low frequencies will be affected later than those with higher frequency components. To get an idea of the influence, two Gaussian beams with $\sigma_1 = 10\,\mu\text{m}$ and $\sigma_0 = 0.8\,\mu\text{m}$ and both with $\lambda = 500\,\text{nm}$ will be propagated once analytically (Fresnel approximation) and once with the Fresnel propagation method of formula 5.10.

A Gaussian beam in 1D

$$u(x) = e^{-\pi\left(\frac{x}{\sigma_o}\right)^2} \tag{5.37}$$

with its Fourier transform

$$\tilde{u}(\nu) = e^{-\pi\,(\sigma_0\,\nu)^2}$$

is propagated analytically into z direction with the Fresnel approximation

$$\begin{aligned} u\left(x,z\right) &= \int e^{-\pi\left(\sigma_0\,\nu\right)^2}\cdot e^{-i\pi\lambda z\nu^2}\cdot e^{2\pi i\,\nu\,x}\,d\nu \\ &= \int e^{-\pi\,\nu^2\left(\sigma_0^2+i\,\lambda\,z\right)}\cdot e^{2\pi i\,\nu\,x} d\nu \\ &= \int e^{-\pi\,\nu^2 w^2}\cdot e^{2\pi i\,\nu\,x} d\nu \\ &= \frac{1}{w}\,e^{-\pi\left(\frac{x}{w}\right)^2} \end{aligned} \tag{5.38}$$

with $w^2 = \sigma_0^2 + i\,\lambda\,z$.

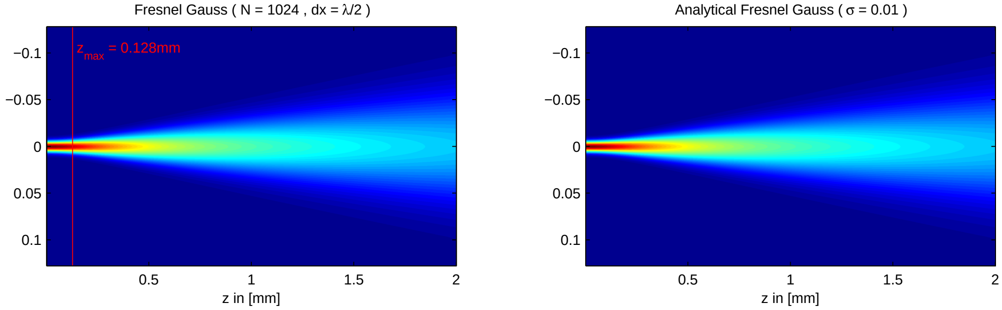

Figure 5.5: Comparison between analytical and the Fresnel propagated Gauss beam (both with Fresnel approximation)

The maximum propagation length is depicted as a vertical line in the left image. The differences between the analytical and Fresnel propagated Gauss beams are in the order of $< 10^{-6}$ even for a large propagation distance $z = 2\,\mathrm{mm}$ ($\approx 10\cdot z_{max}$) (figure 5.5 shows two visually equal Gauss beams).

The reason is the small frequency width of the Gauss beam in Fourier space ($\frac{\nu_{\sigma\,gauss}}{\nu_{max}} \approx 5\%$), where the sampling error has almost no influence.

To see differences, higher frequencies or a smaller σ is needed. The second comparison changes $\sigma_0 = 10\,\mu\mathrm{m}$ to $\sigma_0 = 0.8\,\mu\mathrm{m}$. All other parameters are left unchanged.

The comparison shows that the Fresnel propagation is accurate as long as z_{max} is not exceeded. Due to the periodicity condition of the Fourier transformation, the Gaussian source is repeated in x-direction with the image width as period. If one introduces the same periodicity into the analytical comparison, the errors behind z_{max} vanish. The last Fresnel comparison in figure 5.7 shows the same propagation as the one in the second comparison but with a periodically arranged analytical Fresnel Gauss beam.

5.3.2 Sampling errors of the PWS propagator

The PWS method was derived without approximations for the propagator and should therefore be accurate for the superposition of plane waves. A plane wave propagation is

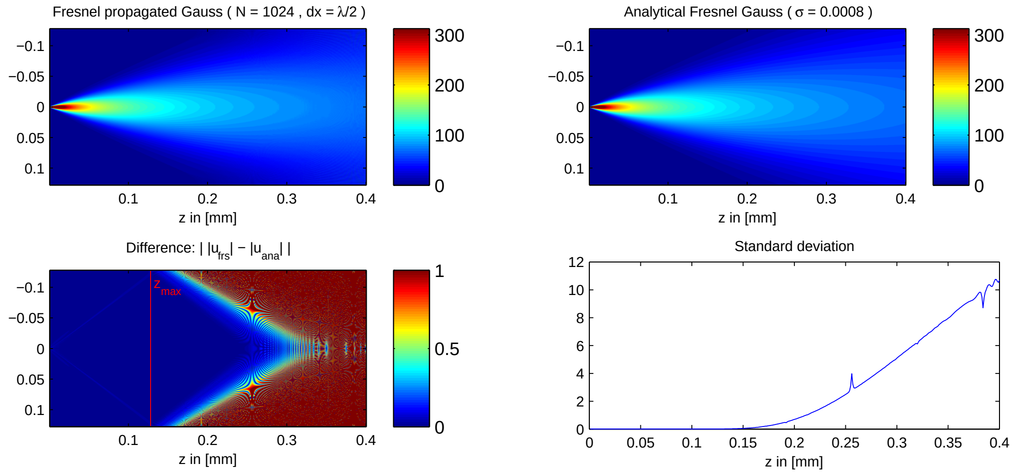

Figure 5.6: Comparison between analytical and Fresnel propagated Gauss $\sigma_0 = 0.8\,\mu$m beam (both with Fresnel approximation)

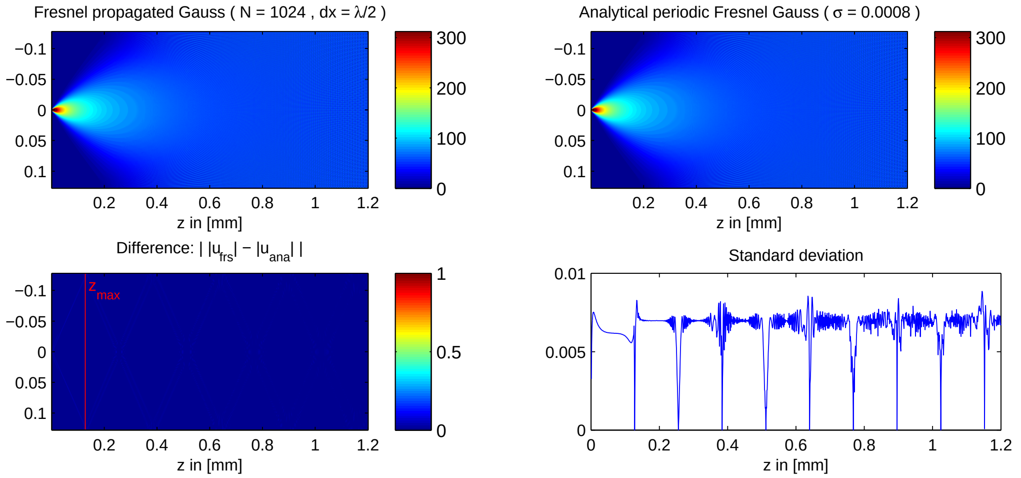

Figure 5.7: Comparison between analytical and Fresnel propagated Gauss $\sigma_0 = 0.8\,\mu$m beam (both with Fresnel approximation). This time, the analytical Gauss is periodically repeated in x-direction and the propagation distance z increased by a factor of 3 to demonstrate the disappearance of the error seen in comparison 5.6

analytically given by

$$u\left(x,y,z\right)=e^{i\left(k_x\cdot x+k_y\cdot y+k_z\cdot z\right)} \tag{5.39}$$

with $\vec{k}=(k_x,k_y,k_z)$. In 1D, the propagation vector $\vec{k}$ becomes

$$\vec{k}=\begin{pmatrix} k_x \\ \\ \sqrt{k_0^2-k_x^2} \end{pmatrix} \tag{5.40}$$

with $k_x=k_0\cdot sin\vartheta$ and the angle of incidence ϑ. Discrete plane waves, plane waves which exactly match a frequency in the Fourier space, are derived with the formula

$$\vartheta=asin\left(\lambda_0\cdot m\cdot d\nu\right) \tag{5.41}$$

with the integer $m=-N/2..N/2-1$.

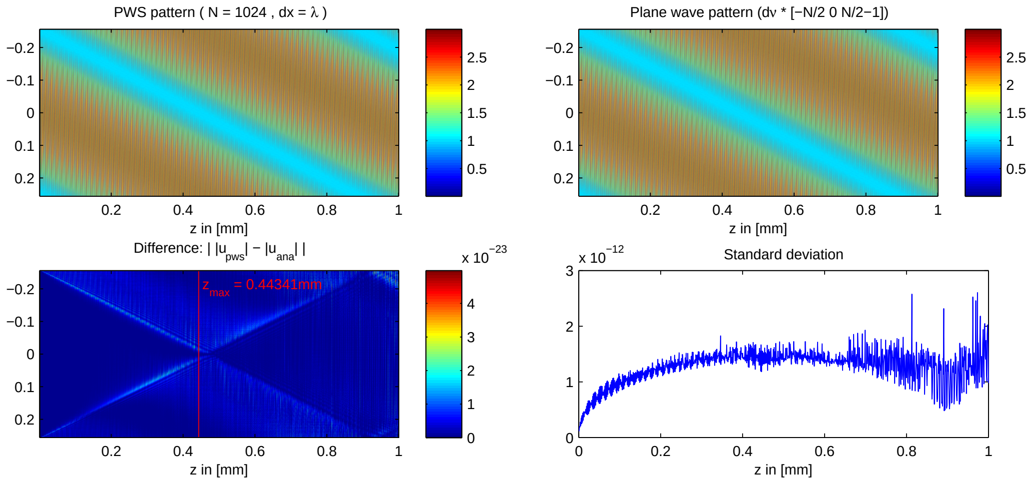

Figure 5.8: Comparison between analytical plane wave expansion and PWS

The comparison in figure 5.8 shows that even for the highest possible angle of incidence, the deviation between analytical and PWS propagated plane waves is within the error of numerical calculations $< 10^{-10}$.

5.3.3 PWS, Fresnel, or QFQ

The question remains, when to choose which propagation method.

As the Fresnel propagator is an approximation of the PWS propagator without any noticeable advantages, one should always choose the PWS propagation within the distance limit z_{max}.

For comparison of the PWS and the Fresnel method with an analytical value, the interference pattern of three plane waves propagating at ±ϑ and 0 is chosen. The plane wave with $+\vartheta$ is shifted by one $d\vartheta$ in order to avoid areas with totally destructive interference. $d\vartheta$ corresponds to a shift of $-d\nu$ in Fourier space. The standard deviation was calculated from the summation of the absolute value over all deviations from the reference value in one z-plane. Since the deviation depends mostly on the propagating distance z and the angle ϑ, a 2D scan over z and ϑ is depicted in figure 5.9.

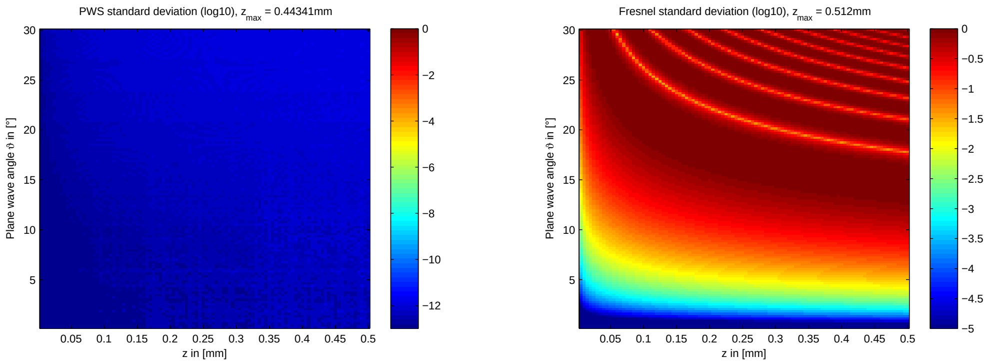

Figure 5.9: Standard deviation in logarithmic scaling of the PWS and the Fresnel method with increasing z and plane wave angles ϑ; the reference is the interference of three plane waves with $-\vartheta$, 0, and $\vartheta - d\vartheta$. Simulation properties: $N = 1024$, $\lambda = 500\,\text{nm}$, $dx = \lambda$ (this determines $\vartheta_{max} = 30°$)

The figure for the Fresnel deviations shows the limitation of the Fresnel propagation for small angles, since it is a paraxial approximation.

For distances of several z_{max}, one has to look at the frequencies of the plane wave decomposition. If the values of the higher frequencies are near zero, the propagation distance can be increased without suffering noteworthy errors. The plane wave with the highest angle and a significant amplitude determines the maximum propagation length according to formula 5.31. If the computed field shows signs of reflections or interference patterns from waves coming from the outside, the maximum propagation length was already considerably exceeded.

For even longer distances, the QFQ method is the best choice: the paraxial approximation is accurate in the far field and due to the scaling of the computation field in position space, plane waves leaving the computation field are not problematical. This behavior is shown in the last comparison of this section with figure 5.10: QFQ propagated Gauss beam and an analytically propagated Gauss beam, both with Fresnel approximation (the Gauss beam is the same as the one in figure 5.6).

The standard deviation for the QFQ method drops with increasing distance z. The minimum distance according to formula 5.36 is $z_{min} = 0.128\,\text{mm}$. The value of the standard deviation is in the order of 10^{-3}, due to the undersampling of the Gaussian beam in the origin plane ($dx = 500\,\text{nm}$ and $\sigma_0 = 800\,\text{nm}$) and not due to the method itself.

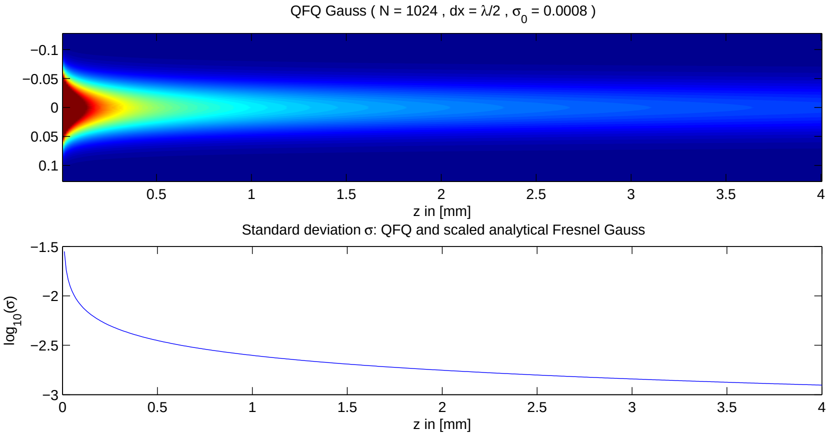

Figure 5.10: Standard deviation in logarithmic scaling of the QFQ and the analytical propagated Fresnel Gauss beam. Simulation properties: $N = 1024$, $\lambda = 500\,\mathrm{nm}$, $dx = \lambda/2$

In summary, the PWS method is the best choice for distances from 0 to z_{max}. For distances of several z_{max}, the sampling of the highest frequency component with a noticeable energy has to be checked for its correctness. If it is sampled correctly, the PWS method can still be used, if not, the QFQ method has to be chosen.

5.4 In inhomogeneous media

In inhomogeneous media, the index of refraction n is a function of space. The scalar propagation methods in the previous sections are based on a constant refractive index. The following section will describe and compare two known methods for the propagation of light in inhomogeneous media: the beam propagation method (BPM) and the wave propagation method (WPM). Both methods divide the volume into small z-slices in which the z-component of the refractive index is constant. The WPM will be further investigated to prevent the energy conservation problem.

5.4.1 BPM

The beam propagation method introduced by Fleck et al. [21] in 1976 is a paraxial numerical solution of the Helmholtz equation (see also Feit and Fleck [19]). It is based on the division of the volume into small z-slices with $n(z) = const.$ In each z-slice, the mean value of $\tilde{n} = (x, y)$ is calculated and the light propagated through the homogeneous z-slice with $\tilde{n}$. The new light distribution is then given by the propagated light through the homogeneous medium, multiplied with a phase correction factor. The BPM is illustrated in table 5.1.

For the propagation through the homogeneous media, the PWS method should be used. The errors introduced by the BPM arise from the averaging of the refractive index in conjunction with the correction phase, where the different propagation angles are omitted.

$\boxed{u\left(x,y,z_j\right)}$	Light field at z_j
$\Downarrow$	
$\boxed{\tilde{n}=\frac{1}{N_xN_y}\sum\limits_{x,y} n\left(x,y,z_j\right)}$	Mean value of $n\left(x,y,z_j\right)$
$\Downarrow$	
$\boxed{u\left(x,y,z_j\right)\xrightarrow[\tilde{n}]{P_{PWS}} u_{\tilde{n}}\left(x,y,z_j+\delta z\right)}$	Propagation in medium with $n=\tilde{n}$ and $z=\delta z$
$\Downarrow$	
$\boxed{u_{\tilde{n}}\left(x,y,z_j+\delta z\right)\cdot e^{i\,\delta z\,\delta n(x,y,z_j)}}$	Correction with phase factor $\left(\delta n=\tilde{n}-n\left(x,y,z_j\right)\right)$
$\Downarrow$	
$\boxed{u\left(x,y,z_j+\delta z\right)}$	Light field at $z_j+\delta z$

Table 5.1: Schematic of one BPM step

5.4.2 WPM

The wave propagation method presented by Brenner and Singer [5] in 1993 is a new numerical method derived from the beam propagation method. It treats every plane wave correctly according to the propagation angle and is therefore accurate for angles up to 85° degrees; the drawback is the higher computational complexity, because the inverse Fast Fourier transform [12] is inapplicable. The schematic for a 1D WPM step is depicted in table 5.2. Two limitations are mentioned in the WPM paper: $\delta z << \frac{\lambda_0}{\delta n}$ and $dx \leq \frac{\lambda_0}{2\cdot n_{max}}$. The first limitation is well met in index media with low gradients and the second condition limits the maximum size of the sampling in position space. For a comparison of the BPM with the WPM, the author used Maxwell's Fisheye as inhomogeneous media:

$$n\left(r\right)=\frac{n_0}{1+\left(\frac{r}{r_0}\right)^2}\ . \tag{5.42}$$

This refractive index distribution perfectly images a point source from on side of the Fisheye onto the other side. This should be true for a series of succeeding fisheyes as well. Figure 5.11 shows the BPM and WPM method for a series of five fisheyes. While the BPM field already shows aberrations from the first focal point, the WPM method images the point source again and again. Since the Gaussian source is narrow, the spectrum is composed of higher frequencies and therefore of higher propagation angles, thus the paraxial BPM method is not suitable. In the WPM image the increasing distortions are clearly visible,

$$\boxed{u\left(x,z_j\right)} \qquad \text{Light field at } z_j$$

$$\Downarrow$$

$$\tilde{u} = FFT\left(u\right)$$

$$\Downarrow$$

$$\boxed{u\left(x,z_j+\delta z\right) = \sum_{x}\sum_{\nu_x}\left(\tilde{u}\cdot e^{2\pi i\,\delta z\sqrt{\left(\frac{n\left(x,z_j\right)}{\lambda}\right)^2-\nu_x^2}}\cdot e^{2\pi i\,x\,\nu_x}\right)} \qquad \text{Light field at } z_j+\delta z$$

Table 5.2: Schematic of one WPM step (1D)

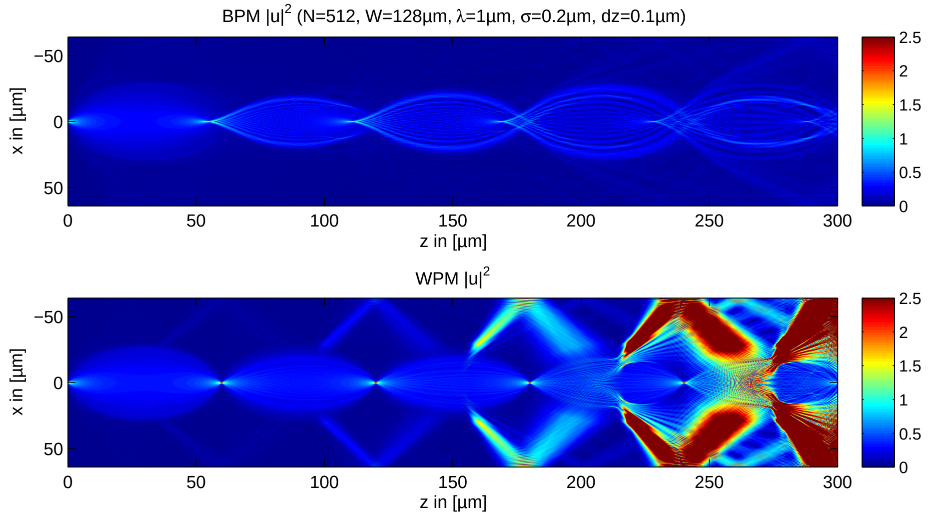

Figure 5.11: Comparison of BPM and WPM with the same parameters for the propagation of light coming from a narrow Gaussian point source

and this with the abidance of the authors' restrictions ($dz = \frac{\lambda_0}{10}$). The energy increases with z, the topic of the following section.

5.4.3 The energy problem of the WPM method

The additional energy is generated by the higher frequency components: figure 5.12 shows the corresponding Fourier spectrum to Figure 5.11. The distortions decrease with higher sampling in x- and z-direction but they cumulate and appear only a few fisheyes later. Since the distortions come from the frequencies near the evanescent limit, one possible way to prevent them is to simply cut off frequencies higher than a certain v_{max}. Which v_{max} is suited depends on the gradient of the refractive index distributions. For smooth gradient profiles like Maxwell's Fisheye, the limitation has not to be as strict as for index profiles with refractive steps. The evanescent limit depends on the index of refraction and this index is not constant in one z-slice. For the same sequence of five fisheyes, in the following comparison frequencies beyond the evanescent limit of the lowest refractive index in a z-slice n_{min}, the mean index n_{mean}, and the maximum index n_{max} are cut off

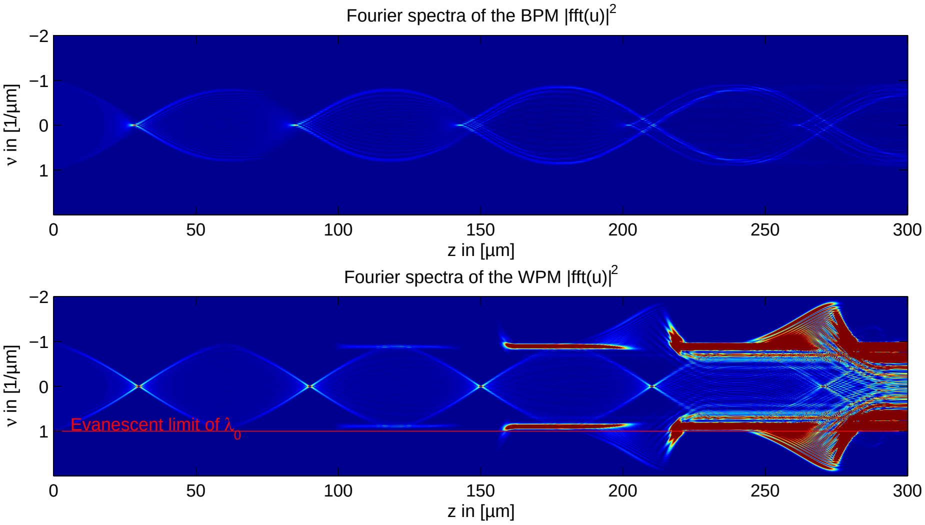

Figure 5.12: Fourier spectra of the BPM and WPM simulation with the fisheye from figure 5.11

$$\nu < \frac{n}{\lambda_0} \tag{5.43}$$

and the energy is plotted as $|u|^2$. The comparison shows an increase in energy for the methods with no cut-off, and cut-off with n_{max}. The more restricted methods with n_{mean} and n_{min} do not show this behavior, where the energy drops very slowly, going from one fisheye to the next. The stability of the WPM method and the energy for the cut-off frequency with n_{mean} is shown in the last figure 5.14 for a series of 25 fisheyes, where the focus behind each fisheye is attained continuously without any distortions.

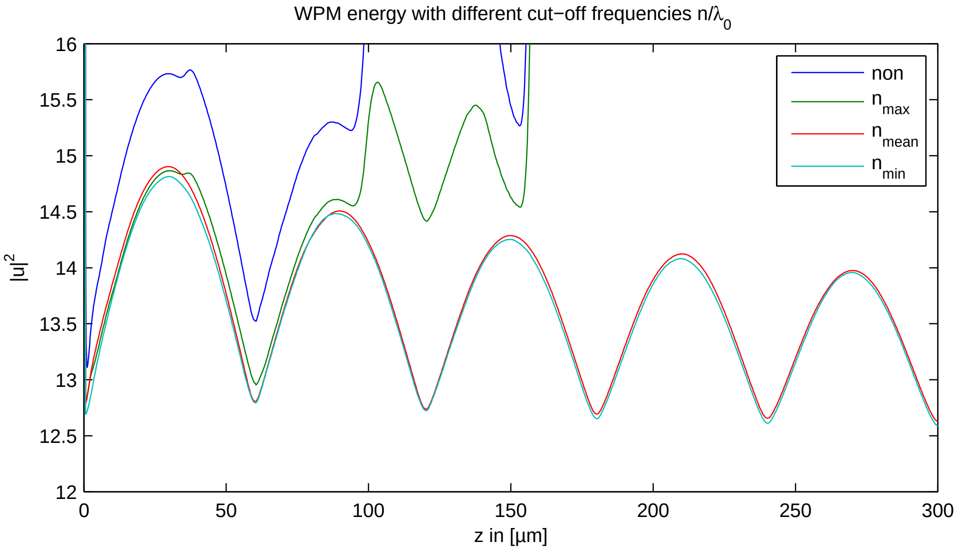

Figure 5.13: Energy development in z-direction for the propagation of light through 5 Maxwell's Fisheyes with the WPM method and different cut-off frequencies ($N = 512$, $\lambda_0 = 1\,\mu\text{m}$, $dx = \frac{\lambda_0}{4}$, $dz = \frac{\lambda_0}{5}$).

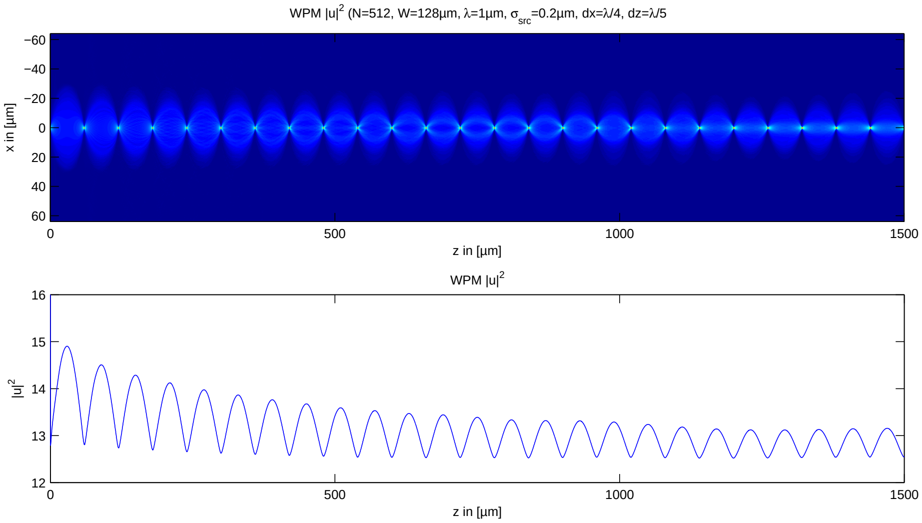

Figure 5.14: WPM propagation through 25 Maxwell's Fisheyes with cut-off frequency $\nu < n_{mean}/\lambda_0$ ($N = 512$, $\lambda_0 = 1\,\mu\text{m}$, $dx = \frac{\lambda_0}{4}$, $dz = \frac{\lambda_0}{5}$).

5.5 Conclusion

Scalar propagation methods in homogeneous and inhomogeneous media have been compared. In homogeneous media, the Rayleigh & Sommerfeld (or PWS) method for distances smaller than $z \leqslant \frac{N\,dx^2}{\lambda}$ is the best choice in terms of accuracy. For longer distances, one has to be careful if plane waves with not negligible energies reach the computation field boundaries. In this case, these waves have to be cut off, for example with a smooth rectangular function with a width depending on the propagation distance z. For even longer distances, the QFQ or 'Fresnel in position space' method is well suited. The computational field scales with increasing distances, and the errors introduced by the paraxial Fresnel approximations are negligible in the far field. The combination allows a precise light propagations from several microns to the far field of several thousand kilometers and more.

In inhomogeneous media, the wave propagation method with adapted cut-off frequencies is a powerful numerical simulation method. The frequency limitations depend on the gradient of the refractive index distribution. For gradient index lenses like Maxwell's Fisheye, the mean index of the z-slice divided by the base wave length $\frac{n_{mean}}{\lambda_0}$ proofed to be a suitable limitation. For distributions with higher gradients or even index steps, the energy development over the propagation has to be carefully investigated and the frequency limitations set accordingly. The ongoing research enhances the WPM from a scalar method to a vectorial method, which can treat polarization effects, Fertig and Brenner [20].

Chapter 6

Simulation of UV deep lithography

In the early 1970s, lithography was considered an art. It was the time when Rick Dill and his team started their work to transform the art into a science. The result are the four so called 'Dill papers' ([16],[17],[29],[18]) from 1975. The Dill papers were the first approach to model the lithography process and the most cited papers in this research field. In the following 34 years, the theories and models on lithography improved and are nowadays an indispensable tool for most people working with lithography (see Mack [37]). Commercially available software like SAMPLE, PROLITH, or Dr. LiTHO model the complete lithography process and provide all features from simulation of the imaging system over optical proximity correction down to the chemistry of the resist while exposing and developing.

Simulation of the lithography process can be divided into three main parts: simulation of the illumination system in front of the mask, diffraction on the mask and propagation of light into the resist, and simulation of the chemical processes to obtain the final structure. The illumination system used in this work has already been analyzed in Part 2 and the light pattern in front of the mask is known. The post exposure process is composed of the post exposure bake, where the polymerization happens, and the development where the non polymerized molecules are dissolved. This area is still an ongoing research field (see Schmid et al. [44]). The scope of this chapter is not to present another complete simulation software but to analyze the influence of a given light distribution in front of the mask in order to simulate the energy distribution inside the resist on the basis of the previous chapter on scalar wave propagation methods with an extension for absorbing media.

6.1 PWS in absorbing media

During exposure the chemical properties of a photoresist change according to the exposure dose and resist properties. The proper simulation of the intensity inside the resist is the basis for the following chemical considerations to determine if molecules are dissolved or not. The presented scalar propagation methods in the previous chapter were based on homogeneous non absorbing media for coherent light. The PhD student Liu extended the scalar propagation method for absorbing media [34, chap. 4]: In absorbing media, the refraction index is given by

$$\hat{n} = n + i\ \kappa \tag{6.1}$$

and the propagation of a plane wave by

$$E\left(x, y, z)\right) = E_0 \cdot e^{i(k_x \cdot x + k_y \cdot y + k_z \cdot z)} \cdot e^{-\gamma_z\ z} \tag{6.2}$$

with k_z changing from $k_z^2 = n^2 k_0^2 - k_x^2 - k_y^2$ to

$$k_z^2 = \frac{1}{2} \cdot \left[\left(n^2 - \kappa^2\right) k_0^2 - k_x^2 - k_y^2 + \sqrt{\left[\left(n^2 - \kappa^2\right) k_0^2 - k_x^2 - k_y^2\right]^2 + 4 n^2 \kappa^2 k_0^4}\right] \tag{6.3}$$

and

$$\gamma_z = n\ \kappa\ k_0^2\ \frac{1}{k_z}. \tag{6.4}$$

This is an inverse relation between the propagation and the attenuation part.

In the following, the Rayleigh and Sommerfeld diffraction integral will be adapted to absorbing media. In homogeneous non absorbing media the diffraction integral is

$$u\left(\vec{r}_\perp, z\right) = \iint \tilde{u}\left(k_\perp, 0\right) \cdot e^{izk_z} \cdot e^{i\left(\vec{k}_\perp \vec{r}_\perp\right)} \frac{d^2 k_\perp}{\left(2\pi\right)^2} \tag{6.5}$$

with $k_z = \sqrt{\left(nk_0\right)^2 - \left(\vec{k}_\perp\right)^2}$.

For absorbing media, the new k_z from equation 6.3 has to be inserted and the attenuation part $e^{-\gamma_z \cdot z}$ added. This delivers

$$u\left(\vec{r}_\perp, z\right) = \iint \tilde{u}\left(k_\perp, 0\right) \cdot e^{izk_z} \cdot e^{-\gamma_z \cdot z} \cdot e^{i\left(\vec{k}_\perp \vec{r}_\perp\right)} \frac{d^2 k_\perp}{\left(2\pi\right)^2}. \tag{6.6}$$

With $k_\perp = 2\pi\nu_\perp$ and the abbreviation

$$w = \frac{\left(n^2 - \kappa^2\right)}{\lambda^2} - \nu_\perp^2, \tag{6.7}$$

k_z is

$$k_z = \sqrt{2}\pi \cdot \left(w + \sqrt{w^2 + 4n^2 \frac{\kappa^2}{\lambda^4}}\right)^{\frac{1}{2}} \tag{6.8}$$

and the integral in ν becomes

$$u\left(\vec{r}_\perp, z\right) = \iint \tilde{u}\left(\nu_\perp, 0\right) \cdot e^{izk_z} \cdot e^{-n\ \kappa\ k_0^2\ \frac{1}{k_z} \cdot z} \cdot e^{2\pi i\left(\vec{\nu}_\perp \vec{r}_\perp\right)} d^2\nu_\perp. \tag{6.9}$$

For the following comparison of a PWS propagation with and without absorption, a rectangular aperture ($l = 50\,\mu$m) is illuminated with a perpendicular incident plane wave. The 3D intensity profile is calculated in a volume with $N_{x,y} = 512$, $d_{x,y} = 0.25\,\mu$m, $d_z = 1\,\mu$m, $\lambda = 365\,$nm, $n = 1.7$, and $\kappa = 0.0002$. Figure 6.1 shows a y-slice at $y = 0$ from the 3D volume for non absorbing and absorbing media.

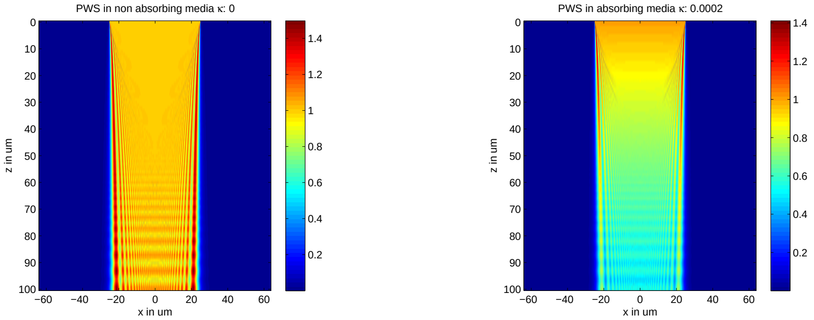

Figure 6.1: Mask diffraction on a 50 μm rectangular aperture and light propagation in non absorbing and absorbing media calculated with the adapted PWS method. Simulation properties: $N_{x,y} = 512$, $d_{x,y} = 0.25\,\mu$m, $d_z = 1\,\mu$m, $\lambda = 365\,$nm, $n = 1.7$, and $\kappa = 0.0002$.

6.2 Partially coherent illumination

Until now in this work, mask diffraction of a single plane wave was considered. Chapter 2.1 about UV illumination systems showed that a real illumination source consists of a broad angular spectrum. Each point in the Fourier domain corresponds to a plane wave propagating at a discrete angle with a certain energy. Additionally, most UV illumination systems emit not coherent but partially coherent light, such as illumination systems with mercury bulbs. For a more realistic simulation, the angular spectrum of the illumination source has to be analyzed, decomposed into plane waves, each plane wave diffracted at the mask and propagated into the resist, and finally the intensities of all plane waves accumulated to receive the resulting intensity 3D volume.

6.2.1 Scaling of the angular spectrum of the illumination source

The measurement of the angular spectrum of an illumination system was described in chapter 2.1.1. For the simulation, the measured data has to be scaled to fit to the grid given by the sampling in the frequency space. The input data consists of an image representing the angular spectrum of the illumination system. Each pixel corresponds to a certain angle and the pixel size ps_c to the sampling of the camera. The measurement image is shown in figure 6.2. The measurement shows clear signs of reflections causing a shifted ghost image. The second figure 6.3 depicts the adapted measurement, converted to gray scale and the ghost image manually retouched. The relation between the propagation angle δ and the image sampling ps_c was

$$\delta = atan\left(\frac{n \cdot ps_c}{f}\right) \tag{6.10}$$

with the number of pixels from the image center n. For the scalar propagation theories, the relation between propagation angle ϑ and frequency sampling $d\nu$ was

$$\vartheta = \arcsin\left(\lambda_0 \cdot m \cdot d\nu\right). \tag{6.11}$$

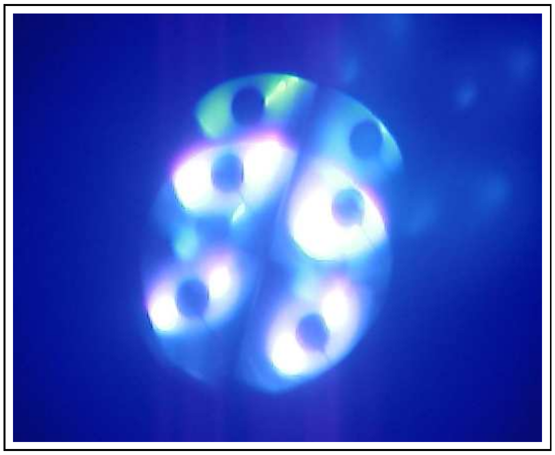

Figure 6.2: Measurement of the angular spectrum of the mask aligner with aperture $r = 4\,\mathrm{mm}$

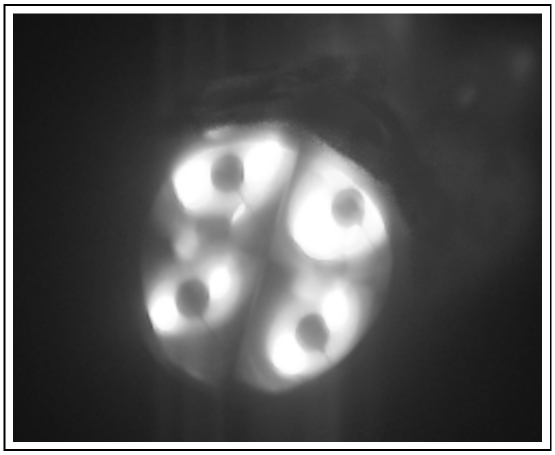

Figure 6.3: Converted and edited measurement image

For small angles one can approximate $\sin(\alpha) = \tan(\alpha)$ obtaining the scaling relation

$$c_{scal} \cdot \frac{n \cdot ps_c}{f} = \lambda_0 \cdot m \cdot d\nu \tag{6.12}$$

or for $n = m$

$$c_{scal} = \frac{\lambda_0}{N\ dx} \cdot \frac{f}{ps_c}. \tag{6.13}$$

With the measurement parameters ($f = 60\,\mathrm{mm}$, $ps_c = 6.25\,\mu\mathrm{m}$) and the simulation parameters ($N_{x,y} = 512$, $d_{x,y} = 0.25\,\mu\mathrm{m}$, $\lambda = 365\,\mathrm{nm}$) the scaling factor becomes $c_{scal} = 27.4$. This means that the measurement image has to be scaled down by this factor. The resulting image is shown in figure 6.4.

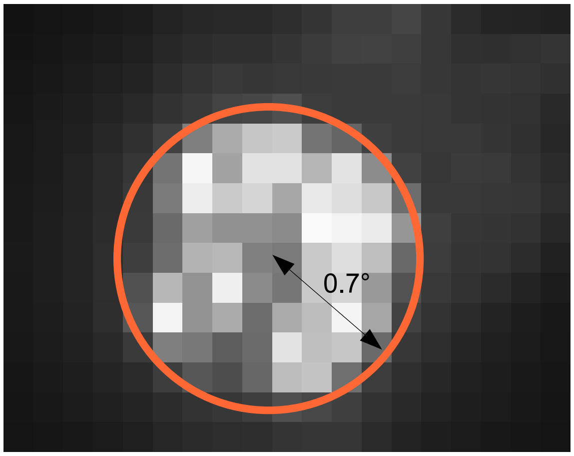

Figure 6.4: Scaled image from the angular measurement

With an aperture size of ≈ 4.5 pixels, formula 6.11 delivers the corresponding aperture angle as 0.7° which is in agreement with table 2.2 on page 16.

6.2.2 Decomposition of the plane waves and partially incoherent superposition

Each pixel in the scaled measurement image 6.4, the angular spread of the light source, corresponds to a plane wave impinging on the mask at a certain angle. The convolution in Fourier space of mask and angular spectrum corresponds to a multiplication in position space

$$u_{0pw} = u_{mask} \cdot \mathcal{F}^{-1}\left(\tilde{u}_{pw}\right) \tag{6.14}$$

with the index $_{pw}$ standing for the field of one plane wave and u_{mask} for the binary mask field. After propagating u_{0pw} according to formula 6.9 and calculating the 3D intensity distribution for each plane wave, all intensity distributions have to be accumulated to receive the final partially coherent 3D intensity distribution for a partially coherent illumination source.

$$I_{sum} = \sum_{pw} \left| P_{pws2}\left(u_{mask} \cdot \mathcal{F}^{-1}\left(\tilde{u}_{pw}\right)\right)\right|^2 . \tag{6.15}$$

To show the influence of a broader angular spectrum, the mask diffraction and light propagation in absorbing media for the same parameters like in figure 6.1 is calculated once for a single plane wave illumination and once for the angular distribution of figure 6.4. Figure 6.5 depicts the intensity distribution in a z-slice at $z = 100\,\mu$m.

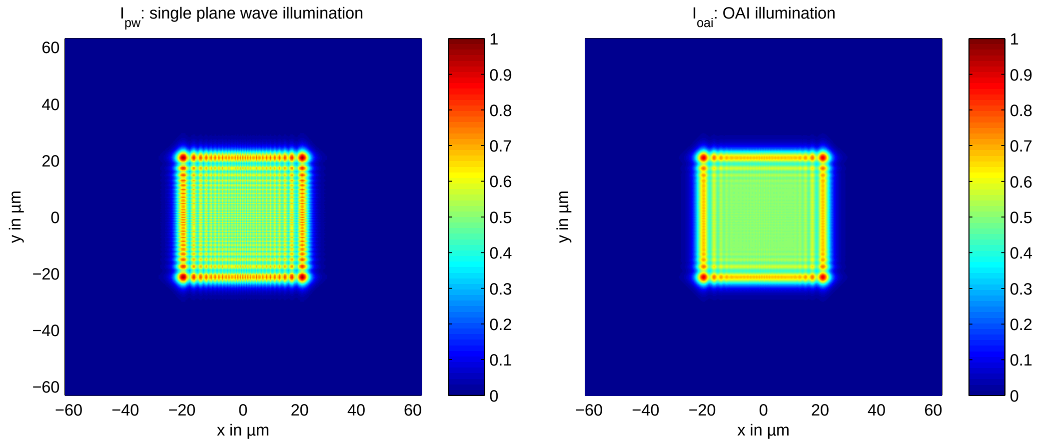

Figure 6.5: Mask diffraction on a $50\,\mu$m rectangular aperture and light propagation in absorbing media for $z = 100\,\mu$m calculated with the adapted PWS method - on the left with a single plane wave illumination and on the right with the spectrum of the mask aligner with the aperture $r = 4\,$mm. Simulation properties: $N_{x,y} = 512$, $d_{x,y} = 0.25\,\mu$m, $\lambda = 365\,$nm, $n = 1.7$, and $\kappa = 0.0002$.

The comparison shows the influence of the real spectrum as a kind of smoothing of the intensity distribution. Due to the small width of the angular spectrum of $\vartheta = \pm 0.7°$, the structure shows no signs of broadening.

6.3 Development model

For a realistic simulation of the chemical processes during exposure and the following prebake and development steps, detailed knowledge about the chemical and physical properties is needed (see Schmid et al. [44]). With this knowledge, one basically solves a transport equation and calculates the polymerization degree. For the scope of this thesis, these processes are simplified to a cut-off threshold, which depends only on the intensity distribution. In this simple model, the developer dissolves the resist, where the intensity is below a certain threshold. The result of this model is a 3D volume plot. For the simulation, the mask aligner light source with an aperture $r = 4\,\text{mm}$ was used and the resist simulated with an absorption of $\kappa = 0.0002$. For the 3D volume, a z-slice every 4μm was calculated, see figure 6.6.

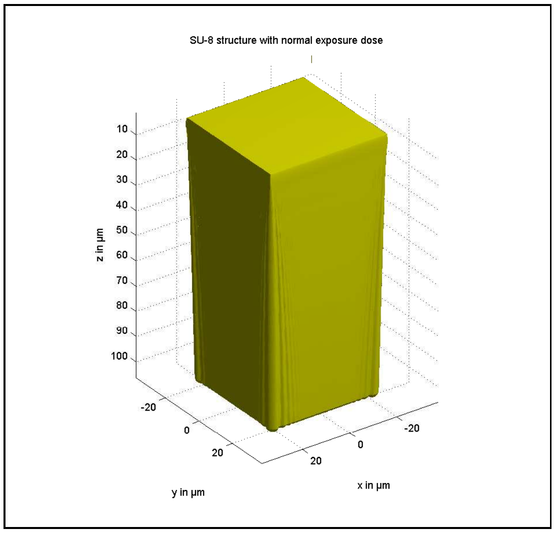

Figure 6.6: Normal exposure: remaining resist structure after development, simulated by propagation of partially coherent light in absorbing media with a following simplified development step

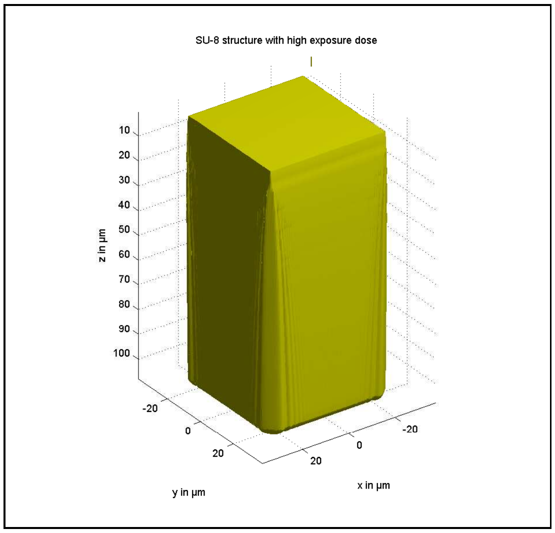

Figure 6.7: High exposure: same simulation as in the left image but with a reduced threshold to simulate overexposure

While the left figure belongs to the class of normal structures with a slight undercut, the structure in the right image 6.7 shows clear signs of overexposure due to a reduction of the threshold, which corresponds to an increase in the exposure dose.

The riffles shown in both simulations can be verified on some SU-8 structures. Figure 6.8 shows a magnified rectangular SU-8 structure and figure 6.9 a magnified image from the simulation shown in figure 6.6.

Even though the periodicity is only akin, the riffles at the edges are very similar and suggest that these riffles are based on partially coherent interferences.

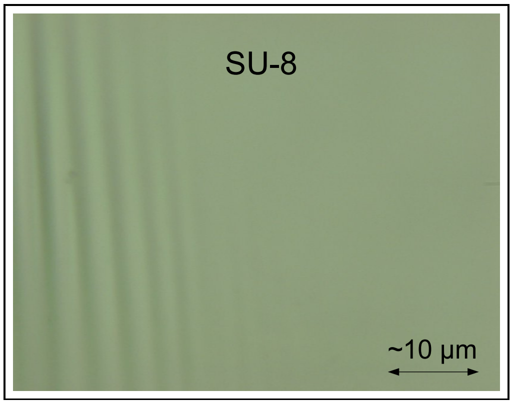

Figure 6.8: Riffles on a SU-8 sidewall edge

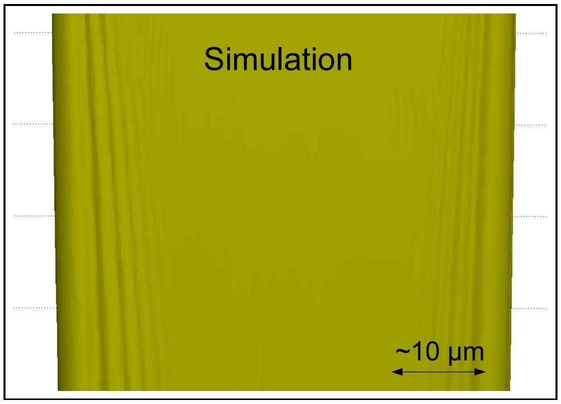

Figure 6.9: Simulation of a SU-8 rectangular structure

6.4 Conclusion

The simulation of lithographic processes helps to understand the underlying background. The light propagation in absorbing media from Liu was adapted for the PWS propagation method to simulate the absorption of a given resist. While each plane wave itself is propagated coherently, a partially coherent light source can be simulated by decomposing the angular spectrum in single plane waves, propagating each plane wave, calculating the intensity profile, and accumulating all intensity profiles. For a first approximation of the resulting lithographic structures, an intensity threshold was used to decide which parts of the volume will be dissolved and which will remain. For a real application of this simulation, the parameters for the resist, in this case SU-8, have to be analyzed and the simulation adapted.

Part III

Applications of miniaturized components

Chapter 7

Optical interconnects in the Future DAQ project

At the GSI (Gesellschaft für Schwerionenforschung) in Darmstadt a new Facility for Antiproton and Ion Research (FAIR project) is planned to be built until 2016 with a cost estimation of around 1.2 billion Euro [11]. It is an international accelerator facility of the next generation. At its heart is a double ring facility with a circumference of 1100 meters. A system of cooler-storage rings for effective beam cooling at high energies and various experimental halls will be connected to the facility (figure 7.1).

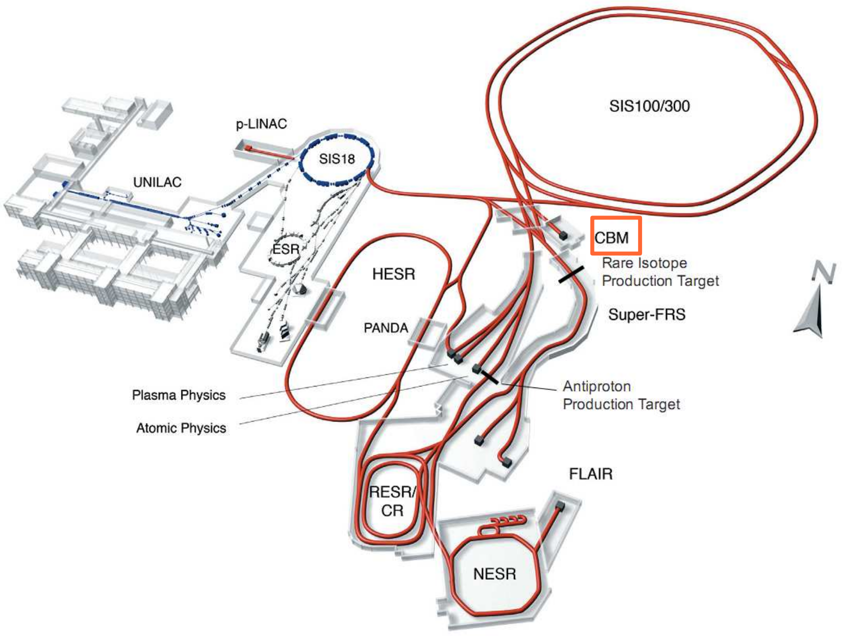

Figure 7.1: Concept of the FAIR project at the GSI in Darmstadt (image from GSI Darmstadt)

The CBM project is one of the experiments at FAIR. The goal of the research program on nucleus-nucleus collisions at the new accelerator facility at GSI is the investigation of highly compressed nuclear matter. Matter in this form exists in neutron stars and in the core of supernova explosions. In the laboratory, super-dense nuclear matter can be created in the reaction volume of relativistic heavy-ion collisions. The baryon density and the temperature of the fireball reached in such collisions depend on the beam energy. In other words, by varying the beam energy one may, within certain limits, produce different states and phases of strongly interacting matter.

The experimental task is to identify both hadrons and leptons and to detect rare events in a heavy ion environment. The challenge lies within the selection of rare events in nucleus-nucleus collisions with charged particle multiplicities of about 1000 per central event at reaction rates of up to 10 MHz. Such measurements require fast and radiation hard detectors, fast and self-triggered read-out electronics, a high-speed data acquisition system, and online event selection based on full track reconstruction. The CBM experimental setup comprises the following detector components (see CBM Progress Report 2008 [8]): Silicon Tracking System (STS), Micro-Vertex Detector (MVD), Ring Imaging Cherenkov detector (RICH), Transition Radiation Detector (TRD), Muon Chamber/Absorber System (MUCH), Resistiv Plate Chambers (RPC), Electromagnetic Calorimeter (ECAL), Projectile Spectator Detector (PSD), see concept in figure 7.2.

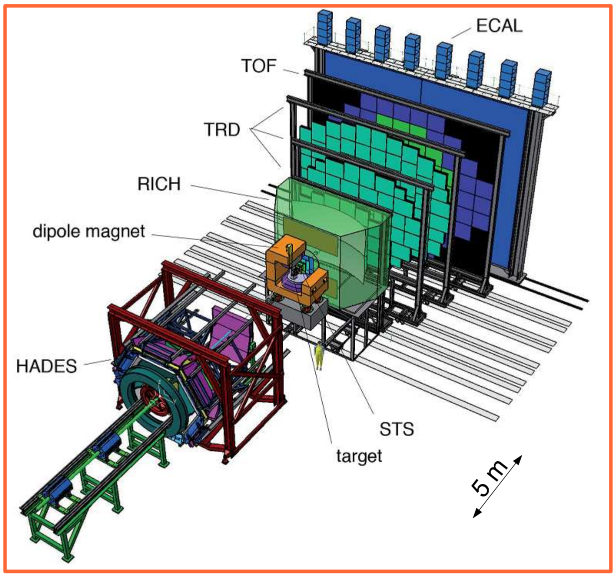

Figure 7.2: Concept of the CBM detector (image from GSI Darmstadt)

The high speed data acquisition system is the content of the Future Data Acquisition project (Future DAQ), where as part of this work, a concept for optical interconnects had to be developed and a demonstrator had to be built.

The chapter starts with a description of the developed optical network hierarchy of the CBM detector and explains the need of pluggable optical interconnects based on VCSEL-fiber-couplers. The chapter continues with the development of miniaturized integrated fiber couplers, the main contribution of this work. This coupling concept is then used on the demonstrator board and the advantages for Active Optical Cables are discussed at the end of the chapter.

7.1 Preliminary design of an optical network hierarchy

Huge amounts of data will have to be transported from the detector to the computer nodes. Estimations refer to 6k serial links at 2.5 Gbit/s . With 25 m length and the demand of radiation hardness, optical links are favored over electrical interconnects. Additionally, the read out boards are on different voltage levels ±300 V and in the reach of very strong magnetic fields, making the task for electrical interconnects even more complicated. One other advantage of optical transmission is the reduction in weight and size. Calculations of the construction engineers came to the conclusion that the foundation of the building had to be made stronger to withstand the huge weight of copper for the electrical transmission cables and the largely reduced size comes to hand in a room, where space is a valuable commodity.

Fortunately, this is not the first accelerator facility which operates with optical links. The CMS detector of the large hadron collider (LHC) at Cern, established 65k optical links at up to 2.5 Gbit/s. The technical design used is from the year 2000 but some very important insights from their "Lessons learned" have to be kept in mind (see Vasey [53], Gan et al. [22], and Troska et al. [52]). Next to the insight about problems concerning large-scale production and quality management, three important lessons were: use commercial off-the-shelf as much as possible, do not use pigtails, and radiation hard VCSELs and fibers are available on the market.

In order to avoid pigtails, pluggable cables are needed to cross the first 25 m. Since the read out boards are electrical and the transmission has to be optical, the idea was born to develop a cable which connects with electrical pins, convert the signal into an optical one inside the plug, and to transmit it via fiber. This concept dates back to 2004 and is nowadays called Active Optical Cables (AOC), a very fast growing market. The electronics for the electro-optical conversion, the read out boards, and the protocols are designed by the group around Prof. Brüning from the Chair of Computer Engineering, University of Heidelberg, and are not part of this thesis. The focus here is on the optics.

The 6k serial links have to cover the 25 m from the detector to the first shielded room. The patch box here bundles the cables to ribbon cables with 12 fibers each, reducing the number for connects from 6k to 500 to cover the 150 m to the nodes. The concept is depicted in figure 7.3.

From the 6k links only 2k-4k are needed, the rest are spare fibers for dead links. The technique to bundle fibers in this way was also used by the LHC consortium; they even added another bundling stage to concentrate 8x12 fibers into one multi ribbon cable. These techniques are state of the art but research in the field of coupling VCSELs to fiber in a very compact and cost efficient way without pigtails is needed. This is the content of the

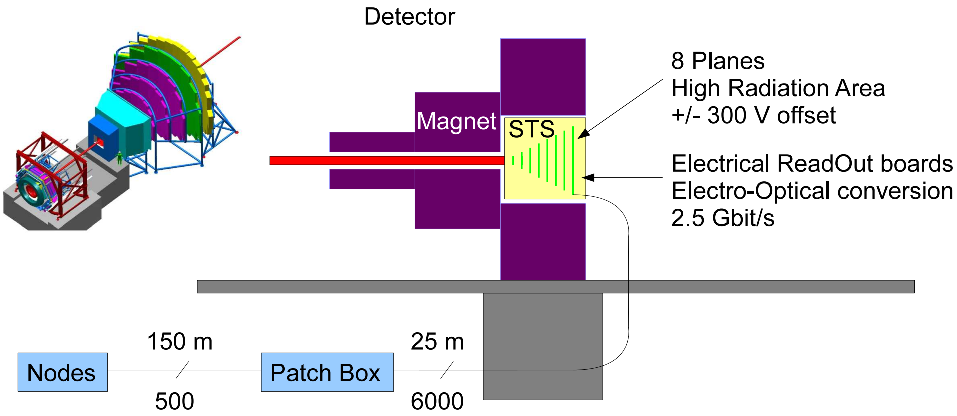

Figure 7.3: Concept of the network hierarchy for the CBM detector

following paragraphs after a brief introduction into VCSELs.

7.2 VCSELs

The invention of the VCSEL (Vertical-Cavity Surface-Emitting Laser) in 1979 by Soda et al. [49] and the first demonstration at room temperature by Koyama et al. [30] finally provided the communication market with a compact and high-performance light source to replace the edge emitting lasers. VCSELs have many advantages: a perpendicular emitter, low power consumption, cost efficient production, on wafer testing, improved beam characteristics, high modulation bandwidth, and they allow compact 2D arrays. The typical beam cone angle of a VCSEL, the angle where the radiation drops to $1/e^2$, is around 12.5°. They are fabricated basically as top or bottom emitting versions depicted in figure 7.4 and figure 7.5.

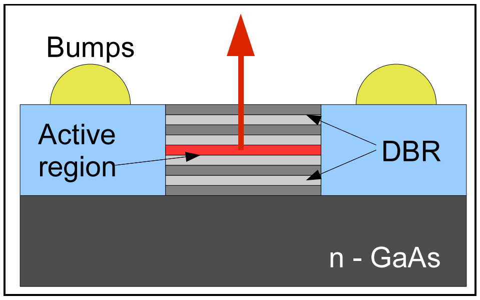

Figure 7.4: VCSEL top emitter: the light is emitted on the side of the bumps

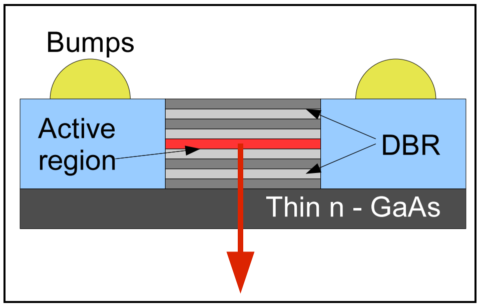

Figure 7.5: VCSEL bottom emitter: the light is emitted through the substrate

While the top emitter is the standard version of the VCSEL, the drawback results from the emitted light and bumps being on the same side. If the top emitting VCSEL is contacted by wire bonds, one has to take care while coupling not to damage these wires, or if the VCSEL is flip chipped on a substrate, one has to guide the light through the substrate. Both options reduce the degree of freedom for the optical coupling design. The bottom emitting VCSEL radiates through the bulk substrate, which has to be thinned in order to keep the attenuation small. The benefit of the more complex fabrication process is that these VCSELs can be flip chipped on any board or chip, emitting the light in the free space above; no wires complicate the coupling into wave guides. In the following coupling concepts, all VCSELs are bottom emitting ones.

7.3 Concepts coupling VCSEL to fiber

VCSELs are typically fabricated on a 250 μm grid, which should be met by the fiber coupling structures in order to couple VCSEL arrays compact with fiber arrays. The standard method is butt- or direct coupling, where the fiber is directly mounted on top of the VCSEL. If the perpendicular coupling is not wanted, for example if the fiber has to be in the plane of the board and the space above the VCSEL is limited, either a VCSEL, bonded on a 90° tilted plane, or a mirror for deflection is needed. The three concepts are shown in figure 7.6.

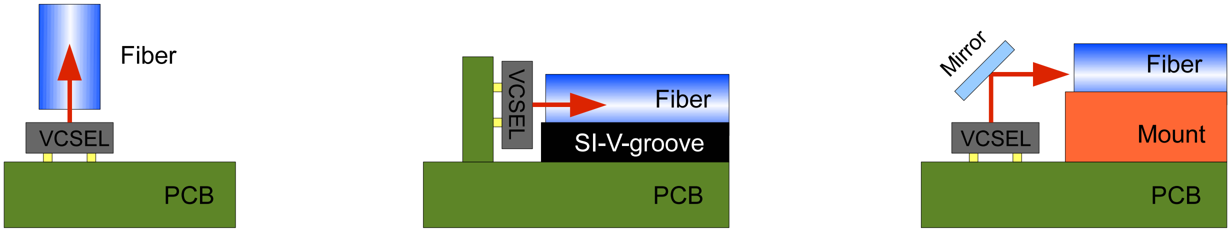

Figure 7.6: Concepts for VCSEL to fiber coupling: direct coupling on the left, tilted VCSEL and fibers in SI-V-grooves in the middle, and coupling via a mirror on the right.

Each concept can be expanded with additional components to increase the coupling efficiency, for example with lenses to image the VCSEL into the fiber. All coupling designs are a trade-off between costs, coupling efficiencies, and power consumption. Lenses increase the coupling efficiency and therefore decrease the power consumption of the system, but they have to be fabricated, aligned, and mounted causing additional costs. The goal here is to develop a concept which combines all advantages without additional costs.

7.3.1 Coupling concepts

Direct coupling is the standard technique to obtain high coupling efficiencies without additional components by minimizing the distance between VCSEL and fiber. Automated high precision alignment stages position and fix single VCSELs with fibers and do the packaging. While this technique is favored for single connectors, array connectors need additional components to guide the fibers within the adapted grid.

Nowadays in 2009, the common techniques for compact in plane array coupling (figure 7.6, middle) are VCSELs bonded on a 90° tilted mount, which is aligned with a module containing V-grooves for fiber alignment. The V-grooves are fabricated either by etching in SI along the crystal axis, or in other materials with micro machining and laser applications. While the V-groove fabrication is well understood, the tilted bonding and alignment still cause higher fabrication costs.

In 2002, K.-H. Brenner and U. Bruening from the University of Heidelberg had the idea for a compact integrated VCSEL to fiber coupler which combines deflection of the emitted light by 90°, high precision fiber alignment, and a simplified fiber insertion.

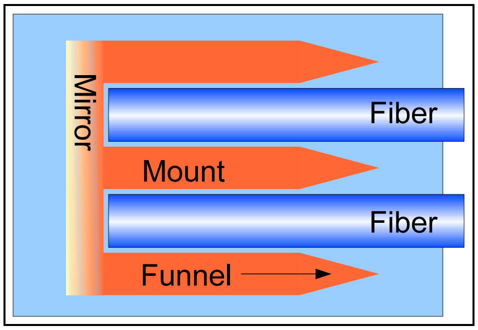

Figure 7.7: Top view: new integrated fiber coupling design for two channels with funnels to simplify fiber insertion

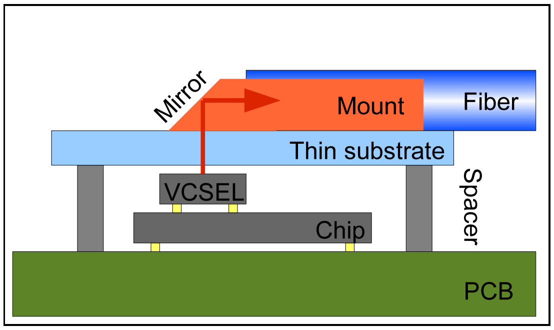

Figure 7.8: Side view: new integrated fiber coupling design with VCSEL flip-chipped on a driver and serializer chip, spacers, and the integrated fiber coupling mount with 45° mirror on a thin glass substrate

The concept is depicted in figure 7.7 and figure 7.8. The primary challenge here lies in the production of the integrated fiber mount containing the mirror and to find suitable replication techniques for large-scale production. The steps leading to the final design are described in the next paragraph after a short introduction into the main influences concerning coupling efficiencies.

7.3.2 Coupling efficiency

Next to the production costs and size, the coupling efficiency of a fiber coupler is the most important property of the design. A low cost design will not be accepted by the market if the coupling efficiency is too low, and another design involving additional costly components to increase the efficiency will not be successful either. Coupling efficiency, or coupling loss, of a fiber coupler depends on the alignment of the fiber with the coupler, their properties, and the distance in between. Alignment faults are misalignment in x- and y-direction and angular mismatch, which appear if the fiber is not exactly centered on the optical axis of the laser. The numerical aperture of the fiber also has to be at least as big as the one of the laser, or additional attenuation will be introduced. The distance or gap between the fiber and the laser is separately mentioned here because of its huge impact on the coupling loss and because in some designs this gap cannot be reduced below a certain value. While direct coupling allows a minimization of the gap into regions close to zero, light deflection on a mirror involves a minimum distance between laser and fiber only due to pure geometrics.

The influence of the gap distance z on the coupling efficiency is depicted in figure 7.10 for a coupling simulation of a VCSEL with a fiber in relation to the gap size z (setup see figure 7.9) with the simulation properties: VCSEL with Gaussian beam profile and a cone angle of 12.5° ($NA = 0.216$), perfectly aligned fiber with matching NA, 'mixed' simulation mode with 33 rings.

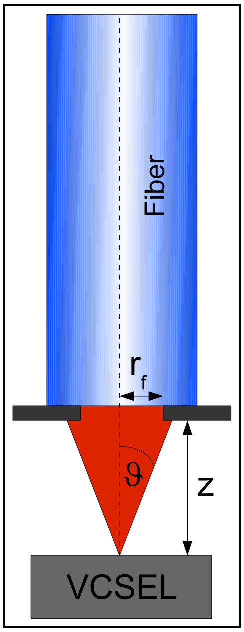

Figure 7.9: Simulation setup

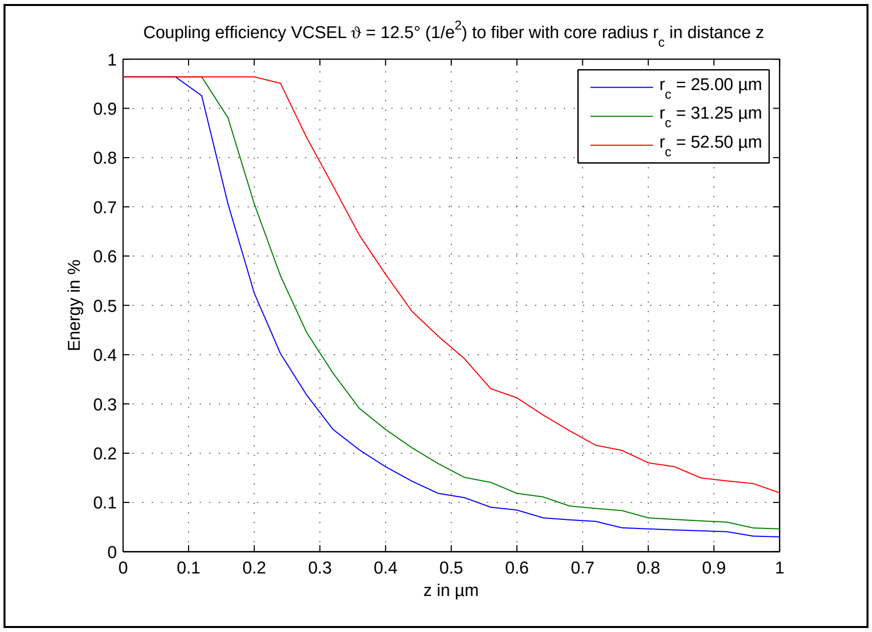

Figure 7.10: VCSEL to fiber coupling efficiency in relation to gap size z (RayTracer: gaussian point source with 33 rings in mixed mode)

The diagram shows how strong the coupling efficiency depends on the distance z, for example the coupling efficiency of a $r_f = 31.25\,\mu$m multimode fiber drops from 70% to 25% going from $z = 200\,\mu$m to $z = 400\,\mu$m.

These results make it clear that VCSEL to fiber coupler designs based on flat mirrors and with inter media substrates are limited to low coupling efficiencies due to the design. Ways to improve the performance of fiber couplers based on mirrors and their fabrication techniques are presented in the following paragraph.

7.4 Integrated fiber couplers

The combination of alignment structure, mirror, and funnel into one integrated structure promises a very compact VCSEL to fiber coupling design. UV deep lithography as fabrication technique was chosen, because it is capable of feature sizes in the micron range with high aspect ratios. The first integrated fiber coupler was fabricated in 2004 by a modified SU-8 lithography process for slanted structures involving water immersion. Two years later, in 2006, considerations about large-scale production and replication techniques lead to the second version. The third version from 2008 finally increased the coupling efficiency by optimizing the mirror surface. In all three versions, the space between fiber and mirror was filled with UV-adhesive to fix the fiber and also to match the indices. The three designs are described in the following paragraphs.

7.4.1 Version 1

The main task for the first version of a slanted fiber coupler was the development of the UV deep lithography process with inclined exposure and water immersion (see chapter 2.2.4). As a demonstration of this concept, figure 7.12 shows a camera image from the bottom of the coupler with a light guiding fiber inserted. The mirror functionality is based on the total reflection between the slanted mount and the air. The space between fiber and mirror structure has therefore to be filled with an index matching material. UV adhesive is suitable and acts as index matching and fiber fixation at the same time.

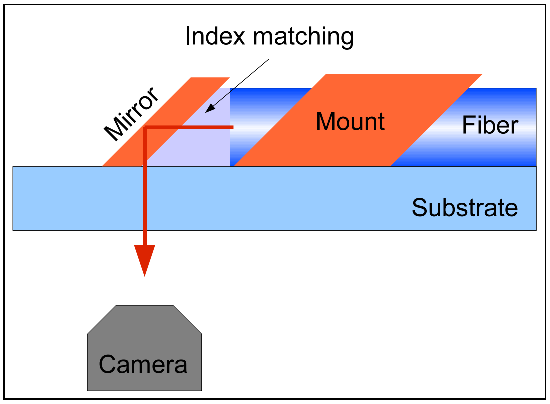

Figure 7.11: Version 1: coupling concept

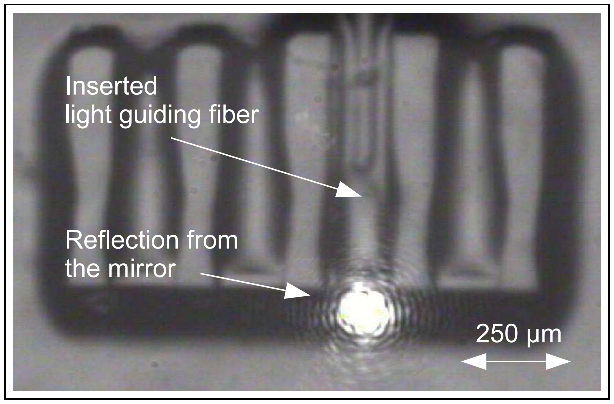

Figure 7.12: Version 1: view through the substrate onto the fiber mount for four channels. The inserted fiber guides light which is deflected on the mirror.

The reflections shown in the camera image are a proof for the principle of the coupling concept. The form of the reflection, a circular area with aberrations, is a first sign of a sufficient surface quality obtained by the UV deep lithography process.

7.4.2 Version 2

Since the lithographic fabrication of SU-8 structures is not the best choice for large-scale production, the structure has to be altered to meet the demands on master structures for replication processes like soft lithography (see chapter 3.2). Soft lithography is a molding technique, which only tolerates marginal undercuts. The slanted structures with 45° on both sides are definitely out of scope. The undercut has to be filled with a second perpendicular exposure, see figure 7.13.

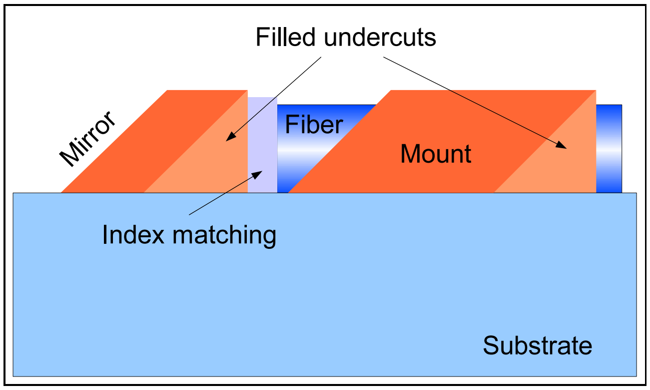

Figure 7.13: Version 2: undercuts from inclined exposure are filled with a second perpendicular exposure step

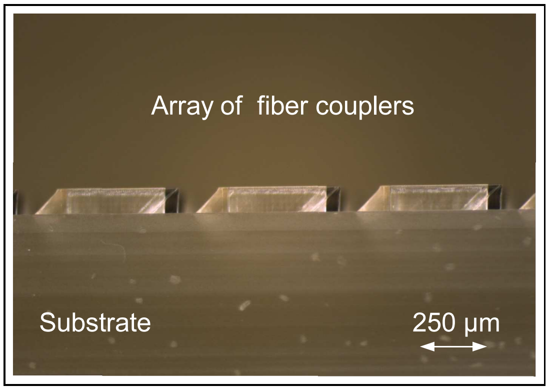

Figure 7.14: Version 2: array of SU-8 fiber couplers fabricated by double exposure

Without filling the undercuts, the replication is needlessly complicated. With the undercuts filled, the structures are ready for large-scale production with soft lithography. However one basic problem remains: the low coupling efficiency.

7.4.3 Version 3

The deflection of light on the mirror has not only the drawback that the distance between the VCSEL and the fiber is increased, resulting in a reduced coupling efficiency, but also offers the possibility to use the mirror as a focusing device. The laser scanner, used in this work to generate the masks for the contact UV lithography, is also capable of writing partially circular rings. This allows to give the mirror a circular shape and to integrate a focusing effect for one axis into the device. A mask with a circular aperture and exposed with inclined radiation produces a slanted SU-8 cylinder with a focusing effect similar to a cylinder lens. The concept is depicted in figure 7.15.

In order to determine the optimal radius of curvature, and to account for all the different layers of air, substrate, replicated material, fiber, etc., the RayTracer from chapter 4 was developed. The main features of the RayTracer are: accurate calculation of the energy transfer on index boundaries, customized surfaces, Gaussian sources, and optimization features. The reflection calculation for a slanted cylinder is described in chapter 4.2.1.

The setup for the version 3 coupling simulation and optimization with all important dimensions is depicted in figure 7.16 with a 3D plot from the RayTracer in figure 7.17.

The optimal radius depends primarily on the optical path length between VCSEL and fiber and is kept fixed for the simulation. With a flat mirror, the simulated coupling

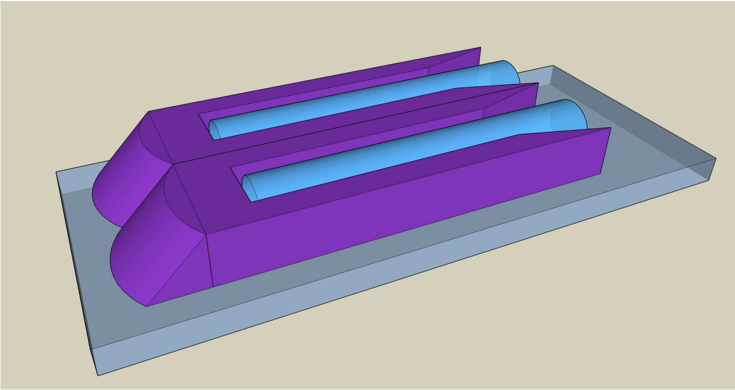

Figure 7.15: Version 3: fiber coupler with curved mirror

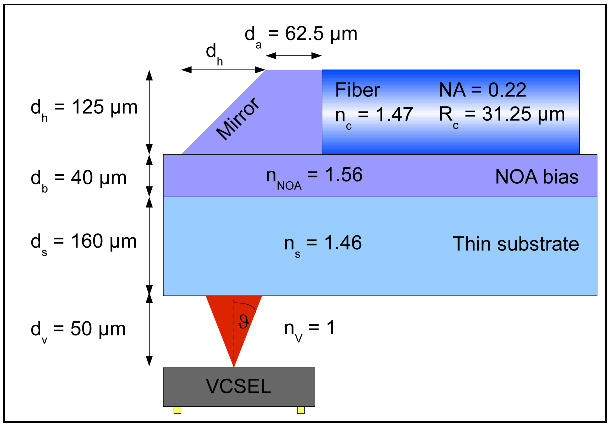

Figure 7.16: RayTracer simulation scenario with the lateral dimensions and refraction indices

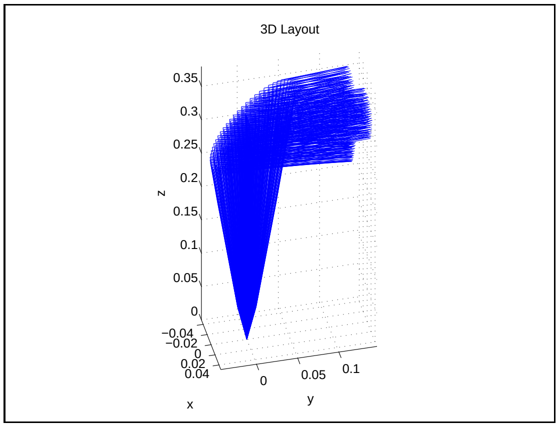

Figure 7.17: RayTracer 3D plot of the scenario with a curved mirror

efficiency for this setup is 39.5%. The increased efficiency in relation to the radius of curvature of the mirror is simulated in 'mixed-mode' for 40 rings and the VCSEL as technical Gaussian point source with 12.5°.

The plot in figure 7.18 shows an optimum around $r_{mirror} = 174\,\mu\text{m}$ with a coupling efficiency of 62%. This corresponds to a gain of 57% in relation to the efficiency of a flat mirror. The losses for the optimal curved mirror result from: index boundaries 10.5%, fiber core aperture 89%, and fiber NA missmatch 0.5%.

7.4.4 Perfect mirror surface

If the mirror surface is not limited by fabrication restrictions and can be optimized as free form surface, what would be the perfect surface profile? One way to find an answer to this question are numerical optimizations, starting with a flat surface and step by step deforming the surface trying to reach an optimal coupling efficiency. Another method from the

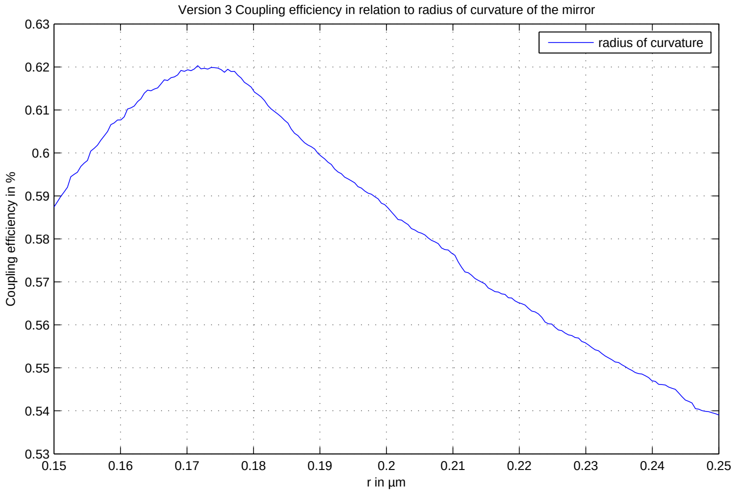

Figure 7.18: Version 3: fiber coupler efficiency in relation to the mirror's radius of curvature

field of beam shaping generates mathematical equations describing the ray transformation of the surface and solves, again numerically, a complex equation system in order to find the optimal surface.

For the very special case of the fiber coupler, mathematicians have already found a solution. The geometrical form of a spheroid, an ellipsoid with two of the three main axis being equal ($a = b$, c), has the property to reflect a ray starting at one focal point always in a way that the ray goes through the second focal point. The principle is depicted as RayTrace simulation for a 2D ellipse in figure 7.19.

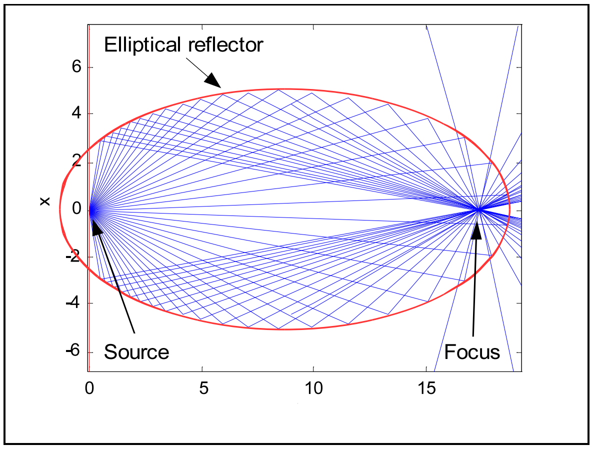

Figure 7.19: RayTrace simulation of an elliptical reflector with the source in the left focal point

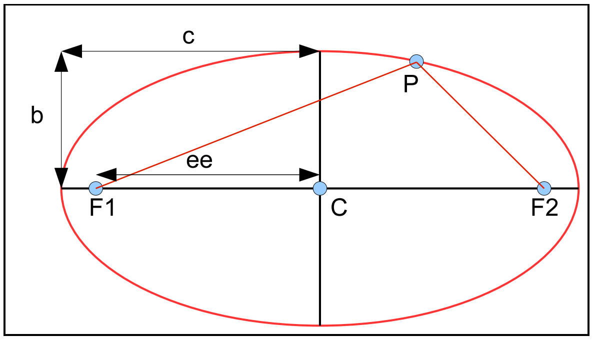

Figure 7.20: 2D plot of a spheroid with a = b

This imaging principle of elliptical surfaces can now be used for the mirror of the fiber coupler, but the parameters of the ellipsoid have to be found. The parameters are achieved in two steps: transform the system into a similar one in homogeneous media and determine the parameters for the ellipsoid in homogeneous media. Since the ellipsoid is rotational symmetric along its main axis, only the parameters b and c have to be determined ($a = b$).

7.4.4.1 Transformation of the system into homogeneous media

The elliptical reflector in this example is made of UV adhesive (NOA) with a refraction index of 1.56. In order to calculate the parameters for the elliptical surface, the setup from figure 7.16 has to be transformed into a setup with an homogeneous refraction index. In the following calculations, the center point of the mirror $\vec{C}_M$ represents two properties: the geometrical center of the mirror surface and the fact that it is the point where the optical axis, starting at the source, going in z-direction, hits the mirror surface. Following the meridional ray on the optical axis from the VCSEL through $\vec{C}_M$ into the fiber, the system can be simplified by ignoring the optical axis change caused by the reflection as shown in figure 7.21

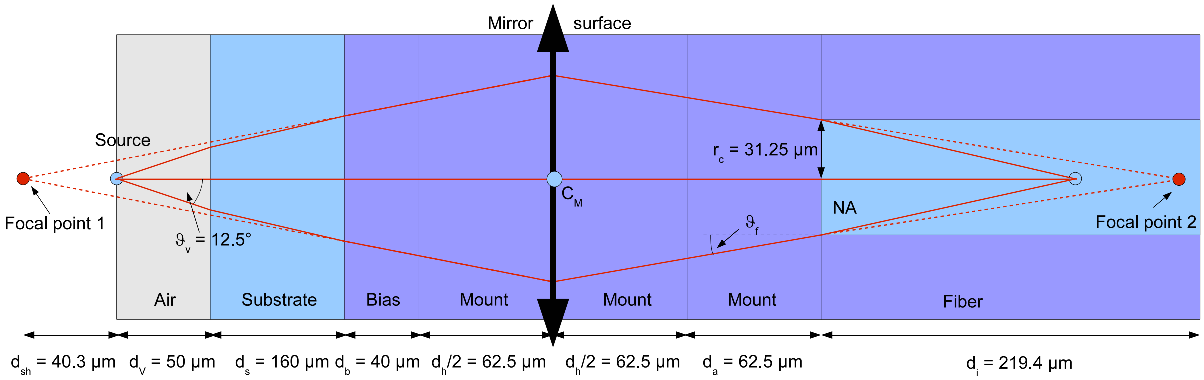

Figure 7.21: Adapted setup for the calculation of the focal points. The dotted line marks the rays going back from the mirror surface to find the virtual sources in a homogeneous media

Focal point 1 is found by tracing the outer ray from the VCSEL, going at 12.5° in the setup, onto the mirror surface and then tracing the ray back, but ignoring the index boundaries. The NA determines the maximum propagation angle which is still accepted by the fiber. Following a ray starting on the outer core diameter of the fiber into the fiber, going at ϑ_f, the second focal point is found. The results are also depicted in figure 7.21.

7.4.4.2 Determining the parameters for the ellipsoid

The focal points F_{o1} and F_{o2} determine the direction of the main axis of the ellipsoid with

$$\vec{s}_e = \frac{\vec{F}_{o2} - \vec{F}_{o1}}{\left|\vec{F}_{o2} - \vec{F}_{o1}\right|}, \tag{7.1}$$

the eccentricity

$$ee = \frac{\left|\vec{F}_{o2} - \vec{F}_{o2}\right|}{2}, \tag{7.2}$$

and with $\vec{s}_e$ and the optical axis $\vec{e}_z$, the rotation angle ϑ of the ellipsoid becomes

$$\vartheta = \arccos\left(\vec{s}_e \cdot \vec{e}_z\right). \tag{7.3}$$

Now, the ellipsoid center $\vec{C}$ is calculated

$$\vec{C} = \vec{F}_{o1} + \vec{s}_e \cdot ee \tag{7.4}$$

and moved into the origin by shifting the vectors

$$\vec{F}_1 = \vec{F}_{o1} - \vec{C}\ , \quad \vec{F}_2 = \vec{F}_{o2} - \vec{C}\ , \quad \vec{C}_M = \vec{C}_{Mo} - \vec{C}. \tag{7.5}$$

In the next step, the rotation matrix $\mathbf{D}$

$$\mathbf{D} = \begin{pmatrix} 1 & 0 & 0 \\ 0 & \cos\vartheta & -\sin\vartheta \\ 0 & \sin\vartheta & \cos\vartheta \end{pmatrix} \tag{7.6}$$

is used to rotate the ellipsoid onto the z-axis. $\vec{C}_M$ becomes the point $\vec{P}$ on the surface of the rotated ellipsoid by multiplication with the rotation matrix $\mathbf{D}$

$$\vec{P} = \mathbf{D} \cdot \vec{C}_M. \tag{7.7}$$

Since the ellipsoid is rotation symmetric with the axis $a = b$, the equation for the ellipsoid is reduced to a 2D elliptical problem. The equations of the ellipse

$$\frac{y^2}{b^2} + \frac{z^2}{c^2} - 1 = 0 \tag{7.8}$$

and

$$c^2 = b^2 + ee^2 \tag{7.9}$$

are now the basis to determine the two missing parameters b and c with the known point $\vec{P} = (x, y, z)$ on its surface

$$\begin{aligned} \frac{y^2}{b^2} + \frac{z^2}{c^2} - 1 &= 0 \\ b^2 &= c^2 - ee^2 \\ \Rightarrow \frac{y^2}{c^2 - ee^2} + \frac{z^2}{c^2} - 1 &= 0 \\ y^2c^2 + z^2\left(c^2 - ee^2\right) - c^2\left(c^2 - ee^2\right) &= 0 \\ c^4 - c^2\left(y^2 + z^2 + ee^2\right) + z^2ee^2 &= 0\ . \end{aligned} \tag{7.10}$$

The last equation becomes with $c' = c^2$ a standard quadratic equation delivering c. b is obtained by inserting c into equation 7.9. For the regarded VCSEL fiber setup, the ellipsoid parameters for the RayTracer are (all units in μm):

$$\begin{aligned} \vec{C} &= \begin{pmatrix} 0 \\ 172.2 \\ 136.1 \end{pmatrix} \\ a = b &= 246.5 \\ c &= 348.6 \\ \vartheta &= 44.3^\circ\ . \end{aligned}$$

Figure 7.22 shows the RayTrace results with these parameters.

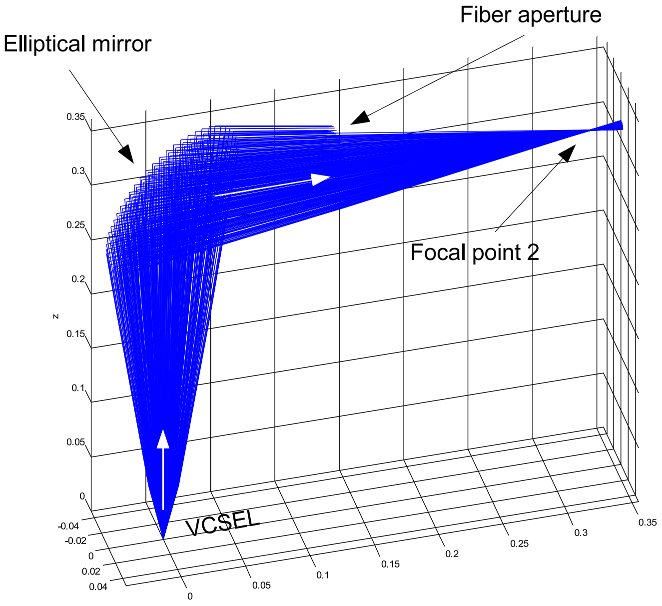

Figure 7.22: 3D plot of the RayTrace simulation for the integrated fiber coupler with an optimized elliptical mirror surface and a simulated coupling efficiency of 93%

The coupling efficiency increases to 93%. Around 4% are due to losses at index boundaries and the other 3% because the fiber is too close to the mirror and the outer rays cannot be focused into the fiber while keeping the NA limit of the fiber. Increasing the distance d_a by only 25 μm and calculating the ellipsoid again, brings the fiber coupler to the theoretical optimum of 96.4% for the regarded setup.

7.4.4.3 Summary

The previous section described the new concept of an integrated and compact fiber coupler using an optimal mirror surface which reaches the theoretical maximum coupling efficiency for the regarded setup of 96.4% ($d_a = d_a + 25\,\mu$m). The formulas for the calculation of the elliptical mirror surface and the parameters for the regarded setup are given. Additionally, the fiber coupler with an optimal mirror surface can be replicated using standard replication methods without increasing costs.

7.5 Demonstrator

After the concept and the optimization phase of the integrated fiber coupler in the previous paragraphs, the experimental proof has to follow. In order to be independent from the electronics and to test the optical performance only, the coupling efficiency between a fiber and a flip-chipped bottom emitting VCSEL, driven with the constant current of $I_v = 4.1\,$mA, is measured. The VCSEL from the company ULM Photonics, which now belongs to Philips, is a 5 Gbps VCSEL, emitting at 850 nm with a beam divergence $\vartheta = 12.5°$ half width $1/e^2$ and the optical power of 1 mW (at $I_v = 5\,$mA). As integrated fiber coupler, a version 3 fiber coupler with a mirror radius curvature of 175 μm was lithographically fabricated with double exposure and via soft lithography, replicated on a thin substrate with thickness $d_s = 160\,\mu$m, see figure 7.23.

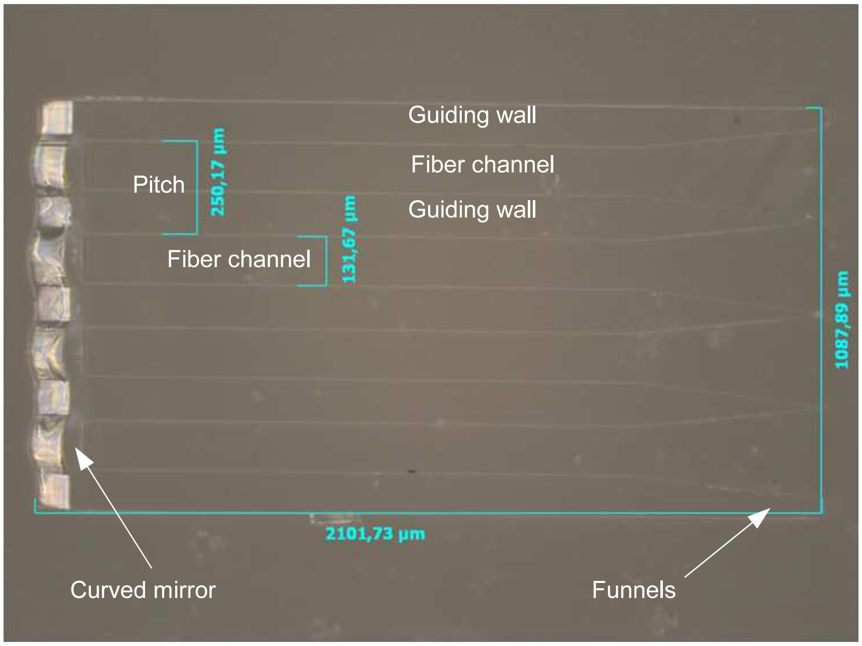

Figure 7.23: Integrated fiber coupler version 3 with four channels, fabricated with UV deep lithography and replicated in UV adhesive on a thin substrate

For the measurement, a multimode grin-fiber with a core radius of $r_f = 31.25\,\mu$m and a NA of 0.27 was inserted and fixed with UV adhesive. The VCSEL to fiber coupling efficiency measurement is described in the next paragraph followed by an analysis of the power budget for a complete transmission system, VCSEL-fiber-photodiode.

7.5.1 Coupling efficiency measurements

The measurements were realized with a Newport photometer and a detector head for 850 nm in three steps: reference measurement, direct fiber coupling measurement, and coupling measurement with the integrated fiber coupler version 3. The three steps are depicted in figure 7.24.

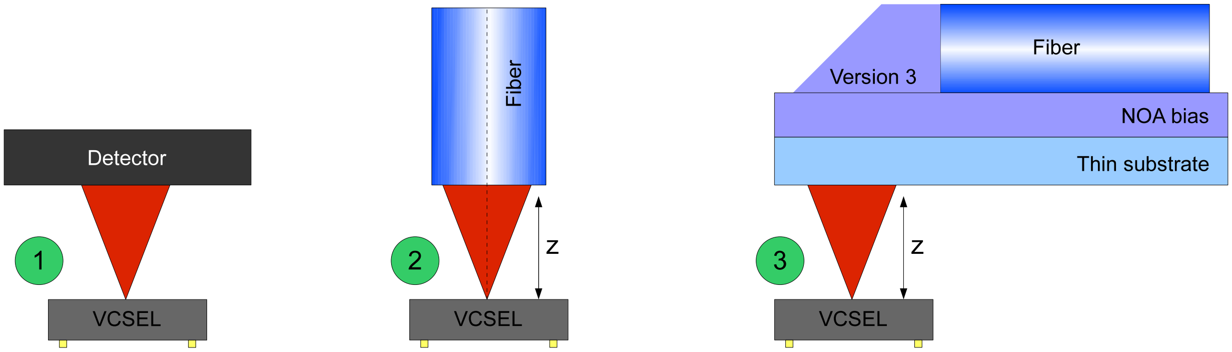

Figure 7.24: The three measurement steps: direct VCSEL measurement, direct fiber coupling measurement, and measurement with the integrated fiber coupler version 3

The optical power of the VCSEL at 4.1 mA is measured in step 1 as $P_0 = 580\,\mu$W. In step 2, the fiber was aligned above the VCSEL and the coupling efficiency measured every $50\,\mu$m. In order to compare the results with the simulation values from figure 7.10 (Gaussian point source coupled to fiber), the simulation results are scaled to meet the maximum measurement value, see figure 7.25.

The measurement shows a similar development of the values in comparison with the simulation. Possible errors are: misalignment of fiber and the optical axis defined by the VCSEL, and mismatch of the Gaussian beam profile of the VCSEL with the simulated beam characteristics.

For step 3, the fiber from step 2 was fixed in an integrated fiber coupler version 3 and the construct aligned with the VCSEL. In order to protect the fragile VCSEL, spacers were set next to the VCSEL, which proved later to be too large ($\approx 400\,\mu$m, increasing the gap between VCSEL and substrate from $50\,\mu$m to $250\,\mu$m). The measured optical power was 78 mW, which corresponds to a coupling efficiency of 14%. Since the simulation, including the bigger gap, showed a theoretical coupling efficiency of 27%, the first measurement was quite promising. Figure 7.26 and figure 7.27 show two photos from the measurement setup. The left one depicts the measurement of the direct VCSEL to fiber coupling, and the right one depicts the first measurement of the integrated fiber coupler with spacers.

A better way to protect the VCSEL is to embed it into a UV adhesive layer. In such a layer, the VCSEL is not only protected, but the beam divergence is also reduced due to the

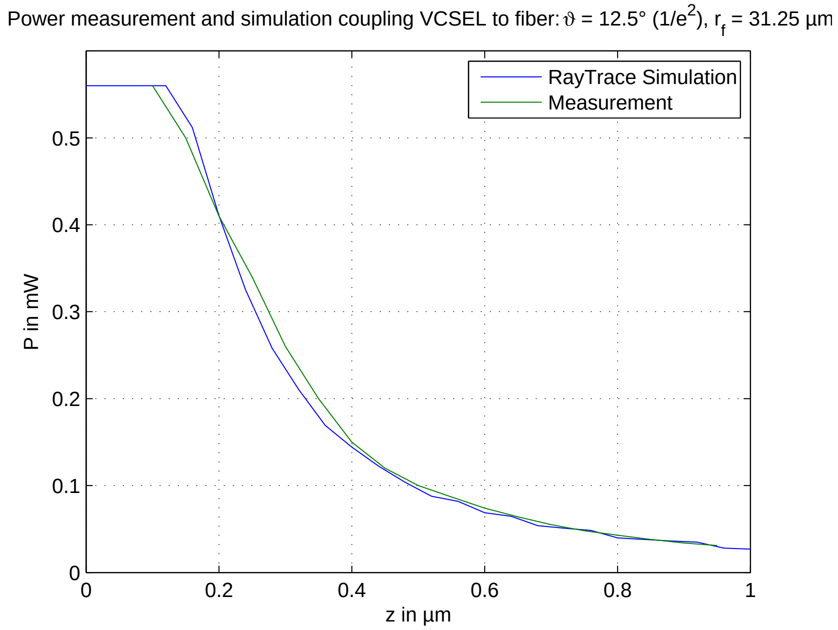

Figure 7.25: Step 2: direct VCSEL to fiber coupler measurement in comparison with the results from a RayTrace simulation ($\vartheta = 12.5°$, $r_c = 31.25\,\mu$m)

higher refraction index, increasing the coupling efficiency. Therefore, a very small droplet of UV adhesive was set directly next to the VCSEL and the surface tension forces of the liquid engulfed the VCSEL in a small UV-adhesive bubble. After curing, the VCSEL was embedded in a highly transparent layer. For the measurement, a second droplet of UV adhesive, as index matching between the VCSEL protection layer and the substrate with the fiber coupler on top, was added to prevent deflection effects of the protection layer surface, see figure 7.28.

With this improved setup, the coupling efficiency increased to 40%, giving a total optical power inside the fiber of 400 μW with the VCSEL driven at 5 mA ,and an optical power output of 1 mW. In comparison, the simulated coupling efficiency, assuming a gap distance of 50 μm filled with NOA, is 68.7%.

In the reflection measurement on SU-8 surfaces in chapter 2.2.7.2 on page 33, the mean value of the reflected energy within an aperture of r/σ was 58%. The combination of the simulated losses on the perfect reflecting mirror and the measured SU-8 surface reflection loss delivers $69\% \cdot 58\% = 40\%$, exactly the same result as the measured one.

7.5.2 Power budget

The transmit power of the source P_v, the attenuation introduced by the fiber A_f, and the minimum receive power P_{pd} of the photodiode determine the power budget, which is often stated in dB. The attenuation of a graded-index fiber with a core radius of $r_c = 31.25\,\mu$m is typically in the range of 3 dB/km. A 100 m fiber will introduce an

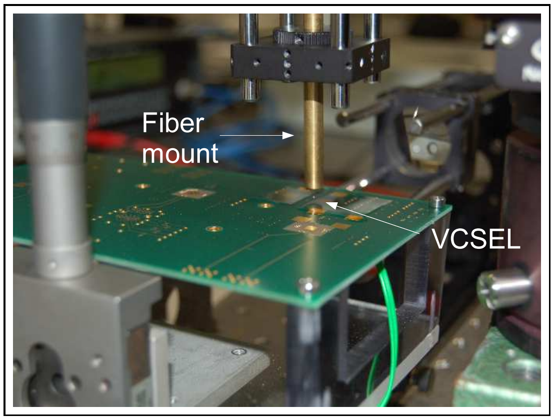

Figure 7.26: Step 2: measurement setup for direct VCSEL to fiber coupling

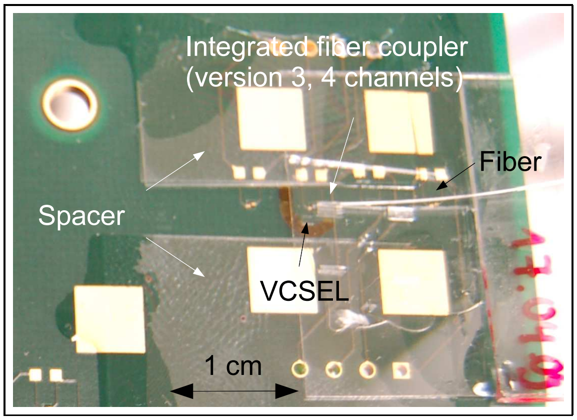

Figure 7.27: Step 3: first measurement of the integrated fiber coupler version 3 with spacers

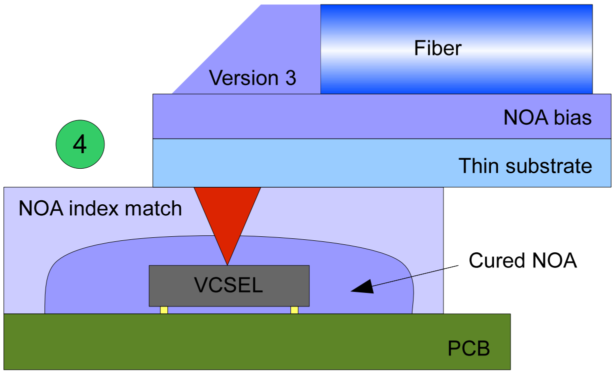

Figure 7.28: Step 3: measurement setup with VCSEL in NOA protection layer and NOA index matching

attenuation of $A_f = 0.3\,\mathrm{dB}$. With $P_v = 1\,\mathrm{mW}$ and $P_{pd} = 10\,\mu\mathrm{W}$ the power budget for the transmission becomes

$$P_{pb} = 10\log_{10}\left(\frac{P_v}{P_{pd}}\right) - A_f = 19.7\,\mathrm{dB}. \tag{7.11}$$

The coupling efficiency, VCSEL to fiber, for the version 3 fiber coupler was simulated with 68.7% ($-1.63\,\mathrm{dB}$), and measured with 40% ($-3.98\,\mathrm{dB}$). The results can also be interpreted as one attenuation coming from the setup with $-1.63\,\mathrm{dB}$ and a second one, coming from misalignment and the mirror surface $-2.35\,\mathrm{dB}$.

The coupling efficiency for the end part of the transmission (fiber to photodiode) has yet to be determined.

For the simulation, the setup shown in figure 7.17 on page 112 is used again, this time with the light coming from the fiber and the VCSEL being replaced by a photodiode with variable aperture radius. Since a larger photodiode means higher coupling efficiency but lower bandwidth, the system designer has to decide which property is more important. Figure 7.29 depicts the 3D plot of the setup and figure 7.30 the simulated coupling efficiency between fiber and photodiode, with the RayTrace configuration: area Gaussian source with 4 rings in 'mixed'-mode.

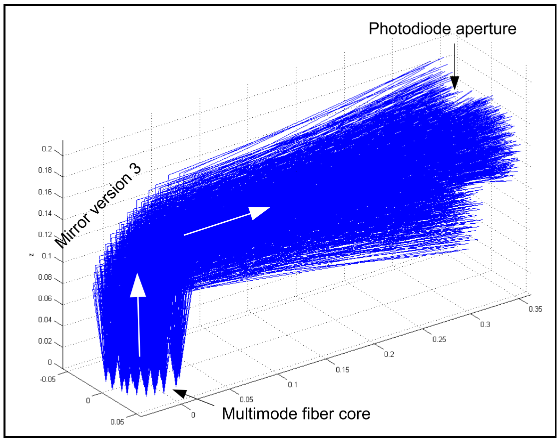

Figure 7.29: RayTrace 3D plot of the coupling between multimode fiber with $r_c = 31.25\,\mu$m and a photodiode (coupler version 3)

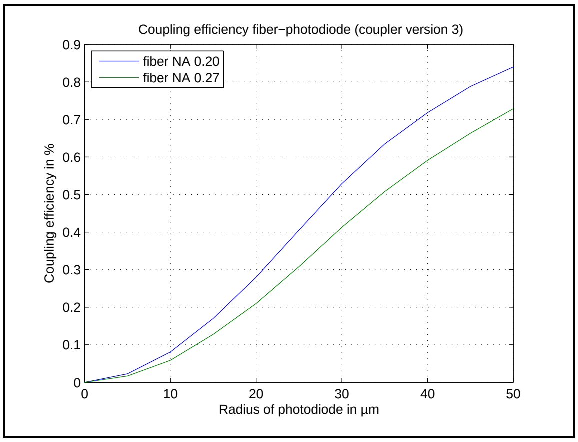

Figure 7.30: Coupling efficiency between fiber and photodiode for the setup in figure 7.17 on page 112

Fibers with higher NA increase the coupling efficiency between VCSEL and fiber but decrease the coupling efficiency between fiber and photodiode at the same time. This becomes more critical with smaller photodiodes. Choosing a photodiode with $r_{pd} = 50\,\mu$m and a fiber with $NA = 0.27$, the simulated coupling efficiency becomes 72% or $-1.43\,$dB.

Table 7.1 lists the power budget and attenuations for this measurement setup with an approximation of the optical performance of the demonstrator. The attenuations caused by mirror and alignment are calculated from the relation between measured efficiency and simulated efficiency, assuming a correct implementation of the beam characteristics. The attenuations coming from the coupling between fiber and photodiode could only be simulated; the estimation of the additional losses due to misalignment and mirror surface ($-3\,$dB) are based on the measurements for the VCSEL to fiber coupling ($-2.35\,$dB).

The remaining power budget of 11.11 dB leaves a high margin for additional losses introduced by misalignment and tolerances in large-scale production.

The potential of this very compact integrated fiber coupling device with high coupling efficiency in the field of active optical cables is discussed in the following paragraph.

Parameter	Symbol	Unit	Value
VCSEL optical power	P_v	μW	960
PD minimum receive power	P_{pd}	μW	10
Fiber attenuation 100 m	A_f	dB	-0.3
VCSEL-fiber setup attenuation (simulated)	A_{s1}	dB	-1.63
VCSEL-fiber mirror and alignment losses	A_{m1}	dB	-2.35
Fiber-PD setup attenuation (simulated)	A_{s2}	dB	-1.43
Fiber-PD mirror and alignment losses (estimated)	A_{m2}	dB	-3.0
Power budget	P_{pb}	dB	11.11

Table 7.1: Power budget and attenuations for the demonstrator using the integrated fiber coupler version 3

7.6 Active optical cables

The market for active optical cables (AOC) is primarily based on the demands of high performance computing. Reaching a transmission speed of 10 Gbps while keeping the cables long enough for the application demands, made people think about alternative connection technologies. Their first choice was to go from copper conductors to fibers but this came with drawbacks. Fiber technologies require new network cards with optical interfaces and trained specialists to handle all issues around fibers such as eye safety, cleaning, splicing and other connection problems.

AOC encapsulate the transceiver and optical connection inside the connector, dismissing all drawbacks of pure fiber connects, while keeping all benefits of optical transmission. Intel was the first company to supply the market with this new kind of cable and established them within the InfiniBand specification. This allows to remove the old copper cables and simply put in the new AOC, gaining all optical benefits without any additional complications. AOC reduce the weight and size in comparison with copper cables by more than 80% while increasing the possible transmission length from 10 m to several hundred meters. Additionally, the old problem that the interconnect is slower than the electronics is now inverted, making any advances in electronics to drive the light sources faster, automatically increasing the transmission speed of the cable. End of June 2009, the company Finisar announced an AOC with 12 channels at 10 Gbps for InfiniBand and 100 Gigabit applications.

A market study “Active Optical Cables Market Analysis 2009” [28] predicts a growth for this segment from the present-year level of \$100 million to over \$1.1 billion in 2010, and then up to over \$2.6 billion by 2013. This indicates the high demand on low priced, highly efficient coupling methods.

In the previous paragraphs, this thesis presented an integrated and compact fiber coupler designed exactly for this purpose.

While the demands for large-scale production are already met with the replication techniques of soft lithography, further improvement in the production process can decrease the costs even more. Two basic assembly sketches follow.

The transceiver module consists of a PCB with electronics for the electro-optical conversion and a basic mount on which the fibers will later be fixed for strain-relief. A simple way to integrate the optics is to first finish the complete electronics on the board, flip-chipping the VCSEL, and to run a basic power test. If everything is working, the optics are integrated in the next step. A thin layer of UV adhesive is applied onto the VCSELs and the optical coupling module, which consists of a thin substrate with replicated integrated fiber couplers on it, is aligned above them. After a short UV flash for curing, the module is fixed and the fiber bundle can be inserted in one step, since the pitch of the coupler is exactly 250 μm matching the pitch of fiber bundles. Now the fibers have to be fixed and the complete assembly can be encapsulated.

It would be even more beneficial, if the substrate for the integrated fiber couplers would become dispensable by replicating the integrated fiber couplers directly on top of the VCSELs. This could be achieved with a high precision flip-chip machine, which already flip-chipped the VCSEL and exactly knows, where the VCSELs are. By changing the head of the flip-chip machine with a PDMS stamp, the same machine can be used to replicate the structures directly. A second advantage of this direct method is an increasing coupling efficiency due to the reduced distance between VCSEL and fiber coupler, since the substrate layer disappears. Figure 7.31 depicts how such a design of an optical module for a 6 channel bidirectional AOC cable would look like.

The transmission speed only depends on the electronics, which reached a speed of 12.5 Gbps per channel in 2009 with even higher rates being announced. The presented very compact integrated fiber coupler allows designs with a density of four channel per millimeter per layer. Since the height of such an assembly is < 2 mm one might think about integrating more than one layer into the plug. Assuming a 2 layer design with a 1 cm optical module containing 20 bidirectional links with 10 Gbps each, the transmission speed of this cable would be 400 Gbps bidirectional at a cable size of ≈ 10 mm x1 mm.

7.7 Conclusion

The market for cables with optical transmission is growing rapidly, not only the long distance area of telecommunications, but also at short distances. Active optical cables are perfectly suited to satisfy the market demands of a cable that can be handled like a

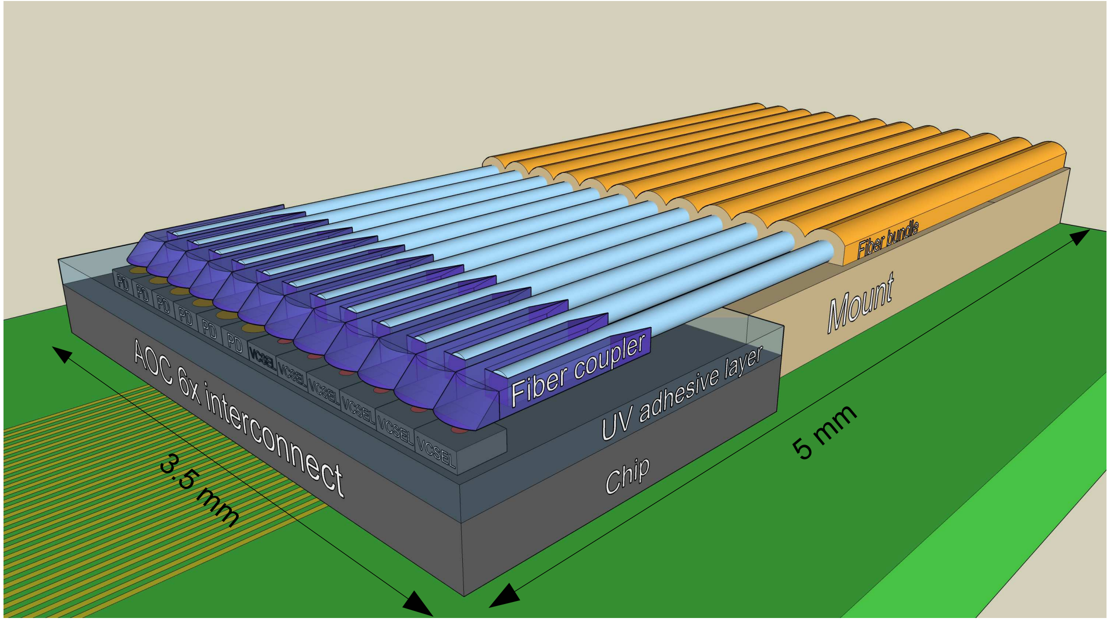

Figure 7.31: Design of the optical module of an AOC with 6 bidirectional channels and the integrated fiber coupler version 3

standard copper cable without thinking about optics, but providing all benefits of optical transmission. The application area is not limited to high performance computing and special scenarios like in high energy physics but will grow into shorter distances and into the consumer market once the costs of the optical assembly are reduced.

The presented concept of an integrated fiber coupler with a focusing mirror is very well suited for exactly this purpose, offering high coupling efficiencies, very compact designs, and standardized replication methods. The measured coupling efficiency of 40% with an integrated fiber coupler version 3 on a substrate can even be improved; by optimizing the mirror surface as presented with the perfect mirror design in the previous chapter, or by reducing the distance between VCSEL and fiber. The latter can be achieved with an adapted replication method rendering the carrier substrate unnecessary. The coupling efficiency using the perfect mirror surface increases to the theoretical maximum of 96.4%, all losses being due to refraction index boundaries which can be further decreased by index matching.

The master for the demonstrator of the integrated fiber coupler was produced with UV deep lithography and replicated with soft lithography.

Chapter 8

Parallel microscopy for the ViroQuant project

The ViroQuant project is established under the roof of the BioQuant project as part of FORSYS (Forschungseinheiten der Systembiologie). As a project in the field of systems biology, it focuses on the systematic and quantitative investigation of complex cellular networks that are essential for viral infections. As one part of the project, biologists define and model gene functions on a genome-wide scale using high-throughput fluorescence-microscopy [42]. Besides a high spatial resolution, the imaging speed, especially in time-lapse imaging [41], is an important factor.

A significant increase in scan speed can be achieved by parallelization. The parallelism of microscopy is limited by the size of one imaging system and the ratio between lens diameter (D_L) and the field of view (FoV) of the objectives. Thus miniaturization offers the possibility of a higher degree of parallelism. Furthermore, the aberrations scale down with the lens size (see Lohmann [35]).

In the following paragraphs, parallel microscopy is investigated and macro objectives, micro lenses, and GRIN-rod lens systems are compared. The latter will be analyzed in more detail. Since the excitation light has to be separated from the imaging light in fluorescence microscopy, a beam splitter is necessary. The chapter is closed with an assembly suggestion for a parallel microscope using GRIN-rods, an integrated beam splitter, and compact mounts fabricated with UV deep lithography.

8.1 High-throughput parallel microscopy

It is clear that the speed of microscopy can be increased by reducing the number of mechanical scans over the substrate. Assuming that the mechanical scans occur along the y-axis, one distinguishes between a parallelization in x-direction and in y-direction. Figure 8.1 depicts the important parameters for a parallelization in x-direction.

At the beginning, only the parallelization in the x-direction is considered, since the y-direction requires only a replication of the hardware. An important factor for parallel

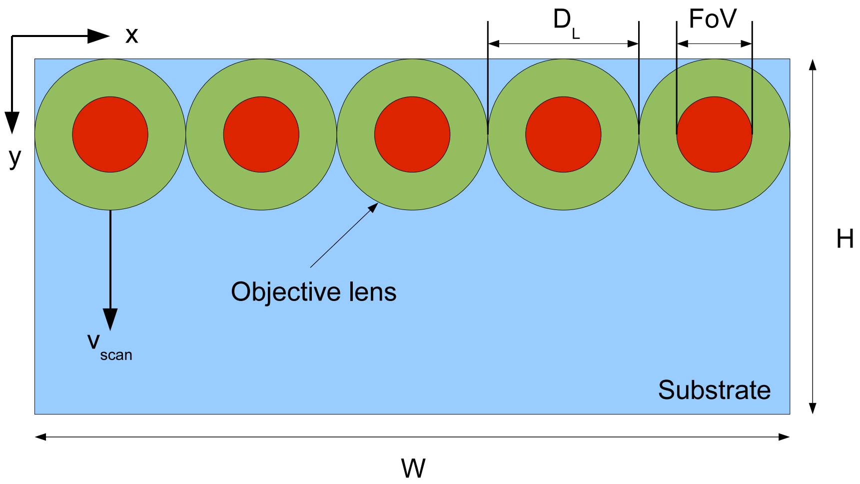

Figure 8.1: Important paramters for a microscopy parallelization in x-direction

microscopy is the ratio between FoV and D_L. The maximum degree of parallelism can be achieved ideally if $FoV/D_L = 1$. The ratio is limited geometrically by the desired magnification and in quality by aberrations of the lens system.

8.1.1 Important parameters for parallel microscopy

The maximum degree of parallelism in x-direction N_x is determined by

$$N_x = \frac{W}{D_L} \tag{8.1}$$

and the field of view can be described with the relation factor α by

$$FoV = \alpha \cdot D_L. \tag{8.2}$$

With N_x and FoV the minimum number of scans N_{scans} on a substrate with the width W results in

$$\begin{aligned} N_{scans} &= \frac{W}{FoV}\frac{1}{N_x} \\ &= \frac{W}{FoV}\frac{D_L}{W} \\ &= \frac{D_L}{FoV}. \end{aligned} \tag{8.3}$$

Finally, the time needed to scan a whole substrate is determined by

$$T = \frac{D_L}{FoV} \cdot \frac{1}{N_y} \cdot \frac{H}{v_{scan}}. \tag{8.4}$$

Equation 8.4 points out three parameters to further optimize the scanning speed of a parallelized microscope in x-direction: decrease the ratio D_L/FoV, increase the parallelization in y-direction, and increase the scanning speed. The ratio D_L/FoV is limited by the performance requirements on the optical design. A larger FoV, and keeping D_L constant increases the complexity of the design. The parallelization in y-direction equally depends on the size of the lens D_L and also on the size of the electronics, while the scanning speed depends on the detector's quantum efficiency and the fluorescence properties. Since lens aberrations scale down with the lens diameter, reducing the complexity of the optic design for a high D_L/FoV ratio and the parallelization in y-direction also increases with smaller lens sizes, these results suggest to focus on designs with miniaturized lenses in order to speed up the system.

Another time consuming factor has to be mentioned here: the time for focusing. In an examination of the system the biologists were using, most of the scanning time was spent on finding the correct focus because their substrates were not flat. This problem is approached in two ways at the moment: measurement of the surface profile using deflectometry (Slogsnat et al. [48]) in order to calculate the correct working distance for each spot, and the development of an optical flat substrate.

At the time, the optical flat substrate is developed by a group from the ViroQuant project. The microwell cell array contains 9216 physically separated microwells [25], see figure 8.2, with a flat surface. A spot diameter of 400 μm and a pitch of 750 μm in both directions is planned.

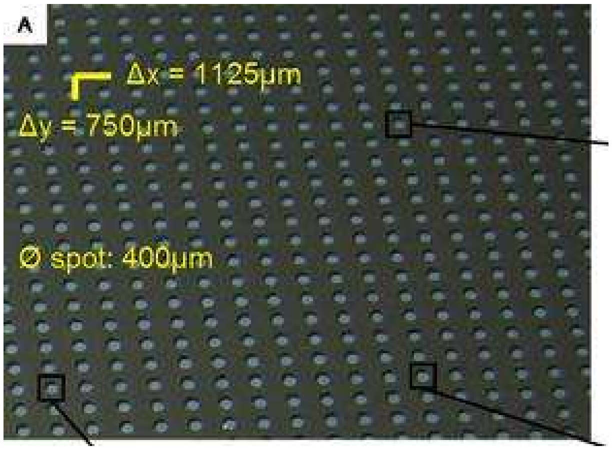

Figure 8.2: Microwell cell array with a flat surface and 9216 physically separated microwells, the new version shall reach $\Delta x = \Delta y = 750\,\mu$m (image source: ViroQuant)

In the following paragraphs, four different approaches for high throughput parallel scanning microscopy systems are analyzed and compared: a classical approach, an approach with miniaturized lenses, one with micro lens arrays, and an approach with GRIN lenses.

8.1.2 Parallelization with classical objectives

Optic design is a science and sometimes an art. Many years of development were invested in order to produce the high performance objectives for fluorescence microscopy offered by different companies. Therefore the first approach of parallel microscopy described here, uses commercially available objectives. The advantages are that these objectives are already optimized for fluorescence application and are diffraction limited going from UV to the near infrared. A parallelized system of commercially available objectives is developed by the PhD student Lars Lehmann from the ViroQuant group. The system consists of Olympus UPLSAPO 10X2 objectives with a numerical aperture of 0.4, a lens diameter D_L of 28 mm, FoV of 2600 μm, and a parallelization factor $N_x = 5$. The challenges in the development are: compact mechanics, alignment and assembly, and the integration of suitable cameras.

8.1.3 Parallelization with miniaturized lenses

While classical optic design with glass lenses is well understood, the design of systems using micro lenses and replication material is still a research field. A leading company in the field of miniaturized parallel microscopy is d.metrix. They assembled a system with four miniaturized polymer lenses, including two aspheric surfaces, covering a field of view of 250 μm. With a numerical aperture of 0.7, and a ratio of $D_L/FoV \approx 8$, the diffraction limited system shows the potential of miniaturized designs. Their optic design is depicted in figure 8.3.

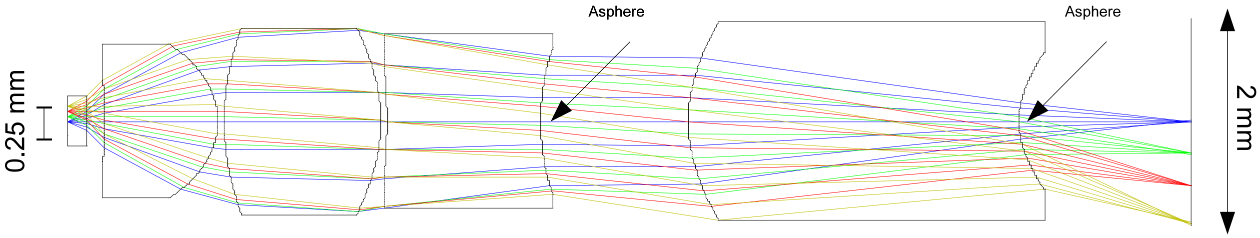

Figure 8.3: D.metrix optic design for miniaturized parallel microscopy $D_L/FoV = 8$

These miniaturized objectives are assembled in a 2D array in a kind that one scan covers a complete area in one step. Since the chromatic aberration is only slightly corrected by using two different polymers (COC and Polystyrol), the design is limited to a narrow wavelength bandwidth.

8.1.4 Parallelization with micro lens arrays

Further reduction of the size leads to the domain of micro lenses. They exist in many different sizes, typically going from $D_L = 100\,\mu$m to $D_L = 1000\,\mu$m. While in the last two designs, both surfaces of a lens were used to minimize the aberrations, one side of micro lenses is often planar. One of their advantages is that they are produced with high accuracy in arrays, called micro lens arrays, reducing the alignment complexity in the subsequent assembly, since only one substrate has to be aligned instead of many single lenses.

Due to the size of the micro lenses in comparison with the required $FoV = 400\,\mu$m, it becomes obvious that more than one scan is necessary to cover one spot. The following system concept was developed to show a minimalistic design using only three lenses with planar surfaces and a magnification equal to the ratio D_L/FoV. The FoV was set slightly larger than half the size of the required FoV, in order to be able to image one spot with two scans. In addition to the two previous designs, a beam splitter is integrated into the design, symbolized by a square block of material. The beam splitter will later be used to couple the stimulating light into the system. The design is depicted in figure 8.4.

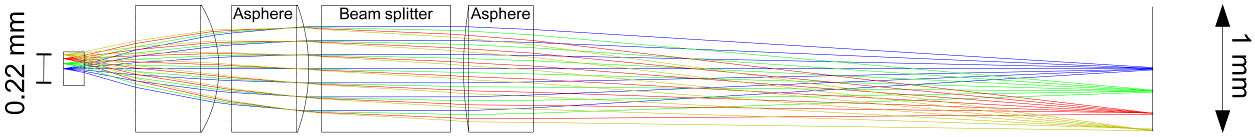

Figure 8.4: Optic design with 3 micro lenses and a beam splitter, $D_L/FoV = 5$, $NA = 0.28$

With 2 aspheres, 1 wavelength, 1 lens material, and a reduced numerical aperture of 0.28, the design is almost diffraction limited across the whole FoV of $220\,\mu$m (see spot diagram in figure 8.5) with a lens diameter of only 1 mm. Each lens consists of $500\,\mu$m thick silica substrate with a replicated lens on top of it.

The charm of such a system lies within the greatly reduced cost in large-scale production. Once a master is fabricated, the system consists of low cost replicated micro lens arrays on planar substrates. The complex alignment of single lenses to form objectives and the subsequent assembly of objectives to parallel systems is reduced to the alignment of a few layers.

8.1.5 Parallelization with GRIN rod lenses

GRIN rod lenses focus light by their gradually changing refraction index. They are commercially available and diffraction limited up to a numerical aperture of 0.5. The gradient index is typically radial symmetric along the optical axis with the highest value in the middle, decreasing in a sech-like profile with increasing r. The material that is diffused into the glass body defines the important parameters of a GRIN lens such as pitch and absorption. Silver and lithium are often used for the diffusion. While silver allows higher gradients, the absorption below 450 nm increases rapidly. GRIN lenses with lithium show an inverse behavior, low absorption till 350 nm but also lower gradients increasing the rod's pitch size. The transmission spectra for GRIN rod lenses with silver and lithium are shown in figures 8.6 and 8.7.

Since lithium rods are not suited for microscopy due to their large pitches, which

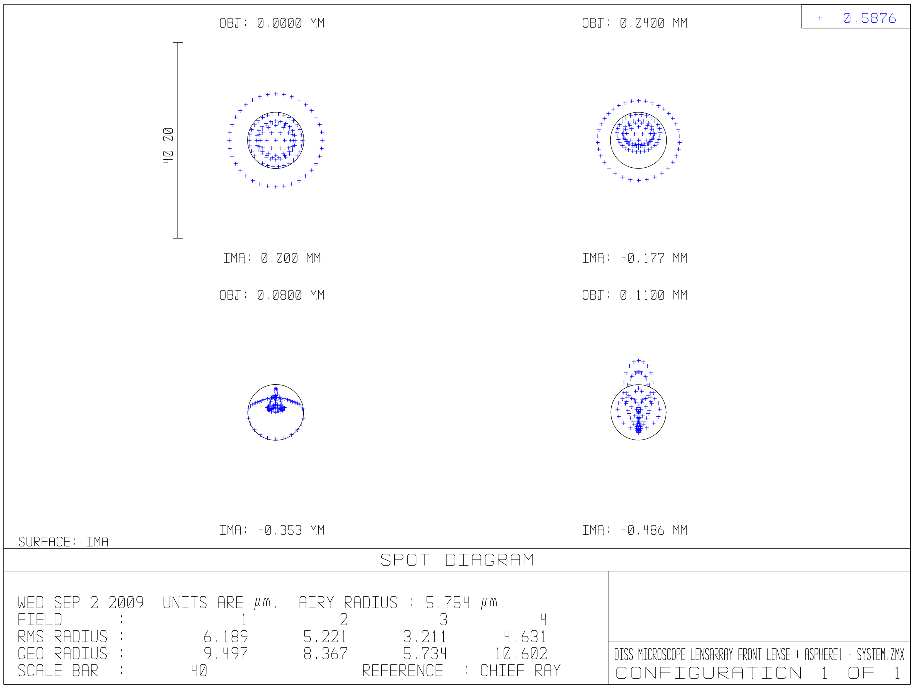

Figure 8.5: Spot diagram of the micro lens array design, $NA = 0.28$, magnification 4.6

corresponds to low numerical apertures for a fixed lens diameter, only silver rods are regarded in the following.

8.1.5.1 The optical design

The optical design of the GRIN rod system is based on the required FoV of 400 μm and a numerical aperture of 0.3. Since the GRIN rods have to be mounted on substrates, 500 μm SiO_2 mount substrates are added in the design, see figure 8.8.

Which side of the lens the substrates are added on has a huge influence on the later performance. For the first lens, the substrate is better placed behind the lens; if not, the outer rays propagate closer to the boundaries of the lens, increasing the aberrations. For the second lens, the substrate is again better placed behind the lens; changing the order of lens and glass increases the spot sizes by more than a factor of two.

The ideal gradient index profile of a GRIN rod lens is the sech-profile, considering the imaging from the front surface to the back surface of the GRIN rod lens. This profile is often approximated with a Taylor series which is cut off after the 4th order term:

$$n\left(r\right) = n_0 + nr_2 \cdot r^2 + nr_4 \cdot r^4 \tag{8.5}$$

In order to achieve a diffraction limited design for a large field of view, the parameter nr_4 of the lenses had to be optimized as well. It was changed for the first lens from 0.0044 (value from GRINTECH) to 0.001736 and for the second lens to 0.009512. The spot diagrams without and with optimized nr_4 are shown in the figures 8.9 and 8.10 .

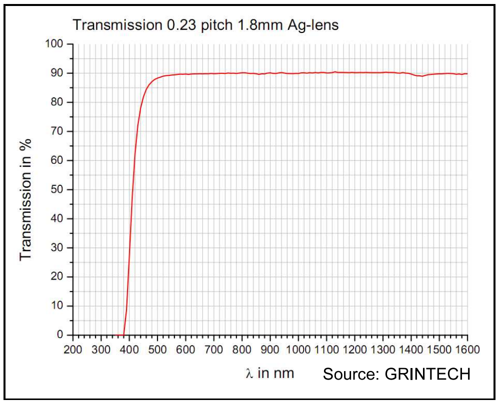

Figure 8.6: Transmission spectrum for GRIN rods with silver

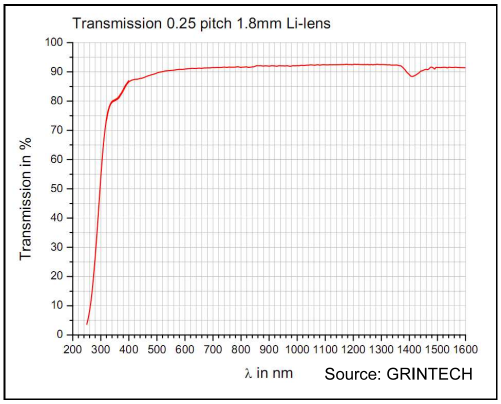

Figure 8.7: Transmission spectrum for GRIN rods with lithium

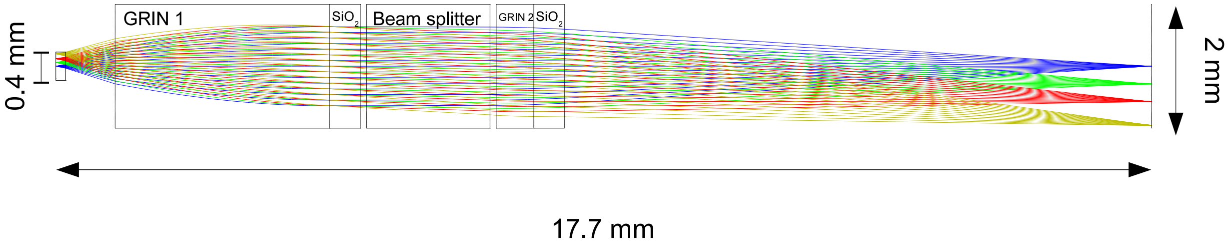

Figure 8.8: GRIN rod lens design with beam splitter and substrates ($D_L/FoV = 5$, $NA = 0.3$, magnification 4.8)

8.1.5.2 Chromatic aberrations

For most of the applications in microscopy, it is essential to correct the objectives for a specific wavelength spectrum. Due to the dispersion of optical materials, the refractive index for blue light is higher than for red light. Therefore in imaging, the focal length for blue light is shorter than for longer wavelengths. The variation of paraxial focal length depending on wavelength is called chromatic longitudinal aberrations.

The chromatic focal shift describes the position variation of the optimal focus for different wavelengths. Good chromatic aberration correction results in a constant focus position while no correction results in a varying position. The focal shift for the described GRIN system is depicted in figure 8.11.

The diagram shows the strong chromatic aberrations of the GRIN system in terms of chromatic focal shift. The acceptable wavelength spectrum is smaller than 10 nm, limiting the design to a very narrow spectrum.

One possible improvement of the system is the implementation of a diffractive optical element in order to minimize the chromatic aberrations.

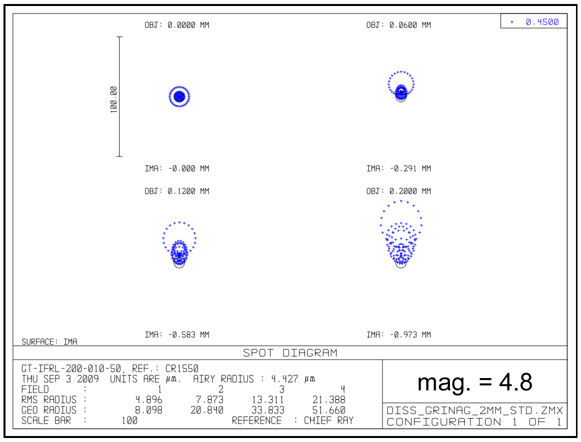

Figure 8.9: Spot diagram of the optic design with commercial available GRIN rod lenses, ($D_L/FoV = 5$, $NA = 0.3$, magnification 4.8)

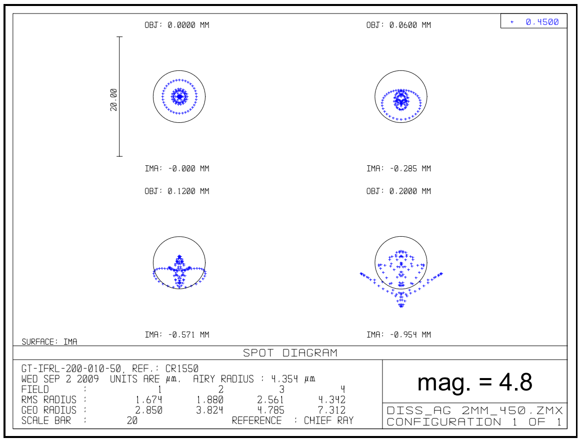

Figure 8.10: Spot diagram of the optic design with optimized (nr_4) GRIN rod lenses, ($D_L/FoV = 5$, $NA = 0.3$, magnification 4.8)

8.1.6 Comparison

Before the systems are compared, a few words about balanced optic designs in relation to the electronics are needed. The performance of the system not only depends on the optics, but also on the electronics, especially on the camera and its pixel size. Even if the optics are diffraction limited and image a 1 μm point with magnification 5 perfectly on a 5 μm spot, the camera still has to sample it according to Nyquist with at least two pixel to avoid sampling errors. The pixel size would have to be $< 2.5\,\mu$m. At the time, available cameras' or sensors' minimum pixel sizes are $> 4\,\mu$m. Therefore, a minimum magnification of 8 is needed to avoid resolution loss due to too large camera pixel.

The comparison for high-throughput parallel microscopes in table 8.1 does not include considerations about the electronics and focuses only on the performance of the optics. The important number for the ViroQuant project is 'Scans to cover spots'. This number accounts for the dimensions of the microwell cell arrays which will be used in the ViroQuant project. Since the spot diameter is 400 μm and the pitch is 750 μm, the optics do not have to scan the complete substrate but only the spots. The number 'Scans to cover spots' specifies the number of scans needed to scan all spots on a microwell cell array with a microscope parallelized in x-direction (N_x maximal). The number is equal to the y-parallelization N_y required to scan the substrate in one pass.

The chromatic aberration correction is specified with two wavelengths for the micro lens array and GRIN rod lens system. The reason is the integrated beam splitter for coupling the excitation light into the system. Since the light path for the simulated light is separated, it can be optimized individually.

The comparison shows that the GRIN rod lens system covers all spots with a degree of parallelization of only three in y-direction, allowing the most compact design. The

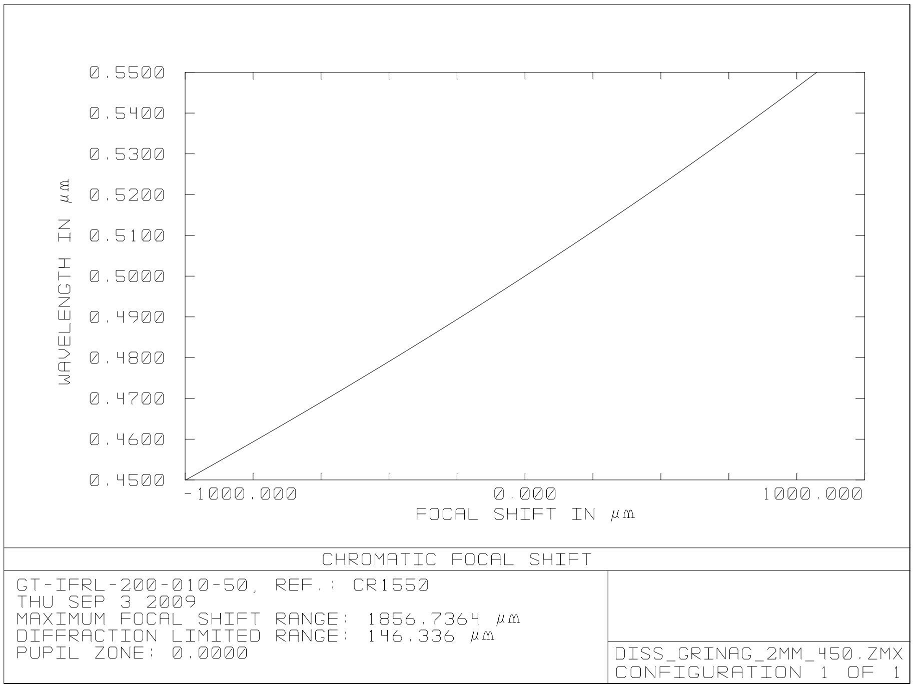

Figure 8.11: Chromatic focal shift of the GRIN system

	Classic parallel	Mini. lenses	Micro lenses	GRIN rod lenses
Magnification	10	7	4.6	4.8
NA	0.4	0.7	0.28	0.3
Object resolution	$\approx 1\,\mu$m	$\approx 1\,\mu$m	$\approx 1\,\mu$m	$\approx 1\,\mu$m
Chr. aber. corr.	yes	minor	2 wavelengths	2 wavelengths
Lens diameter	28 mm	2 mm	1 mm	2 mm
Field of view	2600 μm	250 μm	220 μm	400 μm
Scans for total plane	12	8	5	5
Scans to cover spots	12	6	4	3

Table 8.1: Comparison of the important parameters for a parallel microscope design: classical system, miniaturized lenses, micro lens arrays, and GRIN rod lens system

following paragraphs will describe how such a system would look like and how it would be assembled.

8.2 Concept and assembly of a parallelized microscope using GRIN rod lenses

The GRIN rod lens design consists of two GRIN rod lenses mounted on substrates with a beam splitter in between, as depicted in figure 8.12.

The beam splitter, sensitive to wavelengths, couples the excitation light into the objective and also separates the reflected excitation light from the imaging light. Since the excitation wavelength is shorter than the emission wavelength, the beam splitter is reflective for wavelength up to a certain limit and transparent for wavelengths above. The assembly is described in the next paragraph.

8.2.1 Assembly

The assembly is done in three steps: fabrication of substrates with ring mounts for the GRIN rods, insertion and fixation of the GRIN rods, alignment of the two GRIN rod layers and the beam splitter. UV deep lithography is used to fabricate the ring mounts for the GRIN rods. According to the dimensions of the ViroQuant microwell cell array, the smallest pitch of the lenses in x-direction is $3 \times 750\,\mu\text{m} = 2250\,\mu\text{m}$. The pitch in y-direction depends on the size of the illumination source and the electronics, and might be around 6 mm. Three parallelizations in y-direction are needed to scan the substrate in one turn, each line shifted by $750\,\mu\text{m}$. The optical assembly with $N_x = 4$ and $N_y = 3$ is illustrated in figure 8.13.

After the fabrication of the ring mounts on a substrate, the GRIN rod lenses are inserted and fixed. Due to the high precision of the lithographic fabricated mounts, the GRIN rods of this plane are aligned automatically. The beam splitter and the two substrates with GRIN rods are the three layers which have to be aligned and fixed for the final assembly. The result is a compact three layer stack, including all passive optical components in one block.

8.2.2 Beam splitter

The beam splitter master was fabricated with micro precision machining by LFM in Bremen. The sample is 20 mm long and due to the diameter of the lenses 2 mm high (see concept in figure 8.14). Using direct UV replication, the master was replicated in UV adhesive. The fabrication is described in more detail in chapter 2.3 on page 37 and the replication in chapter 3.1 on page 42.

Reflective coatings on the beam splitter surfaces apply the functionality to be transparent for the imaging light and to be reflective for the excitation light (see figure 8.15). While reflective coatings on glass and metal are state of the art, reflective coatings on polymers

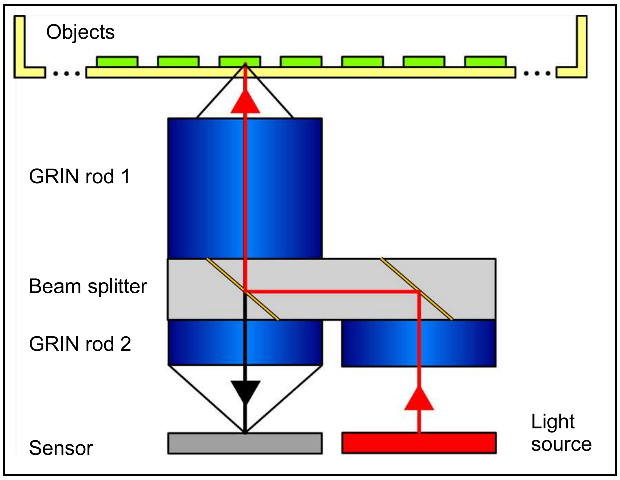

Figure 8.12: GRIN rod lens system design with 2 lenses and 1 beam splitter

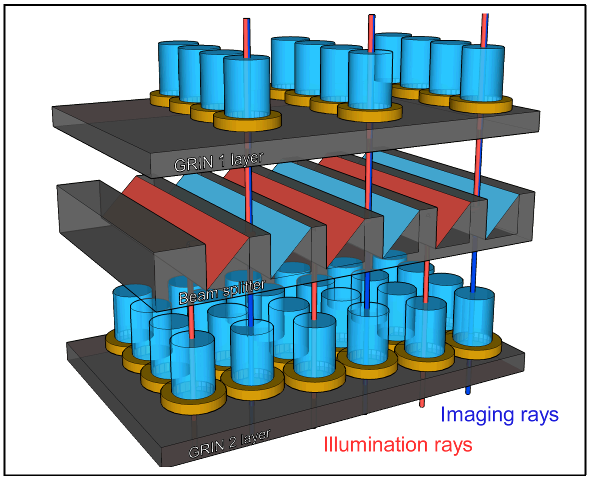

Figure 8.13: Planar assembly of a parallel microscope using GRIN rod lenses and a beam splitter

are not (Munzert et al. [40]). Munzert et al. describe in their paper how polymers are coated with high reflective layers using the properties of the polymer. Once the beam splitter is coated, the slanted grooves are filled with the same material the beam splitter was made of, perfectly matching all indices and making the beam splitter a planar block.

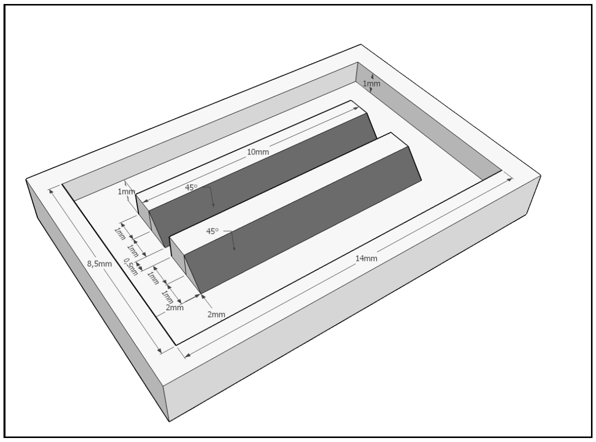

Figure 8.14: Technical draw for the master of the beam splitter

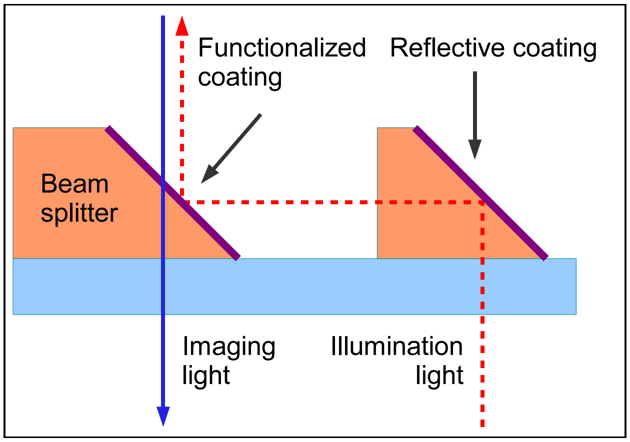

Figure 8.15: Functionality of the beam splitter: reflective for illumination light, transparent for imaging light

In summary, the production and replication for the beam splitter was successful. While the functionality using coatings was demonstrated by other groups, it has yet to be demonstrated for the replicated beam splitter.

8.3 Accuracy of paraxial optics for GRIN rod lenses

Commercial GRIN rod lenses, as found in catalogs, are mostly described by paraxial formula. In the following, the accuracy of this description is compared to a more rigorous calculation using the software Zemax. Three applications using one GRIN rod lens are compared: imaging system, coupling system where a point source in front of the GRIN is imaged on its back surface, and the collimator system which transforms a point source in front of the GRIN into parallel light.

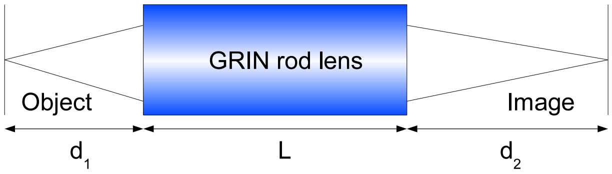

Figure 8.16: Schematic draw of an imaging system using one GRIN rod lens

8.3.1 Paraxial calculation

In paraxial optics, systems can be described by ABCD matrices. A simple imaging system consists of two propagation matrices and one matrix describing the optical system. If the optical system consists of one GRIN rod lens with the index profile

$$n\,(r) = n_0 \; sech(g \cdot r) \tag{8.6}$$

with the approximation

$$n\,(r) \approx n_0 \left(1 - \frac{1}{2}\, g^2\, r^2 + \frac{4}{25}\, g^4\, r^4\right) \tag{8.7}$$

and only regarding the first two terms till r^2, the system is described paraxially by the equation

$$\begin{pmatrix} x_2 \\ s_2 \end{pmatrix} = \begin{pmatrix} 1 & d_2 \\ 0 & 1 \end{pmatrix} \cdot \begin{pmatrix} \cos(gL) & \frac{1}{n_0 g}\sin(gL) \\ -n_0 g \sin(gL) & \cos(gL) \end{pmatrix} \cdot \begin{pmatrix} 1 & d_1 \\ 0 & 1 \end{pmatrix} \cdot \begin{pmatrix} x_1 \\ s_1 \end{pmatrix}. \tag{8.8}$$

From formula 8.8, the following equation can be derived by claiming the term m_{12} in the expanded matrix to become zero:

$$atan\,(n_0\; g\; d_1) + atan\,(n_0\; g\; d_2) = N\;\pi - g\;L \qquad N = 1, 2, 3, ... \tag{8.9}$$

with the refraction index of the GRIN rod in the center n_0, the object distance d_1, the imaging distance d_2, and the gradient constant g.

Since this formula is only paraxial, the question comes to mind, how exact this formula is if one increases the numerical aperture. The following paragraphs compare the paraxial analytical solution with a ray trace simulation in Zemax which includes higher terms for the approximation of the GRIN index profile.

8.3.2 Imaging system

For a given GRIN rod lens with the diameter $D = 2\,\text{mm}$, the refraction index $n_0 = 1.629$ and $g = 0.312\,/\text{mm}$, the paraxial formula given in equation 8.9 is used to calculate the system parameters: $d_1 = 0.984\,\text{mm}$, $L = 5.03\,\text{mm}$, $d_2 = 3.948\,\text{mm}$, and magnification $m = 2$. According to formula 8.7, the coefficients for r^2 and r^4 are: $nr_2 = -0.079287\,/\text{mm}^2$ and $nr_4 = 3.21589 \cdot 10^{-3}\,/\text{mm}^4$. The plot in figure 8.18 shows the RMS spot radius in relation to lateral shifts around the calculated d_2, while all other parameters are kept fixed. Figure 8.17 depicts the optimal spot diagram for $d_2 = 3.97\,\text{mm}$.

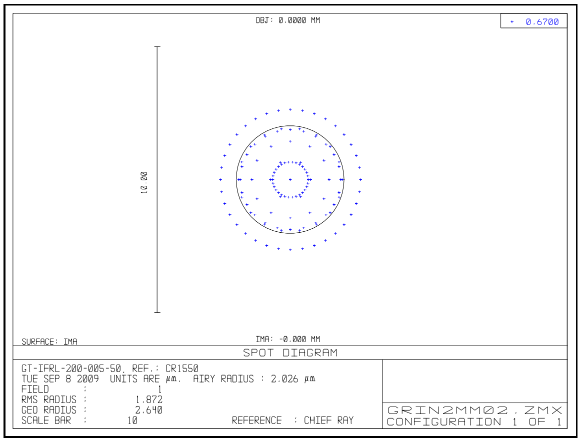

```
GT-IFRL-200-005-50, REF.: CR1550
TUE SEP 8 2009  UNITS ARE µm.   AIRY RADIUS : 2.026 µm
FIELD      :            1
RMS RADIUS :        1.872
GEO RADIUS :        2.640
SCALE BAR  :       10                REFERENCE   : CHIEF RAY
```

Figure 8.17: Spot diagram in the focus at $d_2 = 3.97\,\text{mm}$

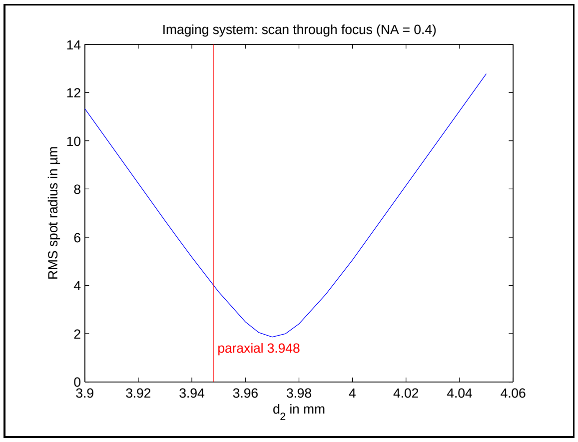

Figure 8.18: Spot RMS size: scan through the focus of the imaging system

The focal shift between paraxial calculation and simulation results as $22\,\mu\text{m}$.

8.3.3 Coupling system

If d_2 is set to zero, the imaging system focuses on its back surface, figure 8.19. One application of such a system is fiber coupling. With $d_2 = 0$, formula 8.9 is simplified to

$$atan\,(n_0\; g\; d_1) = N\;\pi - g\;L \qquad N = 1, 2, 3, \ldots\,. \tag{8.10}$$

A typical VCSEL to fiber coupling problem, as described in the previous chapter, is a VCSEL in distance $d_1 = 400\,\mu\text{m}$ from a possible collimating GRIN rod lens with a diameter of $D = 250\,\mu\text{m}$. Since geometric optics scale proportionally in size, scaling this problem by a factor of eight leads an equal system with $d_1 = 3.2\,\text{mm}$ and a GRIN rod lens with same parameters as discussed for the imaging system. Formula 8.10 calculates the length

L of the required GRIN rod lens as $L = 6.8015\,\text{mm}$ for the scaled system. The accuracy of this solution is now compared with the analytical solution through a focal scan around the distance d_1 with a fixed L, see figure 8.20.

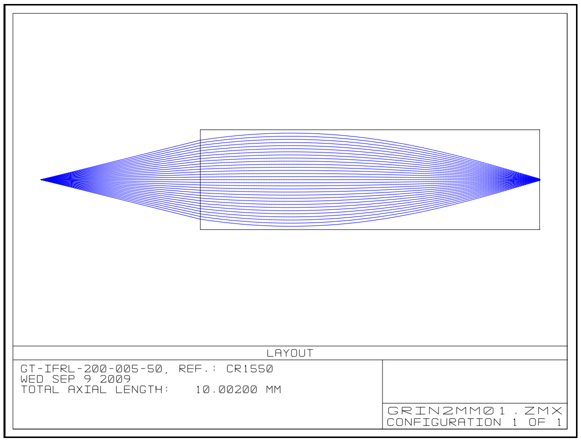

Figure 8.19: Setup of the GRIN coupler

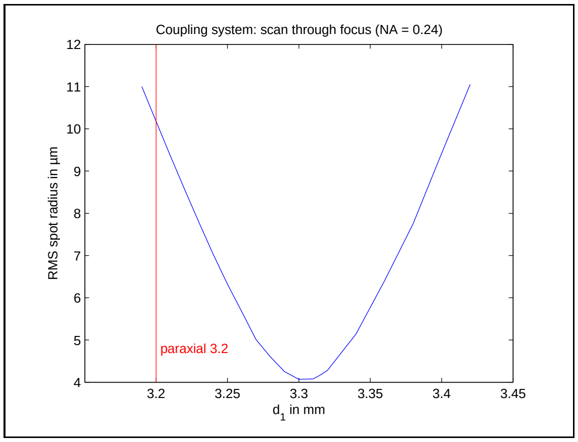

Figure 8.20: Spot RMS size: scan through the focus of the coupler system

The calculated source position is $100\,\mu\text{m}$ closer to the GRIN rod lens than the simulation suggests. While the rays are very close to the optical axis indeed focus on the paraxial distance, the aberration from the outer rays shift the optimal position.

8.3.4 Collimator

A collimator transforms a point source into collimated light. The paraxial formula, in this case

$$d_1 = \frac{1}{n_0\ g \cdot tan\,(g\ L)}\ , \tag{8.11}$$

delivers $d_1 = 0.256\,\text{mm}$ for the same GRIN rod lens as in the previous paragraphs but with a length of $L = 4.62\,\text{mm}$. Since no real focus exists on the back surface, this time the RMS direction cosines are used to evaluate the degree of collimation.

Here, the paraxially estimated position of the source is $12\,\mu\text{m}$ behind the optimal source spot.

8.3.5 Summary

In conclusion, the paraxial formulae are well suited for a first estimation of the system parameters, but for numerical apertures outside the paraxial restrictions one has to simulate the system in order to achieve the best possible result.

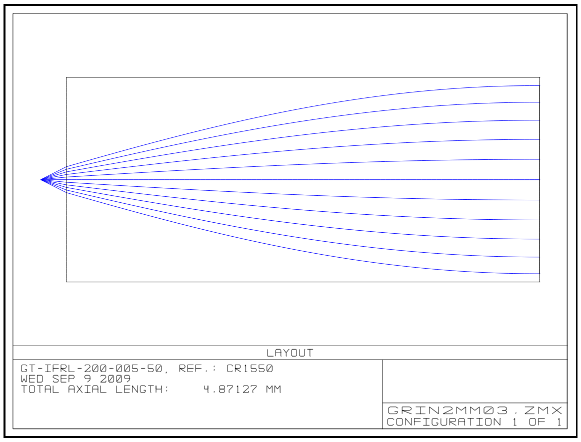

Figure 8.21: Setup of the GRIN collimator

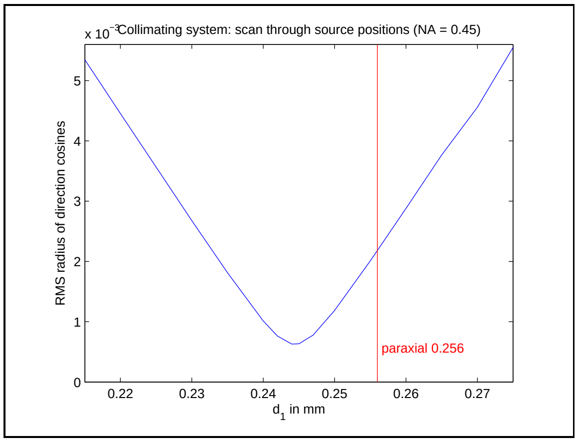

Figure 8.22: RMS of direction cosines: scan through source positions d_1 along the optical axis

8.4 Conclusion

Parallelization speeds up the scanning speed of high-throughput microscopy, enabling biologists to scan a larger parameter space in their experiments. At the time, a parallelization of classical objectives with an optimized substrate and automated scanning mechanics are due to their high imaging quality the best choice for the assembly of parallel systems. Miniaturized objectives with replicated lenses for parallel microscopes are starting to become commercially available and will increase their market share, because they become closer to the classical objectives in optical performance while being cheaper in production and easier to assemble. The presented GRIN rod lens system shows the highest potential for a very fast and compact scanning parallel microscope, but a chromatic aberration correction has to be included and the functionality of the coated beam splitter has to be demonstrated.

Part IV

Conclusion

Chapter 9

Summary and perspective

Summary

Miniaturization in general and optics in particular are both key technologies driving the progress in many multidisciplinary areas, enabling products with more functionality at reduced size and costs. At the time, miniaturization is often limited by the capability of the applied fabrication processes. Improvements in the fabrication technologies often lead to improvements in the products. UV deep lithography is one technology for the fabrication of miniaturized components and is described in the first part of this thesis.

The results obtained by photolithography are generally determined by the performance of the optics, the properties of the resist, and the applied processes. The thesis starts with an investigation of the important parameters for illumination systems used in hard contact mask lithography. Homogeneity, angular deviation, and irradiance of a UV illumination system are simulated, optimized, and measured in order to improve the quality of the resulting SU-8 structures. Applying an aperture in the focal point behind the fly's eye decreases the angular divergence at the cost of homogeneity and irradiance. Scenarios with different aperture radii are discussed. An aperture with a radius of $r_a = 8.5\,\mathrm{mm}$ was mounted into the illumination system, halving the angular deviation while keeping homogeneity and irradiance in a tolerable region.

Inclined and multidirectional exposure increase the variety of lithographically produced structures. A new setup for slanted exposure, using water immersion and a silica prism, is introduced, and the irradiance inside the photoresist in dependence of the angle of incidence and the different layers are analyzed. The analysis showed that water immersion and prism increases the possible structure angles from 36° up to 50°. For higher angles, index matching with a higher refraction index is needed.

While the fabrication of miniaturized master structures is usually expensive, replication technologies enable low priced large-scale production. A direct UV replication method and soft lithography are investigated. In particular soft lithography using PDMS is perfectly suited for the replication of lithographically produced structures and is already used in industrial environments. The soft PDMS stamp also has the disadvantage of deforming under pressure, making it difficult to minimize the remaining replication material layer. Experiments on thin substrates showed that thin PDMS stamps, with the height of 1.5 mm, allow replications with high accuracy and a minimal UV bias of about 40 μm.

Light propagation methods in geometrical optics and scalar wave optics are the topics of the second part of the thesis. The demands of an optimized mirror surface for a fiber coupler required the development of a customized ray tracer. Gaussian point and area sources are simulated using defined point distribution rather than a Monte-Carlo-Simulation. Starting from a ring model for point sources used by the simulation software Zemax, which generates quite homogeneous ray distributions on a screen, this model is expanded to simulate Gaussian point and area sources by weighting each ray according to the Gaussian function. The accuracy of this deterministic ray model is further improved by mixing discrete ring radii (called hexa mode) with a continuous helix like model (called helix mode). For the desired application of passing energies through apertures, the error of the mixed mode for point sources drops under 1% for less than $10k$ rays, while for area sources $30k$ rays are required for an accuracy of 2%.

Scalar diffraction is often modeled by either the Rayleigh-Sommerfeld or the Fresnel method, the latter being an approximation of the first method. Both methods are restricted in their allowed approximation length z_{max}. An analysis showed that the maximum propagation length z_{max} depends on the sampling number N and the ratio dx^2/λ, $z_{max} \approx N \cdot dx^2/\lambda$. Increasing the propagation distance beyond z_{max} introduces sampling errors. The influence of this error depends on the spectrum of the propagating plane waves: if the spectrum energy is very close to zero for the higher frequencies, z_{max} can be further increased. If not, another method called QFQ method is proposed to be used instead.

Going from homogeneous to non homogeneous media, the scalar methods have to be adapted. The beam propagation method (BPM) and the wave propagation method (WPM) divide the volume into small z-slices and propagate the light step by step through these slices. While BPM assumes a homogeneous medium in each slide and applies a phase correction after each propagation step, the WPM accounts directly for the different refraction indices in the media. The propagation through a series of Maxwell's Fisheyes illustrates the higher accuracy of the WPM but also shows an energy problem of the standard WPM method. An analysis reveals that the additional energy is generated in the frequencies near the evanescent limit. Different clipping methods for frequencies near the evanescent limit are introduced to eliminate the energy gain. The clipping depends on the media through which the waves are propagating. Index steps afford a more restricted clipping than gradient index profiles, but this has to be further analyzed than presented here.

An expanded version of the scalar propagation methods, which includes absorption, is then used to simulate the intensity distribution inside a 3D absorbing volume behind an aperture. This method is further expanded to simulate partially coherent light sources with a specified angular spectrum by decomposing the spectrum into plane waves, calculating the diffraction and propagation of each plane wave and summarizing the intensities in the last step. The observed riffles near corners of some rectangular SU-8 structures are also found in the 3D simulation, indicating that these riffles occur due to light diffraction at the aperture.

Applications of miniaturized components in optical interconnects and parallel microscopy are discussed in the third part.

Interconnects between chips, boards, computers, or larger entities are still mostly electric. The bandwidth demands increase while the electric interconnects already push the physical limitations forcing the developer to think about new concepts. Going from electric to optical interconnects removes the transmission restrictions of electrical wires but introduces new problems such as increasing the costs, primarily in the production of electric optical transceivers but also in handling issues concerning fiber technologies. A new concept to couple sources (VCSELs) to receivers (photodiodes) is introduced, allowing very compact and low priced transceiver modules. The concept consists of an integrated fiber mount for the alignment of fibers and a 45° mirror to deflect the light by 90° from and into the fibers. The coupling efficiency is largely increased by optimizing the mirror surface and reducing the distance between fiber and the active optical components, allowing coupling efficiencies of 40%. Demonstrators are built using multidirectional UV deep lithography in SU-8 and soft lithography for replication on thin substrates. The thesis also shows that these integrated fiber couplers are suited for large-scale production, because standard replication techniques like soft lithography are applicable. Active optical cables are one important industrial application of this new coupling concept where a compact electro-optical receiver has to be integrated into the connector, but every other application where fiber coupling is required, is also feasible.

Miniaturization is also interesting for parallel microscopy. An analysis of the important parameters of scanning microscopy concerning the optics is described. Since the lens diameter in relation to the field of view is the limiting factor for parallelization, four different concepts are presented and analyzed: a classical approach, one with miniaturized lenses, one with micro lenses and finally one with GRIN rod lenses. The custom-made GRIN rod system, optimized for the microwell cell array used in the ViroQuant project, allows the most compact design, hence the fastest one. Finally, the design, assembly and some components of the GRIN rod system are presented.

Perspectives

Miniaturization will continue in many fields of technology, allowing to integrate more functions into an equal volume. For example in the field of optical interconnects, where active optical cables started with four interconnects in one connector, twelve interconnects are already announced and more will follow. Improvements in fabrication processes like ultra precision machining will further increase the diversity of miniaturized components and might soon make elliptical shaped mirror surfaces for the presented integrated fiber coupler possible, increasing the coupling efficiency to 96%. A higher coupling efficiency also reduces the heat generated by the device, because the VCSEL's power can be reduced while staying in the boundaries of the power budget.

The reduced size of optical components will emphasize the research in simulation methods for an accurate treatment of the vectorial character of light. The presented scalar methods are only accurate for apertures considerably larger than the wavelength. The combination of different methods to simulate an optical system has already begun. Classical ray tracer offer wave analysis methods and already implement polarization effects. Optical simulations will have to combine methods for all distances, from near field to far field, in order to satisfy the demands of the market. The increasing computational power will further support the computationally intensive simulations and thus allowing them to become more realistic, not only by faster processors but also by specialized expansion cards, for example GPUs.

Miniaturization in parallel microscopy has already begun, like the system from Dmetrix proves. These systems are still limited by the small variety of materials suitable for replication in comparison with the vast glass catalog available to classical optic designer. With the research going on, new polymer combinations might improve the chromatic aberrations enough to reach the imaging quality of classical objectives. With an integration of chromatic aberration correction, the presented customized GRIN rod system will become an interesting alternative to classical parallel microscopes, reducing the number of scans for a complete microwell cell array to one.

Part V

Appendix

Bibliography

[1] M. Born and E. Wolf. *Principles of Optics.* Cambridge, 7th edition edition, 2006.

[2] C. Brecher, M. Weinzierl, and F. Niehaus. Microscale mass production. *MICROmanufacturing*, pages 44–47, 2009.

[3] K.-H. Brenner. Computational optics. *Lecture at the University of Heidelberg*, 2008.

[4] K. H. Brenner. *Vorlesungsskript Grundlagen der Optik HWS2007.* University of Heidelberg, 2007.

[5] K.-H. Brenner and W. Singer. Light propagation through microlenses: a new simulation method. *Applied Optics, 32*, pages 3990–3998, 1993.

[6] E. Brinksmeier, O. Riemer, and J. Osmer. Tool path generation for ultra-precision machining of free-form surfaces. *Production Engineering*, pages 241–246, 2008.

[7] J.C. Butcher. *The Numerical Analysis of Ordinary Differential Equations: Runge-Kutta and General Linear Methods.* John Wiley & Sons Ltd, 1986.

[8] CBM-Collaboration. Cbm progress report 2008. *Published in the internet: http://www.gsi.de/documents/DOC-2009-Feb-233.html*, 2009.

[9] V. Cerveny, M. M. Popov, and I. Psencik. Computation of wave fields in inhomogeneous media - gaussian beam approach. *Geophys. J. R. astr. Soc. 70*, pages 109–128, 1981.

[10] Y.-J. Chang, K. Mohseni, and V. M. Bright. Fabrication of tapered su-8 structure and effect of sidewall angle for a variable focus microlens using ewod. *Sensors and Actuators A 136 (2)*, pages 546 – 553, 2006.

[11] Fair Consortium. Fair facility for antiproton and ion research. *Published in the internet: http://www.gsi.de/fair/*, 2009.

[12] J. W. Cooley and J. W. Tukey. An algorithm for the machine calculation of complex fourier series. *Math. Comput., 19*, pages 297–301, 1965.

[13] A. Cox and A. L. King. A system of optical design. *American Journal of Physics, 34*, 1966.

[14] M. Despont, H. Lorenz, N. Fahrni, J. Brugger, P. Renaud, and P. Vettiger. High-aspect-ratio, ultrathick, negative-tone near-uv photoresist for mems applications. *Micro Electro Mechanical Systems, 26*, pages 518–522, 1997.

[15] M. Deubel, G. von Freymann, M. Wegener, S. Pereira, K. Busch, and C. M. Soukoulis. Direct laser writing of three-dimensional photonic-crystal templates for telecommunications. *nature material, 3*, pages 444–447, 2004.

[16] F. H. Dill. Optical lithography. *IEEE Trans. Electron Devices, 7*, pages 440–444, 1975.

[17] F. H. Dill, W. P. Hornberger, P. S. Hauge, and J. M. Shaw. Characterization of positive photoresist. *IEEE Trans. Electron Devices, 7*, pages 445–452, 1975.

[18] F. H. Dill, A. R. Neureuther, J. A. Tuttle, and E. J. Walker. Modeling projection printing of positive photoresists. *IEEE Trans. Electron Devices, 7*, pages 456–464, 1975.

[19] M. D. Feit and J. A. Fleck. Light propagation in graded-index optical fibers. *Applied Optics, 17*, pages 3990–3998, 1978.

[20] M. Fertig and K.-H. Brenner. Vectorial extension of the wave propagation method (vwpm). *DGaO-Proceedings (Online-Zeitschrift der Deutschen Gesellschaft für angewandte Optik e. V.)*, 2009.

[21] J. A. Fleck, J. R. Morris, and M. D. Feit. Time-dependent propagation of high energy laser beams through the atmosphere. *Appl. Phys., 10*, pages 129–160, 1976.

[22] K.K. Gan, F. Vasey, and T. Weidberg. Joint atlas-cms working group on optical links. lessons learned and to be learned from lhc. *Published in the internet: https://edms.cern.ch/document/882775/3.8*, 2007.

[23] J.W. Goodman. *Introduction to Fourier Optics*. McGraw-Hill, New York, 2nd edition edition, 1996.

[24] H. Gross. *Handbook of optical systems Vol. 1*. Wiley-VCH, 2005.

[25] ViroQuant group. Microwell cell array. *Published in the internet: http://www.viroquant.uni-hd.de/technology_platforms/viroquant-cellnetworks-rnai-screening-facility/projects/cell-arrays.html*, 2009.

[26] L. J. Guerin. The su-8 homepage. *Published in the internet: http://www.geocities.com/guerinlj/*, 2004.

[27] M. Han, W. Lee, S.-K. Lee, and S.-S. Lee. 3d microfabrication with inclined/rotated uv lithography. *Sensors and Actuators A, 111*, pages 14–20, 2004.

[28] Inc. IGI Consulting. Active optical cables market analysis 2009. **Commercial available**, 2009.

[29] K. L. Konnerth and F. H. Dill. In-situ measurement of dielectric thickness during etching or developing processes. *IEEE Trans. Electron Devices, 7*, pages 452–456, 1975.

[30] F. Koyama, S. Kinoshita, and Kenichi Iga. Room temperature cw operation of gaas vertical cavity surface emitting laser. *Japanese Journal of Applied Physics, 18*, pages 2329–2330, 1979.

[31] N. LaBianca and J. Delorme. High aspect ratio resist for thick film application. *Proceedings of the international Society of Optical Engineering (SPIE), 2438*, pages 846–852, 1995.

[32] Z. Ling and K. Lian. Su-8 3d microoptic components fabricated by inclined uv lithography in water. *Microsystem Technologies, 13*, pages 245–251, 2006.

[33] G. Liu, Y. Tian, and Y. Kan. Fabrication of high-aspect-ratio microstructures using su8 photoresist. *Microsystem Technologies, 1*, pages 343–346, 2003.

[34] X. Liu. *Design, Analysis and Fabrication of Micro Optical Systems involving UV-Deep Lithography - with an Aplication in Atomic Physics.* PhD thesis, University of Mannheim, 2008.

[35] A. W. Lohmann. Scaling laws for lens systems. *Appl. Optics, 28*, pages 4996–4998, 1989.

[36] L. Lorenz, M. Despont, N. Fahrni, N. LaBianca, P. Renaud, and P. Vettiger. Su-8: a low-cost negative resist for mems. *J. Micromech. Microeng., 7*, pages 121–124, 1997.

[37] C. A. Mack. Thirty years of lithography simulation. *Optical Microlithography XVIII Proceedings of the SPIE, 5754*, pages 1–12, 2005.

[38] MicroChem. Photoresist nano su8 50, su8 100. *Published in the internet: http://www.microchem.com/products/su-eigth.htm*, 2009.

[39] L. Montagnino. Ray tracing in inhomogeneous media. *J. Opt. Soc. Am., 58*, pages 1667–1668, 1968.

[40] P. Munzert, U. Schulz, and N. Kaiser. Hochreflektierende beschichtungen auf kunststoffoptiken. *Vakuum in Forschung und Praxis, 19*, pages 11–15, 2007.

[41] B. Neumann, M. Held, U. Liebel, H. Erfle, P. Rogers, R. Pepperkok, and J. Ellenberg. High-throughput rnai screen-ing by time-lapse imaging of live human cells. *Nature Methods, 3*, pages 385–390, 2006.

[42] R. Pepperkok and J. Ellenberg. High-throughput fluorescence microscopy for systems biology. *Nature Reviews Molecular Cell Biology, 7*, pages 690–696, 2006.

[43] S. Scheffelmeier. Untersuchung von verfahren zur replikation mikrooptischer elemente. *Diploma thesis at the chair of optoelectronics*, 2006.

[44] G. M. Schmid, M. D. Smith, C. A. Mack, V. K. Singh, Burns S. D., and Willson C.G. Understanding molecular-level effects during post-exposure processing. *Proc. SPIE Advances in Resist Technology and Processing XVIII, 4345*, pages 1037–1047, 2001.

[45] A. Sharma, D. V. Kumar, and A. K. Ghatak. Tracing rays through graded-index media: a new method. *Appl. Opt., 21*, pages 984–987, 1982.

[46] J. M. Shaw. Negative photoresists for optical lithography. *IBM Journal of Research and Development, 41*, pages 81–94, 1997.

[47] S. Sinzinger and J. Jahns. *Microoptics.* Wiley-VCH, 1999.

[48] E. Slogsnat, D. Wohlfeld, and K.H. Brenner. Non-stereoscopic method for deflectometric measurement of reflecting surfaces. *DGaO-Proceedings (Online-Zeitschrift der Deutschen Gesellschaft für angewandte Optik e. V.)*, 2009.

[49] H. Soda, Ken-ichi Iga, C. Kitahara, and Y. Suematsu. Gainasp/inp surface emitting injection lasers. *Japanese Journal of Applied Physics, 18*, pages 2329–2330, 1979.

[50] B. D. Stone and G. W. Forbes. Differential ray tracing in inhomogeneous media. *J. Opt. Soc. Am. A 14*, 1997.

[51] H.-B. Sun, S. Matsuo, and H. Misawa. Three-dimensional photonic crystal structures achieved with two-photon-absorption photopolymerization of resin. *Applied physics letters, 74*, pages 786–788, 1999.

[52] J. Troska, S. Dris, K. Gill, R. Grabit, D. Ricci, and F. Vasey. Cms optical links - lessons learned from mass production. *Published in the internet: http://cdsweb.cern.ch/record/1034347*, 2006.

[53] F. Vasey. Optical links for lhc: experience from the cms project and future prospects. *Published in the internet: http://cdsweb.cern.ch/record/811663*, 2004.

[54] M.A. Verschuuren, R. van de Laar, R. Voelkel, and H. van Sprang. Scil: large area direct molding of optical components. *EOS Conferences at the World of Photonics Congress 2009, Proceeding in Manufacturing of Optical Components*, 2009.

[55] D. Wohlfeld and M. Kufner. Herstellung kontinuierlicher phasenelemente in su-8. *Student project report from the Chair of Optoelectronics, University of Heidelberg*, 2002.

[56] Y. Xia and G. M. Whitesides. Soft lithography. *Angewandte Chemie Int. Ed. , 37*, pages 551–575, 1998.

[57] Y.-K. Yoon, J.-H. Park, F. Cros, and M. G. Allen. Integrated vertical screen microfilter system using inclined su-8 structures. *J. Micromech. Microeng., 11*, pages 227–230, 2003.

[58] Y.-K. Yoon, J.H. Park, and M. G. Allen. Multidirectional uv lithography for complex 3-d mems structures. *Journal of microelectromechanical systems, 15*, pages 1121 – 1130, 2006.

[59] J. Zhang, K. L. Tan, G. D. Hong, L. Y. Yang, and H. Q. Gong. Characterization of the polymerization of su-8 photoresist and its applications in micro-electro-mechanical systems (mems). *J. Micromech. Microeng., 11*, pages 20–26, 2001.

About the author

Denis Wohlfeld was born July 16, 1977, in Leipzig, Germany. Beginning in 1997, he studied Communication Engineering at the Hochschule Mannheim and obtained an intermedia diploma in 1999. Afterwards he changed to the University of Mannheim to study Computer Engineering. His subjects of study include optoelectronics, communication engineering and VLSI design. His diploma thesis, written in 2004, is entitled "Analysis and fabrication of micro prisms for optical communications". Following this, he began his PhD work with the Chair of Optoelectronics, Professor Brenner, at the University of Mannheim, Germany.

Publications and conference proceedings

- D. Wohlfeld, K.-H. Brenner "Fabrication of integrated structures for coupling VCSEL to fibre", DGaO-Proceedings (Online-Zeitschrift der Deutschen Gesellschaft für angewandte Optik e. V.), ISSN: 1614-8436, , 106. Jahrestagung in Breslau/Polen (2005)
- D. Wohlfeld, K.-H. Brenner, "Fabrikation und Integration von mechanisch-optischen Strukturen zur Kopplung von VCSELs mit Glasfasern", Mikrosystemtechnik Kongress 2005, ISBN 978-3-8007-2926-5 / ISBN 3.8007-2926-1, pp 167-169, http://www.gsi.de/documents/DOC-2007-Jul-4.html, (2005)
- D. Wohlfeld, K.-H. Brenner, "Anwendung optischer Verbindungstechniken in der Hochenergiephysik", ORT 2005, 8. Workshop Optik in der Rechentechnik, ISSN 1437-8507, p. 76-82, Ilmenau (2005)
- D. Wohlfeld, S. Scheffelmeier, K.-H. Brenner, "Doppelbelichtung und Replikation von Mikrostrukturen für die optische Informationsverarbeitung", DGaO-Proceedings (Online-Zeitschrift der Deutschen Gesellschaft für angewandte Optik e. V.), ISSN: 1614-8436, , 107. Jahrestagung in Weingarten (2006)
- D. Wohlfeld, K.-H. Brenner, "UV-Tiefenlithographie mit Zweiphasenbelichtung zur Herstellung von replizierbaren optischen Verbindungsstrukuren", ORT 2006, 9. Workshop Optik in der Rechentechnik, ISSN 1437-8507, p. 106 - 109, Siegen, http://www.gsi.de/documents/DOC-2007-Jul-7.html, (2006)

- D. Wohlfeld, E. Slogsnat, K.-H. Brenner, “Integrated beam splitters for array microscopy in life science”, DGaO-Proceedings (Online-Zeitschrift der Deutschen Gesellschaft für angewandte Optik e. V.), ISSN: 1614-8436, 110. Jahrestagung in Brescia/Italien, submitted (2009)
- D. Wohlfeld, F. Merchán, K.-H. Brenner, “Integrated VCSEL to fiber couplers fabricated with micro-machining”, World of Photonics congress, Manufacturing of Optical Components, Munich/Germany, (2009)
- F. Merchán, D. Wohlfeld, K.-H. Brenner, “High speed communication using micro optical integration”, DGaO-Proceedings (Online-Zeitschrift der Deutschen Gesellschaft für angewandte Optik e. V.), ISSN: 1614-8436, 110. Jahrestagung in Brescia/Italien, submitted (2009)
- F. Merchán, D.Wohlfeld, K.-H. Brenner, “Development of active optical cables”, Workshop of Optics in Computing (Optik in der Rechentechnik, ORT), submitted (2009)